

Development of Advanced Technologies for Mixed
Natural Gas Detection

BY

ALI ATWI

B.ENG

Development of Advanced Technologies for Mixed Natural Gas Detection

Development of Advanced Technologies for Mixed
Natural Gas Detection

By ALI ATWI, B.ENG

A Thesis Submitted to the School of Graduate Studies in Partial Fulfilment
of the Requirement for the Degree Master's of Applied Science

McMaster University
Canada

Hamilton, Ontario,

MASTER'S OF APPLIED SCIENCE (2022)

(Engineering Physics)

Title: Development of Advanced Technologies for Mixed Natural Gas Detection

Author: ALI ATWI
B.ENG (American University of Beirut, Beirut, Lebanon)

Supervisor: Dr. Chang-Qing Xu

Number of pages: 110, xiv

Abstract

Advanced technologies for mixed gas detection are discussed. A calorific measurement technique for hydrogen-natural gas mixtures using ultrasonic transducers is examined. Measuring the speed of sound in the gas medium enables an accurate composition testing of mixed gas. At the beginning, different ultrasonic transducers are tested and a suitable one for gas testing is chosen. A jig is designed to conduct the testing with nitrogen/oxygen mixtures in a proof of principle experiment. Another jig is designed and manufactured to test a transit time ultrasonic method for flow rate calculation in order to obtain a full energy flow measurement.

A mixed gas leak detection technique based on laser spectroscopy is also studied. A Mid-Wave Infrared (MWIR) laser is implemented to be used as a source in a direct absorption measurement for methane detection. The implemented MWIR laser uses nonlinear optics to generate a MWIR output. A novel intracavity structure using periodically poled lithium niobate as the nonlinear crystal is implemented, and the highest blackbox efficiency for continuous wave difference frequency generation in the MWIR region is reported, to the best of our knowledge. Currently the output power is around 8.1 mW at 3.5 μm with a 1.058% W^{-1} blackbox efficiency. Watt level MWIR generation is expected using an optimized setup.

At last, a second laser source that operates in the long-wave infrared (LWIR) region was also studied. The discussed laser setup for LWIR generation is similar to the MWIR one with different pump and signal wavelengths and an orientation patterned gallium phosphide (OP-GaP) as the nonlinear crystal. Due to the absorption loss of GaP at the pump wavelength, only mW power level is expected out of the intracavity structure. Some alternative approaches for LWIR generation are discussed.

Acknowledgments

I would like to thank my supervisor Dr. Chang-qing Xu for his appreciated support and guidance throughout this thesis project. Dr. Xu's knowledge has inspired me to be where I am today.

I would also like to thank my committee members Dr. Rafael Kleiman and Dr. Ryan Lewis.

I would like to thank all my colleagues and specially Tyler Kashak who was the first one to support me in any experimental work, Liam Flannigan who helped me a lot in understanding some advanced fundamentals. It was a great pleasure for me to work with such a supportive group.

Finally, I would like to thank my wife, parents, siblings, and my extended family in Canada for their great support. I would not have been able to complete this work without their understanding.

Table of Contents

Abstract	iv
Acknowledgments	v
List of Figures	ix
List of Tables	xii
List of Abbreviations and Symbols	xiii
1 Introduction	1
1.1 Green House Gases	1
1.1.1 Greenhouse Gases Impacts	2
1.1.2 Climate Change Agreements	3
1.1.3 Solutions for Net-Zero Emission	3
1.1.3.1 Methane Detection.....	4
1.1.3.2 Optical Sensors for Methane Detection.....	5
1.1.3.3 Other Methane Sensors.....	7
1.1.4 Hydrogen vs Methane	8
1.1.5 Challenges with Hydrogen Blending	9
1.1.6 Current Projects in Canada	10
1.1.7 Gas Quality Tracking	11
1.2 Calorific Measurement and Leak Detection Proposed Solution	12
1.3 Thesis Structure.....	12
2 Basic Theories on Ultrasonic Transducers and Diode Pumped Solid State Lasers	14
2.1 Ultrasonic Technology	14
2.1.1 Piezoelectric Element.....	15
2.1.2 Matching Layer	17

2.1.3	Backing Element	17
2.1.4	Coupling.....	18
2.2	Ultrasonic Techniques for Gas Flow Rate Measurements	18
2.3	Ultrasonic Techniques for Mixed Gas Composition Measurements	20
2.4	MWIR Laser for Methane Detection	22
2.4.1	Diode Pumped Solid State (DPSS) Lasers.....	23
2.4.2	Nonlinear Optics	27
2.4.3	Phase Matching.....	29
2.4.4	Periodically Poled Lithium Niobate.....	31
2.4.4.1	Cavity Enhanced Nonlinear Process.....	32
2.4.5	MWIR and LWIR for gas Detection.....	35
3	Calorific Measurements for Mixed Natural Gas Using an Ultrasonic Calibration Technique	38
3.1	Introduction	38
3.2	Ultrasonic Transducers Testing.....	39
3.3	Gas Composition Experimental Setup Design	44
3.4	Experimental and Simulation Results	47
3.4.1	Composition and Flow Rate Measurement.....	57
3.4.2	Flow Rate Measurement Using Ultrasonic Transducers.....	59
3.5	Conclusion and Future Work	65
4	Mid Wavelength Infrared Laser Source for Natural Mixed Gas Leak Detection	67
4.1	Introduction	67
4.2	Experimental Setup and Procedure	68
4.2.1	Experimental Procedure.....	70

4.2.2	Spontaneous Parametric Down Conversion (SPDC) Test	72
4.2.3	Beam Profiling	74
4.3	Experimental Results.....	77
4.4	Discussion	80
4.4.1	DFG Power Enhancement.....	80
4.4.2	Wavelength Tunability.....	82
4.4.3	DFG Linewidth	83
4.5	Conclusion.....	83
5	Long Wavelength Infrared Laser Source for Natural Mixed Gas Leak Detection	84
5.1	Introduction	84
5.2	Experimental Setup	85
5.2.1	1342nm Pump Laser - Experimental Results.....	88
5.2.2	1342 nm Beam Profiling and Linewidth.....	89
5.3	LWIR Simulation	91
5.4	Alternative LWIR Generation Methods.....	92
5.5	Conclusion.....	95
6	Thesis Summary.....	97
6.1	Summary	97
6.2	Skills Acquired.....	98
7	References.....	99

List of Figures

Figure 1.1: Annual Worldwide CO ₂ Emission [7]	1
Figure 1.2: (a) Methane's absorption spectrum from 2.5 to 10 micro meter. (b) a close up on methane's absorption spectrum in the MWIR range [39]	7
Figure 2.1: Ultrasonic Transducer Structure [60]	14
Figure 2.2: Wetted Transit Time Flow Rate Measurement Setup	19
Figure 2.3: Energy Level Diagram of Nd:YVO ₄ [81].....	24
Figure 2.4: Four Level Laser System.....	25
Figure 2.5: Simple Nd:YVO ₄ Resonator Cavity	27
Figure 2.6: Nonlinear mixing schematics: (a) second harmonic generation (SHG), (b) sum frequency generation (SFG), and (c) difference frequency generation (DFG).....	29
Figure 2.7: Non-phase matched, and phase matched wave vectors.....	30
Figure 2.8: QPM phase matching	31
Figure 2.9: (a) Initial spontaneous polarization of a lithium niobate crystal. (b) domain inversed PPLN obtained with an external electric field application [84]	32
Figure 2.10: (a) Single pass structure, (b) extracavity structure, (c) intracavity structure, and (d) folded intracavity structure.....	34
Figure 2.11: Atmospheric transmission (%) vs wavelength (μm) [93].....	35
Figure 3.1: Ultrasonic Transducers Test Setup.....	40
Figure 3.2: Expected Oscilloscope Screen with Emitter Signal on Channel 1 and Receiver Signal on Channel 2	41
Figure 3.3: Ultrasonic Transducer 2 Testing Results.....	42
Figure 3.4: Ultrasonic Transducer 3 Testing Results.....	42
Figure 3.5: Ultrasonic Transducer 4 Testing Results.....	43
Figure 3.6: Ultrasonic Transducer 6 testing results	43
Figure 3.7: jig Design of Gas Composition Experiment.....	44
Figure 3.8: Section View of the Jig Design	45
Figure 3.9: Cylinder Jig Assembly During the Composition Testing Experiment.....	46
Figure 3.10: Implemented Mechanical Cylinder/Jig Assembly	47

Figure 3.11: Speed of Sound Comparison Between the Experiment and Airliquide Report	48
Figure 3.12: Gas Composition Comparison Between the Experiment and Airliquide Report.....	48
Figure 3.13: Experimental Time Difference vs Oxygen Molar Concentration	49
Figure 3.14: Experimental and Theoretical Speed of Sound Calculations vs Oxygen Molar Concentration	50
Figure 3.15: Speed of Sound in Methane-Hydrogen and Nitrogen-Oxygen Mixtures.....	53
Figure 3.16: Speed of Sound in Methane-Hydrogen and Nitrogen-Oxygen Mixtures.....	53
Figure 3.17: Price of Mixed gas vs Consumption.....	56
Figure 3.18: Error bars in Price due to Ultrasonic Transducer Composition Testing Uncertainty.....	56
Figure 3.19: Experimental Setup of Composition and Flow Rate Measurements.....	58
Figure 3.20: Ultrasonic Flow Meter Jig Design.....	59
Figure 3.21: Comparison Methods Between Experimental, Simulation and Real Results	60
Figure 3.22: Ultrasonic Time Delay Measurements vs Different Flow Rates.....	61
Figure 3.23: Velocity Contour for the Flow Inside the Pipe.....	62
Figure 3.24: Experimental and Simulation Time Delay Measurements with Different Flow Rates	62
Figure 3.25: Experimental Ultrasonic and Real Rotary Flow Rate Measurements	64
Figure 3.26: Experimental Ultrasonic, Real Rotary and calibrated Flow Rate Measurements	64
Figure 4.1: Direct Laser Absorption Spectroscopy.....	67
Figure 4.2: Schematic Diagram of the MWIR DFG Laser.....	69
Figure 4.3: Schematic of the Thermal Control Setup	70
Figure 4.4: SPDC Test Setup	73
Figure 4.5: SPDC Signal Obtained on the OSA at 25 °C	74

Figure 4.6: (a) 1064 nm Beam Diameter 5" after the OC (b) 1064 nm Beam Diameter 8.35" After the OC	75
Figure 4.7: 1064 nm Beam Profile 5" After the OC	76
Figure 4.8: 1528 nm Minimum Beam Diameter at 10.5 cm From the Focusing Lens	76
Figure 4.9: Experimental and Simulation Results for Leaking 1064 nm Power Against 808 nm Power	77
Figure 4.10: Experimental and Simulation DFG Output Power vs 808 nm Pump Power	78
Figure 4.11: Black Box Efficiency Diagram	79
Figure 4.12: Experimental and Theoretical Black Box Efficiencies as a Function of Signal Wavelength	79
Figure 4.13: Measured and Theoretical Temperature Tuning Curves	80
Figure 4.14: Expected MWIR DFG Power with 10W EDFA	81
Figure 4.15: Methane Absorption Spectrum in the MWIR Region	82
Figure 5.1: Methane Absorption Spectrum in the LWIR Region	85
Figure 5.2: Schematic Diagram of the LWIR Laser	86
Figure 5.3: Schematic Diagram of 1342 nm Diode Pumped Solid State Laser	87
Figure 5.4: Logical Flow of LWIR Study	88
Figure 5.5: Experimental and Simulation Leaking 1342nm Powers	88
Figure 5.6: Experimental and Simulation Intracavity 1342nm Powers	89
Figure 5.7: (a) 1342 nm 2D Beam Profile (b) 1342 nm 3D Beam Profile	90
Figure 5.8: Screenshot of the OSA at 1342 nm	91
Figure 5.9: Simulation Results for LWIR Power against 808 nm Pump Power	92
Figure 5.10: DFG Output Power at 10 W 808 nm Pumping and 4 W 1625 nm Signal Power as a Function of GaP Length	93
Figure 5.11: LWIR Generation with a Single Pass Structure 1342 nm Pump and 1625 nm Signal	94
Figure 5.12: LWIR Generation with a Single Pass Structure 1550 nm Pump and 1950 nm Signal	95

List of Tables

Table 1.1: Hydrogen vs Methane Comparison	9
Table 2.1: Theoretical Speed of Sound in Different Gases.....	20
Table 2.2: MWIR Generation Methods	22
Table 2.3: Different Structures and nonlinear processes using PPLN crystals.....	35
Table 3.1: List of Tested Transducers for the Feasibility Study.....	39
Table 3.2: Cylinders Used in the Mixed Gas Composition Testing with their Relative Molar Concentrations of Nitrogen and Oxygen.....	46
Table 3.3: Time Delay Between Channel 1 and Channel 2 with Different Mediums	49
Table 3.4: Experimental vs Expected Speed of Sound Comparison.....	50
Table 3.5: Comparison Between Composition Measurement Using Ultrasonic Transducers and Airliquide Reported Composition	51
Table 3.6: Obtained Experimental Results for Composition and Flow Measurements....	58
Table 3.7: Experimental Time Delays obtained with Different Air flow Rates	61
Table 3.8: Measured Flow Rates with the Time Transit Ultrasonic Method and the Rotary Meter	63

List of Abbreviations and Symbols

AR	Anti-reflection
CW	Continuous wave
DPSS	Diode pumped solid state
DFG	Difference frequency generation
GHG	Greenhouse gases
GWP	Global warming potential
HR	High reflectivity
HT	High Transmission
LWIR	Long-wavelength infrared
MWIR	Mid-wavelength infrared
NLO	Nonlinear optics
OC	Output coupler
OP-Sc	Orientation patterned semi-conductor
OSA	Optical spectrum analyzer
PPLN	Periodically poled lithium niobate
QCL	Quantum cascade laser
QPM	Quasi-phase match
SFG	Sum frequency generation
SHG	Second harmonic generation
SWIR	Short-wavelength infrared
TEC	Thermo-electric cooler

Development of Advanced Technologies for Mixed Natural Gas Detection

Chapter 1

1 Introduction

1.1 Green House Gases

Greenhouse gases trap heat in the atmosphere. Infrared radiation emitted from the surface of earth gets absorbed by some gases which redirects the net heat energy back to earth [1]. The main greenhouse gases are Carbon dioxide (CO₂), Methane (CH₄), Nitrous Oxide (N₂O), and Fluorinated gases [2].

Technological advancement, and the continuous need for energy that is being fulfilled by burning fossil fuels, and the transportation of coal and natural gas are some of the key factors that are affecting the greenhouse gases emission rates [3].

Studies show that the concentration of greenhouse gases has increased drastically since the last century [4]. The emission of greenhouse gases increased by more than 45% since 1990 [5]. Canada reported 13.1% increase in greenhouse gas emission between 1990 and 2020 [6]. Figure 1.1 shows the trend in the annual CO₂ emissions worldwide since 1940 [7]

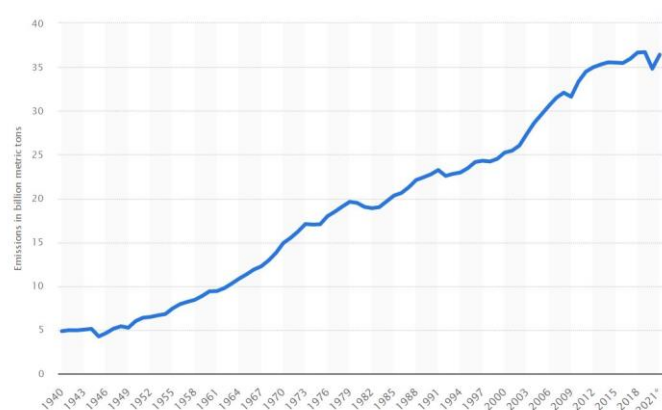


Figure 1.1: Annual Worldwide CO₂ Emission [7]

The greenhouse gases have different potential risks due to their specific properties. A concept called Global Warming Potential (GWP) is used to convert the amount of any greenhouse gas emitted to its equivalent carbon dioxide equivalent. For example, CO₂ has a GWP of 1 while CH₄ has a GWP of 27-30. CH₄ emission has more risks associated with it compared to CO₂ since it absorbs more energy [8]. In 2020, Methane accounted for 11% while CO₂ accounted for 79% of the emitted greenhouse gases in the United States of America as shown in Figure 1.2 [9].

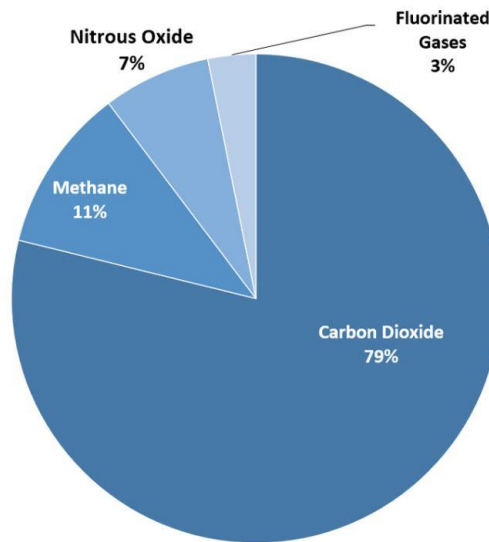


Figure 1.2: Different Percentages of Greenhouse Gases emitted in the US in 2020

1.1.1 Greenhouse Gases Impacts

Greenhouse gases have severe impacts on the environment, human health, and the global economy. The overall temperatures on earth are expected to increase due to the absorption of net heat in the atmosphere by the greenhouse gases. The world's surface air temperature has risen by 1.1 °C since 1900 due to greenhouse gas emission [10]. The projected increase in temperature is an additional 4°C until the end of the century if greenhouse emission continues to follow the current trend [10]. As a consequence of

warmer temperatures, snow and sea ice are expected to melt at an increased rate which would result in rising the sea levels [11].

Flooding, forest fires, and loss of wildlife species are other consequences for the heat trapping effect of greenhouse gases [11]. Humans would have some serious health problems associated with the impacts of greenhouse gases such as heat strokes and water-borne diseases [11]. The emission of greenhouse gases would have economic impacts such as damage to infrastructure caused by extreme weather conditions, as well as need for additional social and health support systems [11]. The roots of these effects have been discussed and studied since 1896. Swedish scientist Svante Arrhenius was the first to link the presence of CO₂ with the earth warming effect [12].

1.1.2 Climate Change Agreements

Countries around the world have been trying to come up with a protocol to reduce greenhouse gas emissions since the early 1990's. In 1992, 197 countries around the world established an annual forum aiming to reduce the concentration of greenhouse gases in the atmosphere. In 2005, the Kyoto Protocol was the first legally binding agreement to set rules for some countries to reduce emissions. In 2015, the Paris agreement was signed by most of the world's countries aiming at net-zero emissions by 2050 [13]. Canada's plan is to reduce the greenhouse gas emission by 40-45% below 2005 levels by 2030 [14].

1.1.3 Solutions for Net-Zero Emission

Many solutions have been proposed to reduce the carbon footprint. Some of which include improving energy efficiency, early monitoring and detection of greenhouse gas leakage, and increasing the consumption and use of renewable energy [15]. More proposed solutions consist of producing hydrogen and using it to feed zero emission fuel cells, protecting forests, and charging countries for their greenhouse gases [15].

Blending hydrogen with natural gas is a potential solution for lowering greenhouse emissions. Blending hydrogen would require minor changes to the existing mixed gas delivery infrastructure instead of having to install new dedicated infrastructure for hydrogen transport [16]. There are numerous benefits to blending hydrogen in natural gas such as:

- Reduction in GHG emission: blending 5% of hydrogen into mixed natural gas is estimated to reduce the carbon dioxide emission by 2% [17].
- Taking advantage of the existing infrastructure for distribution [17].
- Savings in the capital cost of developing dedicated infrastructure for hydrogen storing and delivery
- Increasing the supply and demand for clean energy obtained from the combustion of hydrogen which decreases the cost of hydrogen supply.

Obanijesu et al. [18] discovered the importance of hydrogen blending in subsea pipelines to inhibit the formation of hydrate, which is a safety hazard [18].

Flekiewicz and Kubica [19] proved that the presence of hydrogen in natural gas increases the SI engine's efficiency. They discovered that the consumption of the SI engines drops when supplied with mixed natural gas/hydrogen blends.

Glanville et al. [20] proved that many end user appliances perform with better efficiencies when operated with hydrogen-natural gas mixtures.

Scientists also propose the use of nuclear power as a solution since nuclear plants don't have direct air pollution impacts [21].

1.1.3.1 Methane Detection

One ton of emitted methane is approximately equivalent to 30 tonnes of Carbon Dioxide when comparing the impacts of both gases over a period of 100 years. Methane accounts for 30% of global warming, and the main human-caused methane source is the

energy sector [22]. As a result, it is vital to track the sources of methane leaking especially in oil and gas operations. Accidents in the natural gas storing industry are also another reason for methane leaking, similar to the leaking incident from Aliso Canyon Underground storage facility in Los Angeles [23]. Olmer et al. [24], reported that 5% of all greenhouse emission are linked with the delivery and handling of natural gas.

Furthermore, methane gas would be considered an explosive material once its concentration surpasses 5% in an enclosed space [25]. The use of methane is crucial in the future since it is the main component of natural gas, which is seen as a key factor in the transition to a fossil-free economy [26]. Having an efficient way to track methane leaking from pipes, and wells would help cut around 75% of the current methane emissions [27]. The early detection of methane would help avoid significant emissions, restore the leaked gases, and increase economic savings.

Blending hydrogen with natural gas makes the early detection of any leaking incident more important. The main component of natural gas is methane, and its leaking is highly undesirable if the net zero emission target is to be met. Optical sensors, calorimetric sensors, pyroelectric sensors, semiconducting metal oxide sensors, and electrochemical sensors have been demonstrated for their ability to detect the presence of natural gas [28]. These sensors are feasible because of their ability to detect methane. However, most of them are not a practical solution for on site natural gas leaking.

1.1.3.2 Optical Sensors for Methane Detection

Optical sensors for methane detection are mainly based on infrared absorption spectroscopy. They bring the ability to perform non destructive measurements based on a physical interaction rather than a chemical reaction. Methane has specific wavelength absorption lines in the IR region which is directly related with its chemical bonds. Methane has two weak absorption lines in the short wave infrared SWIR (0.8-3 μm) region which are around 1.33, 1.66 μm and 2.3 μm [29]. One strong absorption lines exists in the mid wave infrared MWIR (3-5 μm) region which is around 3.4 μm [30]. The core element for

an optical sensor is the emitter. Most of the available high power, compact sensors use SWIR sources and were proven to reach a ppm sensitivity [31]. However, most of the sensors were used inside labs under clear atmospheric conditions or using multi-pass cells. The low transmission of SWIR in harsh weather conditions raises a concern regarding the efficiency remote areas testing due to scattering and attenuation of signal. In efforts to increase the sensitivity of such sensors, the development of MWIR laser sources is needed. Methane's absorption in the MWIR is two orders of magnitude higher than in the SWIR region [32]. In addition, MWIR lasers are considered more weather-resistant lasers for their ability to surpass foggy, rainy and harsh weather conditions [33].

Researchers have studied and implemented new techniques to develop MWIR lasers. DFB, QCLs and VCSELs are different semiconductor laser structures that have achieved lasing in the MWIR region. [34,35]. These MWIR lasers require very complex manufacturing techniques, liquid nitrogen cooling, and a high pumping current.

Nonlinear optics has been efficiently used to develop MWIR lasers using single pass, intracavity, and optical parametric oscillator (OPO) schemes. Some of the reported nonlinear MWIR lasers suffer from low output power due to losses induced by the components used, and complexity of alignment since these lasers mix two laser signals to obtain the MWIR signal. [36,37].

Methane has another absorption line in the LWIR (8-14 μm). The absorption line of methane is considered strong. Guillaume Druart et al. [38] used a LWIR camera to prove the ability to detect and quantify methane leaking. LWIR sources are the least developed laser sources in the IR region. If found, LWIR lasers are very expensive, and the detectors that operate in the LWIR are less sensitive than their counterparts in the MWIR region.

Methane absorption spectrum from 2.5 to 10 μm is shown in Figure 1.3 (a), and the absorption spectrum from 2.5 to 4.5 μm is shown in Figure 1.3 (b) [39].

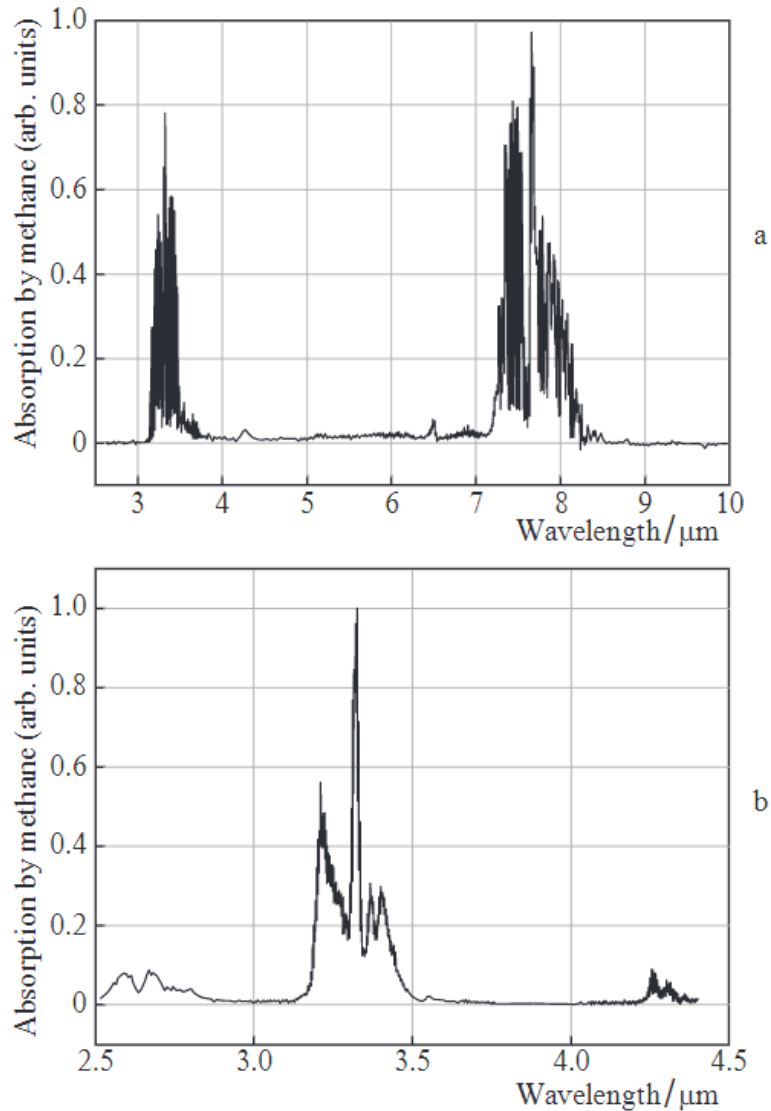


Figure 1.3: (a) Methane's absorption spectrum from 2.5 to 10 micro meter. (b) a close up on methane's absorption spectrum in the MWIR range [39]

1.1.3.3 Other Methane Sensors

Calorimetric sensors are based on a monitored combustion chemical reaction that occurs due to the oxidation of methane on a sensitive catalyst layer. The combustion of methane is an exothermic process that releases heat [40]. The heat increases the catalytic surface temperature. A temperature sensor is used to monitor the increase in temperature,

which is a signal of methane's presence. Calorimetric sensors are cost efficient. However, they are destructive, unable to operate for long term, and have a high operating temperature.

Semiconducting metal oxide (SMO) sensors are another type of sensors that are capable of detecting the presence of methane. Methane changes the electric resistance of an active SMO layer. This type of sensor has a long life time. However, ambient temperature, and humidity have a negative impact on the stability and sensitivity of SMO sensors [41].

1.1.4 Hydrogen vs Methane

In search for an alternative energy sources, hydrogen (H_2) comes into the picture. The combustion of natural gas is not very environmentally friendly since it emits some air pollutants [42]. However, hydrogen has key criteria that makes it a great candidate to replace gasoline and natural gas [43-46]. Two of these criteria are cleanliness and convenience, which make hydrogen feasible to use for the purpose of near net zero emission. The only concern about the use of hydrogen is the safety of production, transport, and storage [47]. These safety concerns along with some catastrophic events involving hydrogen leaking, such as the hydrogen tank rupture in Frankfurt in 1991, have affected the popularity of hydrogen [48].

Nevertheless, it is expected that by 2040, hydrogen use shall help reduce global carbon dioxide emission by 20% [49].

Hydrogen is the first element on the periodic table making it the lightest element by molecular weight. Methane is eight times heavier than hydrogen by molecular weight. Knowing this, the probability of hydrogen slipping through cracks, joints and connections is much higher than the leaking of methane [50]. The combustion process of hydrogen doesn't result in carbon dioxide generation which makes it a very clean process. In addition, hydrogen has a wide range of flammability from 4% to 75% when mixed with air, while methane's range of flammability is 7% to 20% [50]. As a result, hydrogen would combust with high and low air presence making the control of unwanted combustion incidents

harder than methane. Furthermore, the flame speed of hydrogen is 200-300 cm/s while methane's flame speed is only 30-40 cm/s [50]. The flame speed of hydrogen is approximately 10 times higher than methane's flame speed which results in an extra added flame control challenge. Hydrogen has a higher heating value compared to methane. Burning one pound of hydrogen would produce 2.5 times the energy obtained from burning one pound of methane. However, hydrogen is less dense than methane, so in order to get the same energy produced by burning one cubic foot of methane, 3 cubic feet of hydrogen is needed [50]. Table 1.1 shows a summary for the comparison of methane and hydrogen properties.

	Hydrogen	Methane
Chemical Formula	H ₂	CH ₄
Molecular Weight	2	16
Flammability Limit	4%-75%	7%-20%
Flame Speed	200-300 cm/s	30-40 cm/s
Heating Value	51623 Btu/lb	21518 Btu/lb

Table 1.1: Hydrogen vs Methane Comparison

Fluid dynamics suggests that hydrogen's leaking rate is 3 times faster than methane's, which is due to the molecular size of hydrogen. However, a recent study [51] shows that small leaks of mixed natural gas and hydrogen happen at the same rate. Methods used to detect methane can be the base point for detecting mixed natural gas leaks.

1.1.5 Challenges with Hydrogen Blending

Many challenges for mixing hydrogen into natural gas exist and researchers have been trying to come up with solutions to overcome them. Pipeline compatibility is one of these challenges. The presence of hydrogen might affect the pipeline's mechanical properties and response to tension stress. This change in mechanical properties affect the yield point of a pipeline making it more brittle, which raises a concern about sudden and catastrophic pipe damage occurrence. The embrittlement effect is a concern for some type

of high strength steel pipes. However, newly installed ductile metallic iron and copper pipes are more free from these concerns. [52]

Another concern is the tolerance of end-use equipment. The blend ratio of hydrogen/natural gas is limited by the maximum allowable capacity that the end-use equipment can handle. As a result, a precise method is needed to fine tune and monitor these ratios prior to supplying equipment with the mixture.

Since hydrogen has one-third the volumetric energy density that methane has, an increased volume of hydrogen shall be supplied to meet the same calorific value of pure mixed gas. This raises a concern regarding the pipelines and storage units' capacities. The rule of thumb method to overcome this is to operate at higher pressures [17].

Furthermore, the cost of hydrogen production is relatively high compared to other fuel sources, so accounting for the amount of supplied hydrogen is important in case a premium is to be paid for low carbon gas.

1.1.6 Current Projects in Canada

Many ongoing projects in Canada focus on blending hydrogen into existing natural gas infrastructure. First, the Alberta-ATCO project was initiated in 2020, and it has been awarded \$2.8 million funding to construct the biggest blending facility. The volumetric percentage of the hydrogen blending is 5% [53].

Second, the Enbridge Gas and Cummins project was initiated in 2020 and has received more than \$5 million in funding aiming to blend hydrogen with natural gas to limit greenhouse gas emissions in Canada [54].

Third, British Columbia- FortisBC aims for using the 50,000 km gas infrastructure in British Columbia to deliver mixed hydrogen and natural gas [55].

Fourth, the Quebec – Evolugen and Gazfiere project was started in 2021 to reduce greenhouse gas emission by 15,000 metric tons/year. The project aims at building one the Canada’s biggest green hydrogen facilities using water electrolysis [56].

1.1.7 Gas Quality Tracking

One of the challenges that was previously described is the need to have an accurate method to measure the calorific value of a mixed gas. Gas quality tracking is important for many reasons, and one of these reasons is to be able to measure the supplied energy from a fuel. End users pay fuel bills based on the supplied energy, and the code of practice for gas billing states that the billing error shall not exceed 2% [57].

End use appliances have a specific acceptable tolerance for hydrogen content in fuels, which raises another reason to precisely measuring the calorific value at the different positions in a distribution line to keep track of the hydrogen content.

Fiebig et al. [57] proposed an analytical and simulated solution for calculating the calorific value of mixed natural gas. The simulation that was done on SMARTSIM requires input data such as pipe layout, diameter, roughness, and calorific values at entry points and exit volumes. The method showed a high accuracy in predicting the calorific values, but it is a complex process that would be difficult to scale to single distribution line and exit line.

Gas calorimetry is another method used to determine the calorific value of a gas. The methods used is gas calorimetry are based on the combustion of a sample inside a calorimetric bomb or in an open flame gas burner. The concept of these instruments is based on the first law of thermodynamics and the conservation of energy. The heat generated is transferred to a heat absorbing fluid that results into a temperature increase in the fluid. The temperature increase is equivalent to the calorific value of the fuel [58].

A correlation method for measuring the calorific values of mixed gas has been also studied [59] when the permittivity of the mixed gas is correlated with the calorific value.

1.2 Calorific Measurement and Leak Detection Proposed Solution

This thesis tackles two main issues that were previously described. The first issue is the need to measure the calorific value of the mixed gas. A calibration method based on ultrasonic techniques is used to determine the calorific value of mixed gas. Using the speed of sound inside a gas mixture, gas tracking is achieved and the calorific value is obtained. Combining the calorific measurement with the volumetric flow rate, the complete energy flow rate can be obtained.

The second goal is to design and test a high efficiency mid-wave infrared (MWIR) laser source. The MWIR laser source proposed uses nonlinear optics and, specifically, difference frequency generation to obtain lasing in a wavelength region that is suitable for methane detection. The advancement of MWIR emitters is needed in order to come up with sensors with a high mixed natural gas leak detection sensitivity.

Potential long-wave infrared (LWIR) generation using the same MWIR difference frequency generation (DFG) concept is also analyzed.

Such research is required to lay the road towards net zero emission goals set by Canada and other countries.

1.3 Thesis Structure

Chapter 2 describes the theory of ultrasonic mixed gas detection, MWIR generation using nonlinear optics (difference frequency generation) and phase matching. It also provides a description on periodically poled lithium niobate crystals.

Chapter 3 describes the experimental and simulation work done to achieve high detection accuracy for mixed gases content.

In chapter 4, MWIR DFG simulation is presented. The test setup is discussed as well as the experiments that were done to achieve MWIR DFG power. A comparison between the simulation and experimental results is analyzed, and the potential of the experimental

results is illustrated. In chapter 5, LWIR DFG test setup is described. Experimental and simulation results are compared.

Chapter 6 concludes the thesis and its findings.

Chapter 2

2 Basic Theories on Ultrasonic Transducers and Diode Pumped Solid State Lasers

2.1 Ultrasonic Technology

Non-destructive testing has driven the advancement in ultrasonic measurement techniques. The main component used in these measurements is the ultrasonic transducer. Ultrasonic transducers are responsible for generating and receiving acoustic wave. An ultrasonic transmitter works by converting an electrical voltage to displacement, and an ultrasonic receiver converts the mechanical displacement to voltage. The structure of ultrasonic transducers consists of an active piezoelectric plate, backing element, and a matching layer [60]. The different components are coupled together and an electrical lead is used to supply the active layer with voltage as shown in Figure 2.1.

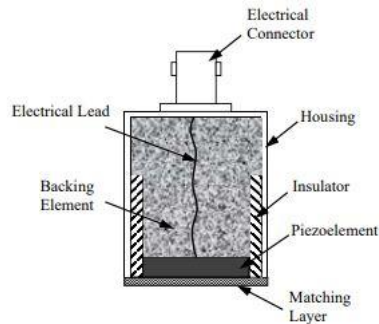


Figure 2.1: Ultrasonic Transducer Structure [60]

2.1.1 Piezoelectric Element

Due to the nature of some “smart” materials, two modes of operations can be seen. The first mode is the direct piezoelectric effect in which an applied force on the material gets converted to displacement in the material that produces an electric field. The second phenomenon is the inverse piezoelectric effect in which the voltage applied to the piezoelectric material results in material displacement.

These physical phenomena can be mathematically described with some governing equations [60].

Normal and shear stresses can be expressed as a stress vector.

$$[T] = [T_x \ T_y \ T_z \ T_{xy} \ T_{xz} \ T_{yz}]^t \quad (2.1)$$

Where $[T]$ is the stresses matrix, T_x , T_y , T_z are the normal stresses, and T_{xy} , T_{xz} , T_{yz} are the shear stresses.

The Strain Vector can be written as:

$$[S] = [S_x \ S_y \ S_z \ S_{xy} \ S_{xz} \ S_{yz}]^t \quad (2.2)$$

Where $[S]$ is the strain matrix, S_x , S_y , S_z are the normal displacements, and S_{xy} , S_{xz} , S_{yz} are the shear strain.

The displacement $[D]$ and Electric field $[E]$ vectors can be written as:

$$[D] = [D_x \ D_y \ D_z] \quad (2.3)$$

$$[E] = [E_x \ E_y \ E_z] \quad (2.4)$$

For piezoelectric materials the stress-strain equation is written as follows:

$$[T] = [C][S] - [e]^t[E] \quad (2.5)$$

Where $[C]$ is known as a 6 x 6 elastic stiffness matrix, and $[e]$ is a 3 x 6 piezoelectric constant matrix.

The piezoelectric constant matrix [e] can be written as follows:

$$[e] = \begin{bmatrix} e_{11} & \cdots & e_{16} \\ \vdots & \ddots & \vdots \\ e_{31} & \cdots & e_{36} \end{bmatrix} \quad (2.6)$$

Where e_{ij} are the piezoelectric constants

The displacement vector can be written as:

$$[D] = [e][S] + [P][E] \quad (2.7)$$

Where [P] is the 3 x 3 permittivity matrix that can be expressed as:

$$[P] = \begin{bmatrix} P_{11} & \cdots & P_{13} \\ \vdots & \ddots & \vdots \\ P_{31} & \cdots & P_{33} \end{bmatrix} \quad (2.8)$$

Where P_{ij} are the permittivity constants.

These governing equations for the electro-mechanical behaviour of the material set the basis for designing such materials.

The efficiency of a certain piezoelectric material is defined as the ratio between the supplied energy and energy stored in the material [61].

We define [B] and k factor as:

$$[B] = [C] + [e]^t[P]^{-1}[e] \quad (2.9)$$

$$k = \frac{e_{33}}{\sqrt{B_{33} * P_{33}}} \quad (2.10)$$

The physical meaning of k is an efficiency measurement. It is material dependant as seen in equation (2.10). It depends on the piezoelectric constant, permittivity, and elastic stiffness of the piezoelectric materials.

The most widely used piezoelectric materials employed in ultrasonic transducers are: lead-zirconate-titanate (PZT), lithium niobate (LiNbO₃), and α -quartz (SiO₂) [61].

2.1.2 Matching Layer

The matching layer is a layer that is placed on top of the piezoelectric active layer. This layer usually comes in direct contact with the test medium whether it is a gas, liquid, or solid. The thickness t_m of this matching layer is directly related to the resonant wavelength of the piezoelectric layer as:

$$t_m = \frac{\lambda_r}{4} \quad (2.11)$$

In addition, the matching layer shall be chosen in a way to satisfy Equation (2.12)

$$Z_m = \sqrt{Z_p * Z_g} \quad (2.12)$$

Where Z_m , Z_p and Z_g are the acoustic impedances of the matching layer, active layer, and test medium.

By carefully selecting the matching layer material and thickness, the best coupling can be achieved between the transducer and the test medium.

Different ultrasonic transducers work in specific mediums, and one of the specifications that determine the compatibility of a transducer with a certain test medium is the matching layer impedance.

2.1.3 Backing Element

The backing element has two main characteristics. First, the acoustic impedance of the backing element determines how much energy can be transferred from the active element to the backing element. It is desired that the transmitted signal to the backing element gets attenuated without being reflected back to the active layer. Second, the backing element plays an important role in attenuating the noise and reducing the signal to noise ratio in an ultrasonic transducer [62]. Epoxy based backing elements have the desired attenuation coefficients that enables them to act as a backing element [63].

2.1.4 Coupling

The different layers of an ultrasonic transducer have to be coupled together. Bonding these layers can be done in three different methods. The first method is dry bonding which consists of applying a high pressure to the components to be bonded. The drawback of this method is that the active layer is usually thin and some materials can not withstand the high pressure.

The second method is through liquid couplers in which the different components are bonded together using silicone oil, or glass solders. Liquid couplants melt and couple the ultrasonic components together. This method induces corrosivity and thermal stresses which might affect the efficiency and lifetime of the ultrasonic transducers [60].

The third method is based on solid adhesion such as soldering, diffusion bonding, and sol-gel techniques are used to bond the backing element, piezoelectric component and matching layer together. Solid coupling has shown improved performances in a wide operating temperature and pressure ranges [60].

2.2 Ultrasonic Techniques for Gas Flow Rate Measurements

Ultrasonic transducers can be used to measure the flow rate without inducing any moving parts to the flow, and with high accuracy. There are two types of ultrasonic flow meters. The first type is called a doppler type where the shift in frequency between the main ultrasonic signal emitted by the ultrasonic transducer, and the frequency of a reflected ultrasonic wave from the interaction with the fluid flow is measured. The shift in frequency is directly related to the flow velocity. However, the fluid shall contain some contaminants that would help in reflecting the ultrasonic wave [64].

The second method uses the transit time of the ultrasonic wave. In this method, the time that the ultrasonic wave takes to travel between two transducers is used to calculate the velocity of the flow. Two types of transducers can be used for this purpose which are clamp on that are placed outside the pipe, or wetted transducers placed inside the pipe.

In the clamp on transducers case, the pipe surface is required to be as smooth as possible to ensure that the ultrasonic wave penetrates and exits the pipe. However, In the case of the second method, where transducers are installed inside the pipe, there are less limitations regarding the surface quality of the pipe.

Figure 2.2 shows a setup for transit time method with wetted ultrasonic measurement technique.

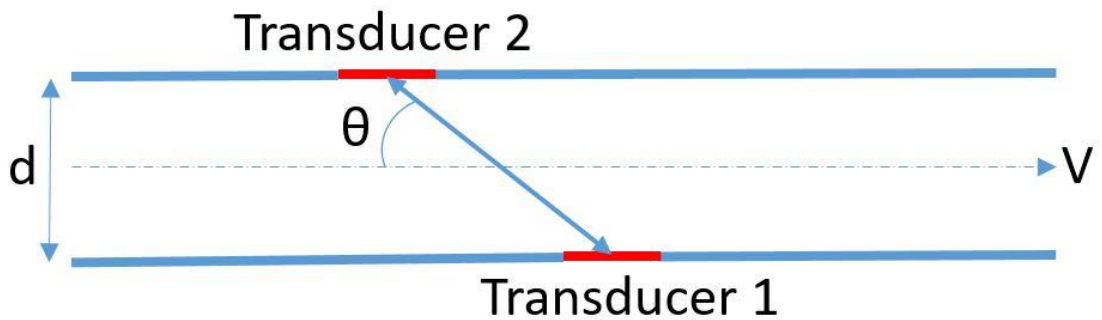


Figure 2.2: Wetted Transit Time Flow Rate Measurement Setup

The velocity of the flow affects the time needed for the signal to travel from the transmitter to the receiver. In case the signal is sent from transducer 1 and received on transducer 2 (t_1 against the flow), it would take more time for the signal to reach the receiver than when it is sent from transducer 2 and received in transducer 1 (t_2 with the flow). The acoustic path (L) is the distance between transducers 1 and 2.

T_1 can be expressed as written in Equation (2.13)

$$t_1 = L/(V_s - V\cos\theta) \quad (2.13)$$

Where V_s is the speed of sound in the medium.

T_2 can be expressed as written in Equation (2.14)

$$t_2 = L/(V_s + V\cos\theta) \quad (2.14)$$

As a result, the time difference between the upstream and downstream ($t_1 - t_2$) is

$$\delta t = \left[\frac{2L \cos \theta}{V_s^2 - V^2 \cos^2 \theta} \right] V \quad (2.15)$$

Having knowledge about the acoustic path, speed of sound in the medium, and the angle θ enables the calculation of the velocity of the flow.

The flow rate is related to the flow velocity as shown in Equation (2.16)

$$U = A * V \quad (2.16)$$

Where A is the cross sectional area of the pipe.

The ultrasonic transducers should not interfere with the flow path in order to have accurate results.

2.3 Ultrasonic Techniques for Mixed Gas Composition Measurements

The speed of sound is dependant on the medium that the wave is traveling in. Table 2.1 shows some theoretical speed of sound measurements in different gaseous mediums at 20°C and 1 Atm pressure [65].

Gas	Theoretical speed of sound (m/s)
Air	343
Nitrogen	349
Oxygen	326
Methane	446
Hydrogen	1270

Table 2.1: Theoretical Speed of Sound in Different Gases

Many conditions such as mixture composition and temperature affect the speed of sound. At higher temperatures, the molecules have more energy which makes them vibrate faster. The speed of sound in air at 0°C is 331 m/s, while it is 343 m/s at 20°C.

The simple correlation between the change in speed of sound in air vs temperature is [66]

$$V_s = 331 + 0.6 * T \quad (2.17)$$

For mixed gases, the temperature, adiabatic constant, and molar mass are needed to calculate the theoretical speed of sound.

The speed of sound can be calculated as

$$V_s = \sqrt{\left(\frac{\gamma RT}{M}\right)} \quad (2.18)$$

Where

- γ is the mixed gas adiabatic constant
- R is the universal gas constant
- T is the mixture temperature
- M is the mixture molar mass

The adiabatic constant for the mixed gas can be determined as

$$\gamma = \frac{x_1 * Cp_1 + x_2 * Cp_2}{x_1 * Cv_1 + x_2 * Cv_2} \quad (2.19)$$

Where

- x_1 is the mole fraction of the first gas
- x_2 is the mole fraction of the second gas
- Cp_1 is the constant pressure specific heat of the first gas
- Cp_2 is the constant pressure specific heat of the second gas
- Cv_1 is the constant volume specific heat of the first gas
- Cv_2 is the constant volume specific heat of the second gas

The molar mass of the mixture can be found using Equation (2.20)

$$M = x_1 * M_1 + x_2 * M_2 \quad (2.20)$$

Where

- M_1 is the molar mass of the first gas
- M_2 is the molar mass of the second gas

By calculating the speed of sound in a mixture, the evaluation of the gas mixture components is possible.

2.4 MWIR Laser for Methane Detection

Any laser source used in gas detection has to have certain specifications. The wavelength that the source is operating at shall be in a strong absorption region of the target gas. With this wavelength specification, the absorption of the incident light is set to be high enough to detect the presence of the gas. The power level of the source shall be in the milliwatt-watt level region to avoid the noise effects on the accuracy of the measurement. The linewidth of the source shall be less than 100 kHz in order to get an optimized absorption [67]. In addition, the laser source shall have a good tunability range to be able to tune the source wavelength to get a peak that gives a maximum absorption. In the short wave infrared (SWIR), many laser sources meet the requirements stated above. For methane, one of the disadvantages of using a SWIR source is that the absorption line of the gas in the wavelength region is two orders of magnitude less than in the MWIR and LWIR regions.

Methane gas has a strong absorption line in the MWIR region which makes lasers that work in this region have a practical solution for methane detection. Table 2.2 shows the used technology to generate MWIR lasers with direct and indirect conversion.

Method	Class	References
Optical Parametric Oscillator	NLO: LiNbO ₃ , MgO:PPLN, AgGaS ₂ , etc...	[68-71]
Fiber Laser	Er ³⁺ :ZBLAN, Dy ³⁺ : ZBLAN	[72,73]
Solid-State Laser	Fe:ZnSe, Cr:ZnSe	[74,75]
Gas Laser	CO ₂	[76]
Chemical Laser	HF	[77]
Quantum Cascade Laser	AlSb, InAs	[78]

Table 2.2: MWIR Generation Methods

Each method has its own advantages and disadvantages. OPO lasers have high energy and efficiency, but the alignment and complexity of the setup is high. Fiber lasers are stable, but they have a very narrow tuning range. In addition, solid state lasers that operate in the MWIR and LWIR are hard to find due to materials limitations [79]. Gas lasers can operate at a high power, but they raise some safety concerns, and they are significantly larger than their counterparts. On the other hand, chemical lasers have good beam quality but they contain toxic products. With the advancement in quantum cascade lasers, QCLs are considered a promising choice for MWIR generation, but the output power levels are still considered poor [76]. For a high efficient QCL, the operating temperature shall be at liquid nitrogen temperature [79].

Most of the high powers MWIR lasers are OPO based and in pulsed mode. In this work, continuous wave (CW) MWIR laser is studied and implemented using nonlinear optics (NLO) DFG process.

The proposed method for MWIR generation involves diode pumped solid state laser and NLO. As a result, a brief description of DPSS lasers and nonlinear optics is discussed in the following sections.

2.4.1 Diode Pumped Solid State (DPSS) Lasers

Diode pumped solid state lasers (DPSS) are lasers that use semiconductor laser diodes to pump rare earth ion doped materials where pumping is defined as raising atoms from a lower to a higher energy levels. These rare ion earth ions are usually doped into a host material such as doping Nd^{3+} into yttrium aluminum garnet or yttrium vanadate (Nd:YAG or Nd:YVO₄). DPSS lasers are highly efficient, compact and cost effective.

Nd:YVO₄ has outstanding features that put it in a great position to be used as the fundamental crystal of diode pumped solid state lasers. Nd:YVO₄ has a strong absorption coefficient at 808nm. In addition, it has a strong stimulated emission cross section. The laser output of the Nd:YVO₄ is linearly polarized and the absorption of the pump beam is

also polarization dependent. The absorption profile of Nd:YVO₄ vs pumping wavelength smoothly changes and peaks at around 808 nm [80].

Laser diodes have a larger divergence angle than the resonator mode. From a mode matching point of view, it is required that the pump beam size matches the resonator mode size. The shorter the fundamental crystal, the better the mode matching, and the reason behind that is that the beam does not diverge so much inside the fundamental crystal. Nd:YVO₄ has a strong absorption which enables the use of short crystals that can absorb the pump beam.

One of the drawbacks of Nd:YVO₄ crystals is the low thermal conductivity. Controlling the temperature of the crystal is hard because of the difficult heat dissipation. Such problems may put limitations on the operating pumping powers to avoid thermal induced fractures in the crystal. In case thermal induced fracture is noticed, moving to lower doping concentrations might solve the heat dissipation problems.

The energy level diagram of Nd³⁺ ion doped into yttrium vanadate is shown in Figure 2.3 [81].

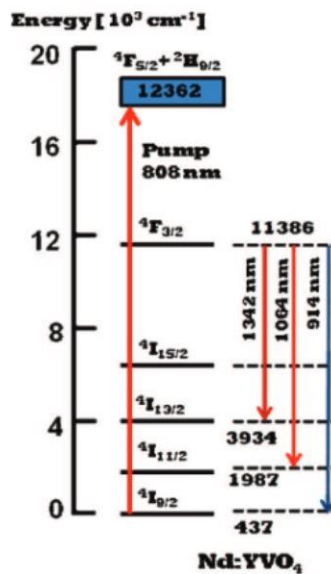


Figure 2.3: Energy Level Diagram of Nd:YVO₄ [81]

Pumping Nd:YVO₄ with a 808nm pump source, excites the electrons inside the atom from the ground state to a higher level energy state ($^4I_{9/2} \rightarrow ^4F_{5/2}$ Transition). The excited electrons relax from $^4F_{5/2}$ to $^4F_{3/2}$ with a fast relaxation rate. The transitions from $^4F_{3/2}$ determine the emitted wavelength.

- $^4F_{3/2} \rightarrow ^4I_{13/2}$: 1064nm emission line
- $^4F_{3/2} \rightarrow ^4I_{11/2}$: 1342nm emission line
- $^4F_{3/2} \rightarrow ^4I_{9/2}$: 914nm emission line

To favor one emission over the others, optimizing the coating of Nd:YVO₄ and the cavity conditions is a must.

Pumping with 808nm might induce thermal damage in the Nd:YVO₄, so as an alternative, in case thermal induced damage persists, pumping with 880nm excites the electrons from $^4I_{9/2}$ to $^4F_{3/2}$ instead of $^4F_{5/2}$ and might help solve the thermal damage issues [80].

Nd:YVO₄ DPSS lasers are known as four levels lasers as shown in Figure 2.4.

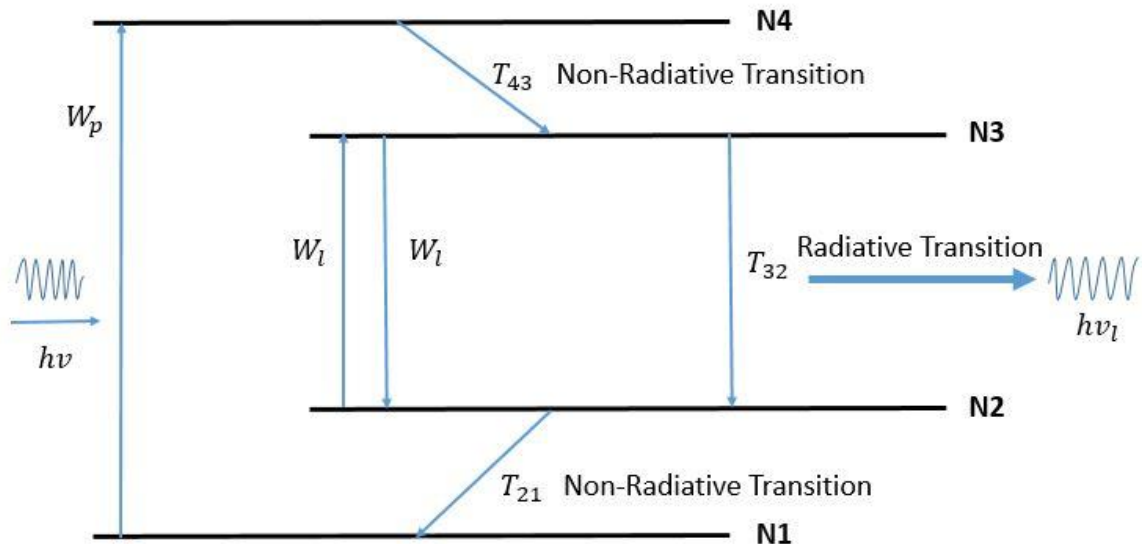


Figure 2.4: Four Level Laser System

The rate of change in the population of each layer is described by the four level laser rate equations [82].

$$\frac{dN_1}{dt} = -W_p N_1 + T_{21} N_2 \quad (2.21)$$

$$\frac{dN_2}{dt} = W_l (N_3 - N_2) + T_{32} N_3 - T_{21} N_2 \quad (2.22)$$

$$\frac{dN_3}{dt} = T_{43} N_4 + W_l (N_2 - N_3) - T_{32} N_3 \quad (2.23)$$

$$\frac{dN_4}{dt} = W_p N_1 - T_{43} N_4 \quad (2.24)$$

Where

- $W_p N_1$ is the effective pumping rate
- T_{21} is the spontaneous decay rate between levels 1 and 2
- T_{32} is the spontaneous decay rate between level 2 and 3
- T_{43} is the spontaneous decay rate between levels 3 and 4
- W_l is the stimulated transition rate between levels 2 and 3

Through working with Equations (2.21-2.24) at steady state where $\frac{dN_i}{dt} = 0$. Some necessary conditions for lasing and population inversion are concluded:

- $T_{21} > T_{32}$
- A feedback resonant cavity
- Gain per round trip is larger than loss per round trip

A simple Nd:YVO₄ DPSS laser resonator cavity is shown in Figure 2.5.

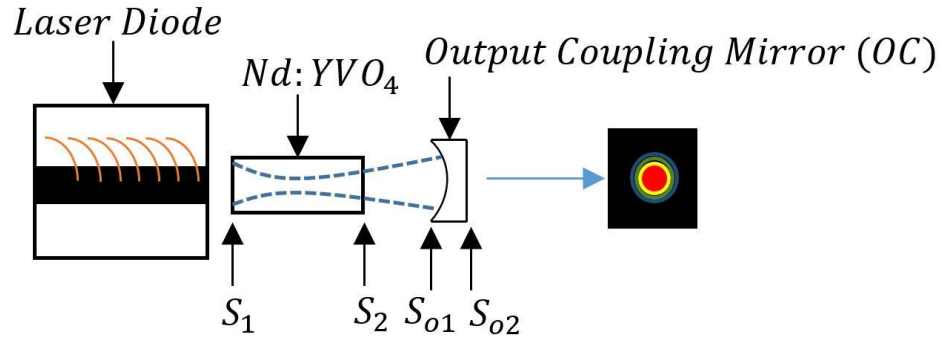


Figure 2.5: Simple Nd:YVO4 Resonator Cavity

S_1 is coated in a way to act as a first mirror in the resonator cavity. It passes 808nm pump, and reflects the wavelength of interest that has to be generated from the cavity (1064nm or 1342nm). S_2 is anti reflection coated at the wavelength of interest.

The output coupling mirror (OC) is the second mirror to complete the resonator cavity. The OC can be plano-plano, or plano-concave with S_{o1} coated with high reflectivity coating at the wavelength of interest and S_{o2} is coated with anti reflection coating at the wavelength of interest.

2.4.2 Nonlinear Optics

The interaction of an optical frequency electric field E with a dielectric material results in a polarization P such as:

$$P = \epsilon_0 \chi E \quad (2.25)$$

Where ϵ_0 is the dielectric permittivity of vacuum, χ is the dielectric susceptibility.

The dielectric susceptibility can be written as a function of optical frequency electric field as:

$$\chi = \chi^{(1)} + \chi^{(2)} E + \dots + \chi^{(n)} E^{n-1} \quad (2.26)$$

Where $\chi^{(i)}$ are the i^{th} nonlinear coefficients.

As a result, Equation (2.25) can be written as

$$P = \epsilon_0(\chi^{(1)} + \chi^{(2)}E + \dots + \chi^{(n)}E^{n-1})E \quad (2.27)$$

The high order nonlinear susceptibility dependency on electric field helps in generating new optical frequencies [83]. Usually, the second order susceptibility is much larger than the higher orders.

$$\chi^{(2)} \gg \chi^{(3)} \gg \dots \gg \chi^{(n-1)} \quad (2.28)$$

The second order nonlinear interaction has more research interest than the higher orders since it is the strongest interaction.

Assume an electric field that is composed from the superposition of two field with frequencies ω_1 and ω_2 . The total electric field is written as:

$$E = E_1e^{i\omega_1t} + c.c + E_2e^{i\omega_2t} + c.c \quad (2.29)$$

The second order nonlinear polarization term is:

$$P = \epsilon_0 \chi^{(2)}E^2 \quad (2.30)$$

$$= \epsilon_0 \chi^{(2)}(E_1e^{i\omega_1t} + c.c + E_2e^{i\omega_2t} + c.c.)^2$$

$$= 2(|E_1|^2 + |E_2|^2) + (E_1^2e^{i2\omega_1t} + c.c + E_2^2e^{i2\omega_2t} + c.c) + (2E_1E_2e^{i(\omega_1+\omega_2)t} + c.c.) + (2E_1E_2e^{i(\omega_1-\omega_2)t} + c.c.)$$

- First term in Equation (2.30) represents the DC frequency component
- Second term represents the second harmonic generation (SHG)
- Third term represents the sum frequency generation (SFG)
- Fourth term represents the difference frequency generation (DFG)
- c.c represents a complex conjugate

The photon transition for the different interactions that can occur is shown in Figure 2.6.

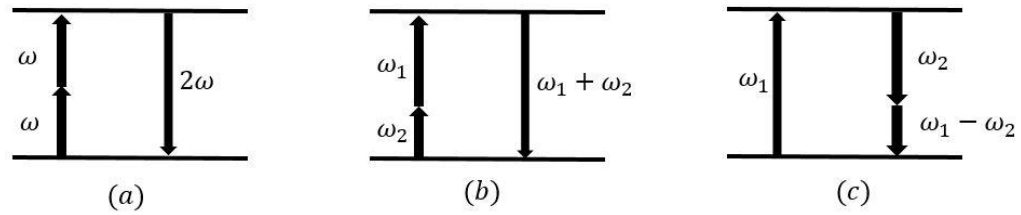


Figure 2.6: Nonlinear mixing schematics: (a) second harmonic generation (SHG), (b) sum frequency generation (SFG), and (c) difference frequency generation (DFG)

The second harmonic generation is a special case of the sum frequency generation where $\omega_1 = \omega_2 = \omega$ which means the two photons at a certain frequency create one photon at a frequency $\omega' = 2\omega$. In SFG, one photon at a frequency ω_1 annihilates with another photon at a frequency ω_2 to create a photon with a frequency $\omega' = \omega_1 + \omega_2$. In a DFG process, one photon at a frequency ω_1 interacts with another photon with a frequency ω_2 in a nonlinear medium to create one photon with a frequency $\omega' = \omega_1 - \omega_2$.

Some of the requirements for these interactions to happen are:

- The nonlinear medium shall be transparent in the wavelength range that it is going to be operating in.
- The nonlinear coefficient for the nonlinear medium shall be high enough to ensure an efficient process.
- Momentum conservation or phase matching shall be satisfied.

2.4.3 Phase Matching

The wave vector associated with each wave is defined as:

$$k_i = \frac{2\pi n_i}{\lambda_i} \quad (2.31)$$

The wave vector is dependent on the wavelength and the refractive index of the medium in which it is traveling. The difference in momentum among the involved waves in a nonlinear interaction is noted as Δk . In the DFG case, the pump (ω_1), the signal (ω_2), and the idler ($\omega_3 = \omega_1 - \omega_2$) have the following phase matching term:

$$\Delta k = k_1 - k_2 - k_3 \quad (2.32)$$

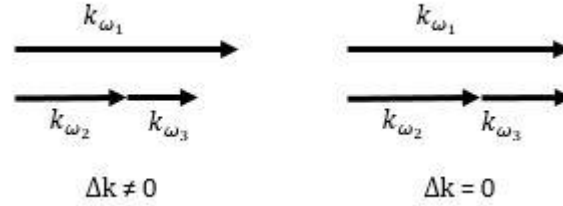


Figure 2.7: Non-phase matched, and phase matched wave vectors

When $\Delta k \neq 0$, it means that the signal and the idler drift out of phase over a distance $L_c = \frac{2\pi}{\Delta k}$.

In the case of SHG, when $\Delta k \neq 0$, it means that the generated wave and the pump wave propagate in the crystal at different speeds, and at a certain point in the crystal they become out of phase.

To solve the issue of phase mismatch, two main methods are used. First, with birefringent phase matching the different waves are polarized and experience different refractive indices at ordinary and extraordinary polarizations. By turning the nonlinear crystal with a certain angle, and operating at a certain temperature, phase matching could be achieved.

Second, quasi-phase matching (QPM) is another solution for the phase mismatching. During QPM, the of the second order nonlinear coefficient is converted at each coherence length. QPM can be achieved with periodically poling the nonlinear crystal. Figure 2.8 shows the quasi-matching effect on the wave vectors.

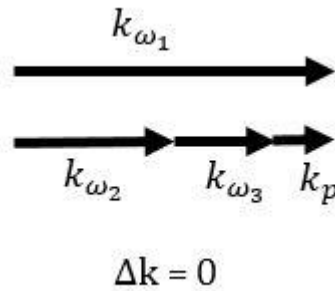


Figure 2.8: QPM phase matching

The QPM phase matching equation can be written as:

$$\Delta k = k_1 - k_2 - k_3 - k_p \quad (2.33)$$

Where $k_p = \frac{2\pi}{\Lambda}$, and Λ is period of the crystal poling. With the help of temperature control, poled crystals can reduce the phase mismatch to zero.

2.4.4 Periodically Poled Lithium Niobate

The physical properties of lithium niobate such as piezoelectric effect, and nonlinear optical effect make it attractive for many researchers. In birefringence phase matching (BPM), the polarization limitation affects the nonlinear conversion efficiency. The small nonlinear coefficient $d_{31} = 2.1 \text{ pm/V}$ of lithium niobate is used in BPM. In QPM, the largest effective nonlinear coefficient $\frac{2}{\pi}d_{33} = 17 \text{ pm/V}$ is used [84].

Lithium niobate has a strong spontaneous polarization at temperatures below 1210 °C. Applying an external electric field to the crystals results in a domain inversion which is a change in the polarization direction. By studying the mixing process that the nonlinear crystal is supposed to perform, the poling period can be calculated by applying an appropriate electric field at certain locations. Figure 2.9 shows the process used to obtain domain inversion [84].

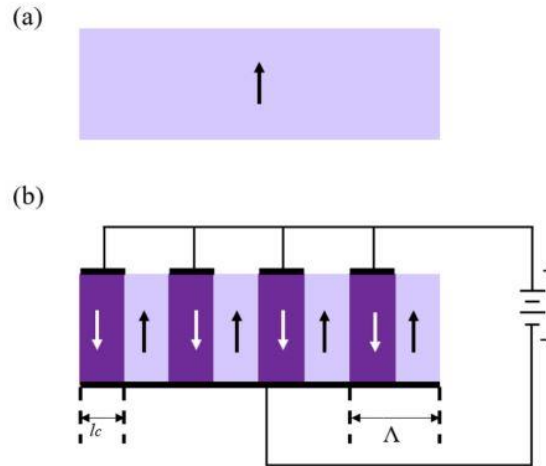


Figure 2.9: (a) Initial spontaneous polarization of a lithium niobate crystal. (b) domain inverted PPLN obtained with an external electric field application [84]

The damage threshold for PPLN is relatively low compared to other nonlinear crystals. MgO doping is used to enhance the damage threshold. 5mol% MgO doping in PPLN crystals has a significant effect on the damage threshold and stability.

The fabrication steps of PPLN involve:

- Preparation of wafer
- Spinning photoresists
- Preparation and alignment of masks with the intended half period openings
- UV light exposure for the photoresist
- Thin film deposition
- Etching

With the advancements in micro fabrication, these steps have been highly developed during the last years.

2.4.4.1 Cavity Enhanced Nonlinear Process

Figure 2.10 shows the different structures discussed in 2.4.4.1. The simplest structure that a PPLN can be used in is a single-pass setup as show in in Figure 2.10 (a). In

the single-pass setup, the PPLN, or any other nonlinear crystal used, is positioned outside the resonator cavity where the output of the cavity interacts with the PPLN after the output coupling mirror. In single pass configurations, the limited interaction length requires long crystals and high intensities to realize an efficient nonlinear process. In case such a source is not available, cavity enhanced designs can be used to achieve better conversion efficiencies as the resonator increases both the effective interaction length and the intensity, which is controlled with the cavity design. An external-cavity design is achieved by placing the PPLN within two mirrors that can circulate the fundamental wavelength output from the fundamental resonator as shown in Figure 2.10 (b). In this method, multiple passes of the fundamental wave are achieved which improves the efficiency of the system. If a more compact setup is required, an intracavity nonlinear PPLN design is a potential solution. Putting the PPLN crystal inside the fundamental cavity enables the access for a high intracavity power that is available for the nonlinear conversion without requiring an additional external cavity. Two main things shall be taken into consideration in case of an intracavity structure are the damage threshold of the PPLN, and the loss that is induced to the fundamental wavelength due to inserting the PPLN inside the fundamental resonator cavity.

The simplest intracavity structure is the straight linear cavity as shown in Figure 2.10 (c). However, more complex setups can be used such as folded and ring cavities as in Figure 2.10 (d). These more complicated forms of intracavity can help optimize the cavity mode size. All of these setups have been explored for different nonlinear interactions such as SHG, SFG, OPO, DFG, and SPDC. Table 2.3 lists some of the research activities along with the method and structure used working with periodically poled lithium niobate.

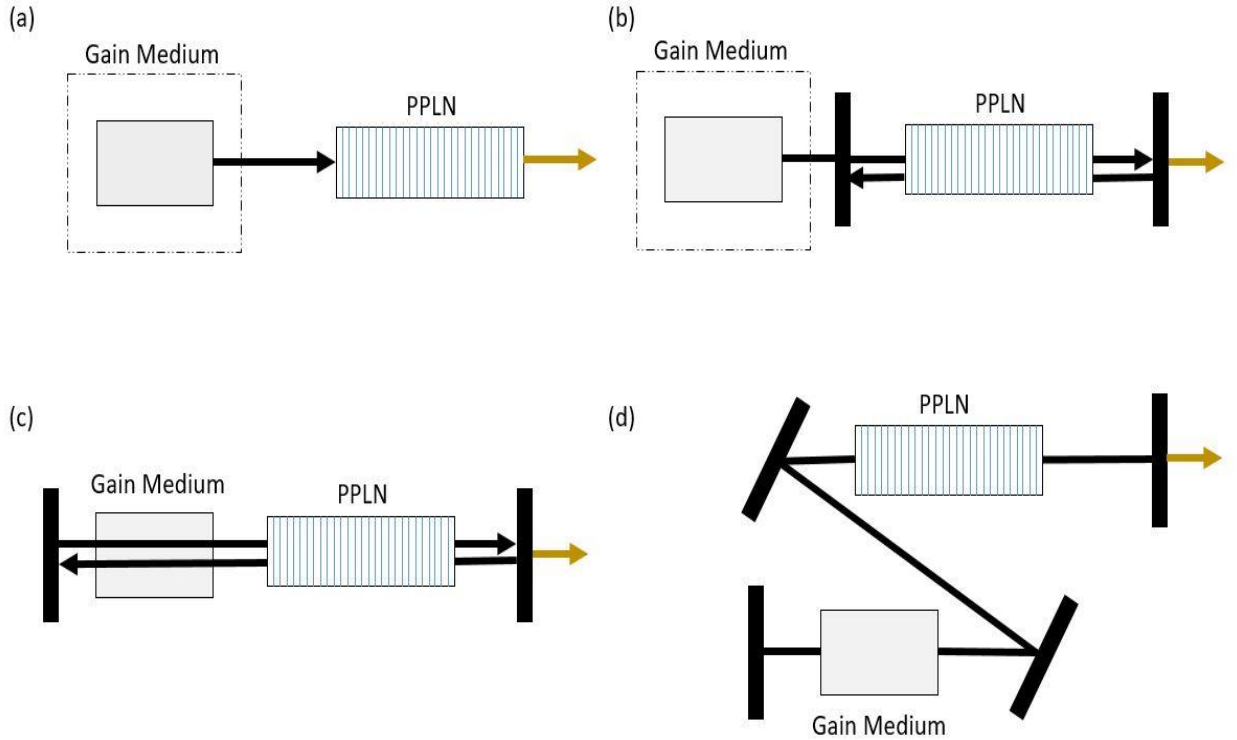


Figure 2.10: (a) Single pass structure, (b) extracavity structure, (c) intracavity structure, and (d) folded intracavity structure

The use of an intracavity structure has an advantage of reducing the required pumping power which directly affects the required electrical power to operate the pumping source. Intracavity structures are a promising solution to increase the O-O efficiency. However, the coating conditions shall be optimized in order to minimize the loss at the fundamental wavelength induced by inserting the PPLN inside the cavity.

Cavity Type	Nonlinear Process	Idler/output wavelength (μm)	Reference
Single pass Structure	SHG	0.532, 0.78, 1.18	[85-87]
Intracavity Structure	SHG	0.532, 0.561	[88,89]
Extracavity Structure	OPO	2.5-3.6	[90]
Intracavity Structure	OPO	2.1	[91]
Intracavity Structure	DFG	3.141	[92]

Table 2.3: Different Structures and nonlinear processes using PPLN crystals

2.4.5 MWIR and LWIR for gas Detection

Away from the absorption lines of some gases such as methane and carbon dioxide, MWIR and LWIR are rarely absorbed in the atmosphere. This gives MWIR and LWIR lasers another advantage by ensuring that the only absorption effect is happening due to the presence of a certain gas. Figure 2.11 shows the absorption lines of different gases in different atmospheric windows [93].

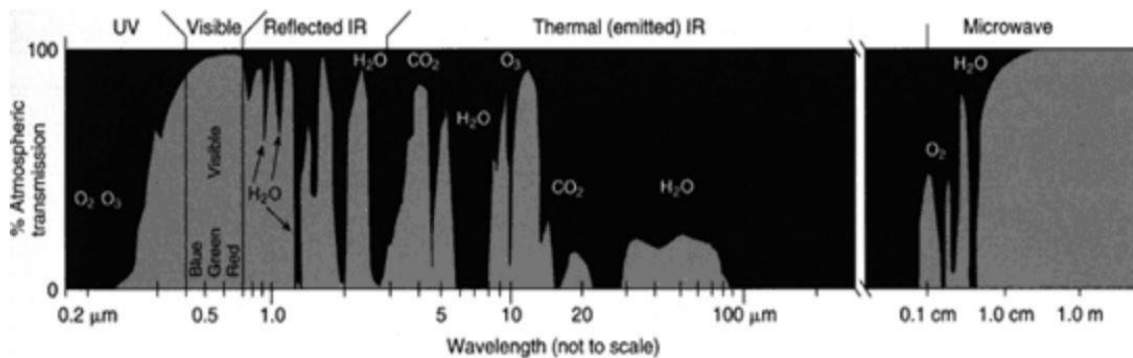


Figure 2.11: Atmospheric transmission (%) vs wavelength (μm) [93]

Highly developed SWIR sources are commercially available, and there have been successful direct absorption spectroscopy experiments where sources that operate in the SWIR region were used. The Greenhouse Gas Observing Satellite (GOSAT), TROPOMI satellite, and AVIRIS-NG are examples of satellite missions that used a SWIR source to detect methane leaks and presence in the atmosphere [94]. These satellites offer a great tool for methane detection. However, on site SWIR based laser detectors have some disadvantages which are [79]:

- Low transmission in harsh weather conditions (might give false positive readings)
- Inability to detect low methane's concentrations due to low total absorption
- Long range measurements are hard due to scattering and attenuation of signal

Sources with wavelengths higher than 1500 nm are safer to human eyes than the ones that operate at shorter wavelengths. As a result, higher power sources can be used without raising a lot of human safety concerns. MWIR and LWIR sources and detectors are not as commercially available as their SWIR counterparts. However, they have some promising characteristics that fit the requirements for highly accurate methane detection. The advantages of MWIR and LWIR lasers are [79]:

- High transmission in the atmosphere with minimal attenuation
- Highly absorbed by methane
- Long range measurement is much more feasible

The disadvantage of using MWIR or LWIR lasers is that they are not as commercially available as their SWIR counterparts.

Using a difference frequency generation process MWIR and LWIR wavelengths can be obtained from a pump and a signal source that operate in the SWIR region. The signal source can be 1550 nm to take advantage of the availability of great 1550 nm optical components. PPLN can be used for MWIR generation due to its transparency in this region (up to 4.5 microns). However, for LWIR, a potential candidate is orientation patterned semiconductors (OP-SCs) such as gallium arsenide or gallium phosphide which are

transparent up to $18 \mu\text{m}$. OP-SCs are still in an early stage of development, and it is relatively harder to manufacture when compared with PPLNs [79].

Chapter 3

3 Calorific Measurements for Mixed Natural Gas Using an Ultrasonic Calibration Technique

3.1 Introduction

The calorific value of a gas is a value that shows the energy content in a certain volume or mass of the gas. Calorific values of gases are usually obtained by combusting a certain quantity of the gas and checking the heat produced from the combustion process in a destructive experiment. Each gas has a certain calorific value, so when mixing different gases, the calorific values of the mixture changes with respect to the concentrations of the components. In mixed natural gas, it is important to measure the calorific value to be able to price the supplied gas, and to comply with the energy tolerance of the end use equipment as discussed in Section 1.1.7.

Ultrasonic transducers have been used in many non-destructive measurement technologies such as flaw detectors in solid materials, gas flow meters, and distance measuring devices. One potential utilization of ultrasonic transducers is in mixtures composition testing. Speed of sound in a medium depends on the constituents of the medium that the ultrasonic wave is traveling in. The design of an ultrasonic transducer highly affects whether it works in a specific medium or not. As a result, not all ultrasonic transducers are entitled to work in a gaseous medium.

In this chapter, many ultrasonic transducers are tested to choose one that works for gas measurements. The suitable ultrasonic transducer is then used for a proof of principle experiment to test the composition and flow rate of a mixed gas. Using the background theory discussed in Section 2.3, the composition of a mixed gas can be determined. The

feasibility and accuracy of the measurement technique is analyzed and compared with simulation/theoretical results.

3.2 Ultrasonic Transducers Testing

Many transducers have been tested to decide on one that is suitable for a gas composition testing experiment. A list of the tested ultrasonic transducers is shown in Table 3.1.

Ultrasonic Transducer	Brand and Model Number
1	Olympus IMS – V1012
2	CeramTec-200Khz
3	CeramTec-400Khz
4	CeramTec-400khz-prototype
5	NU200E12TR-1
6	DYA-200-011-X

Table 3.1: List of Tested Transducers for the Feasibility Study

To test the transducers, the configuration shown in Figure 3.1 was used. Two transducers of the same kind were used in each testing experiment, and the input factors were the same while testing all six transducers. These inputs are: the supplied voltage to the emitter, and the distance between the transmitter and receiver. The experiments were conducted with air at room conditions as the medium.

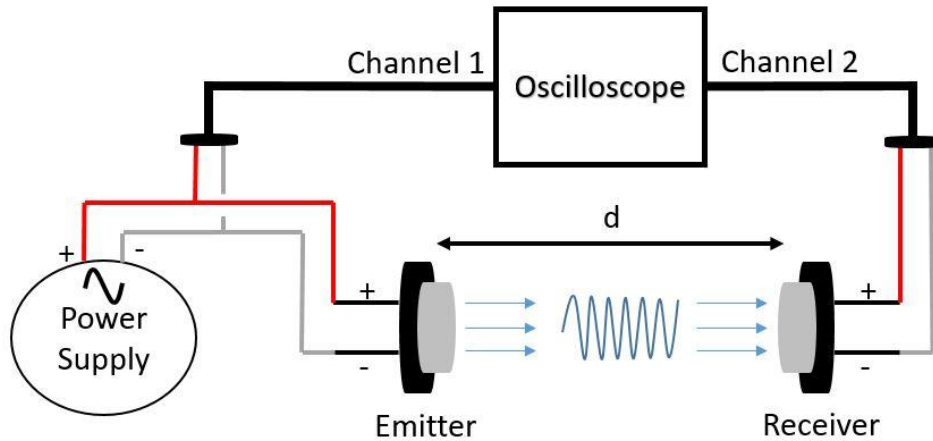


Figure 3.1: Ultrasonic Transducers Test Setup

The emitter is powered by a power supply with a pulse of a sinusoidal wave $V_{pp} = 20 \text{ V}$, and the distance d between the emitter and receiver was fixed at 10 cm among all experiments. On the oscilloscope, channel 1 was for the emitter and channel 2 was used for the receiver. The outputs of this transducers feasibility study are:

- Which transducers work in a gas medium
- Accuracy of the transducer (is there any time delay?)
- Signal to noise ratio
- How easy it is to measure the time t

The suitability of an ultrasonic transducer depends on the outcome of this initial study along with other specifications such as the maximum allowable input voltage, and the maximum operating pressure and temperature.

Figure 3.2 shows a schematic for the expected view on the oscilloscope screen. The time difference between the first peak on channel 1 and the first peak on channel 2 is directly related to the speed of sound.

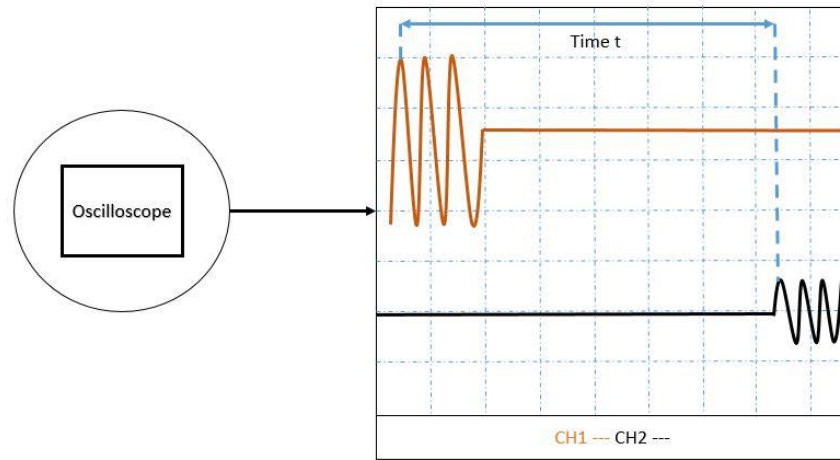


Figure 3.2: Expected Oscilloscope Screen with Emitter Signal on Channel 1 and Receiver Signal on Channel 2

The first transducer (Olympus IMS – V1012) was tested using the setup shown in Figure 3.1. No signal was detected on the second channel. The reasons behind this result were investigated to find out that this specific transducer is not designed to work in a gaseous medium. It was found that this transducer works best in solid materials flaw detection.

The second transducer was tested in the same setup. It was found that this transducer works in a gaseous medium. However, the signal to noise ratio was high, and the output voltage on the receiver transducer was low which makes the detection of the first peak very hard. In addition, the legs of the ultrasonic transducer were flimsy and can be easily broken. Figure 3.3 shows a screenshot of the oscilloscope window.

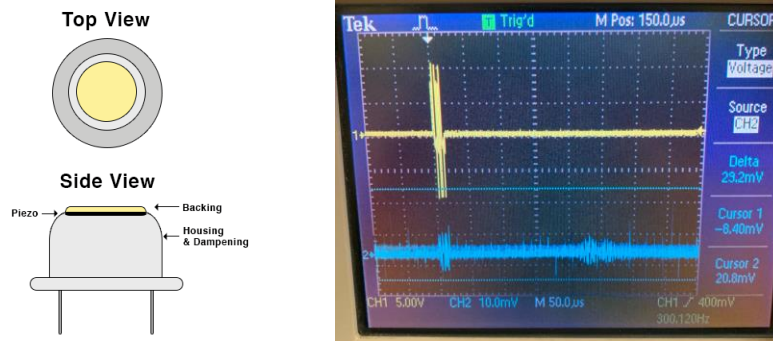


Figure 3.3: Ultrasonic Transducer 2 Testing Results

Next, the third transducer was tested. It was found that this transducer works with a gas medium. However, the signal was very weak, and the signal to noise ratio was high. The signal becomes weaker when the distance between the two transducers increases. At 10 cm distance, it was not possible to distinguish the noise from the signal on the receiver side. The two transducers were moved closer together, and at 0.7cm a screenshot of the oscilloscope was taken as shown in Figure 3.4.

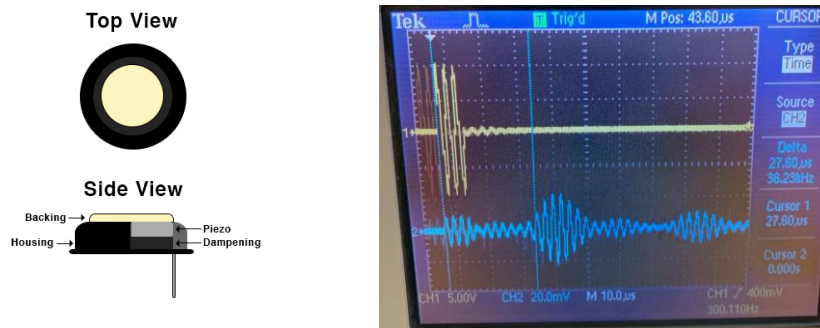


Figure 3.4: Ultrasonic Transducer 3 Testing Results

Transducer 4 was tested in the next step. The transducer was able to operate in a gaseous medium. However, it suffered from the same problems as transducers 2 and 3. The signal on the receiver side was very weak, and the signal to noise ratio was high. It was hard to identify the first peak of the receiver signal at large distances. The transducers were moved closer together and the obtained results are shown in Figure 3.5.

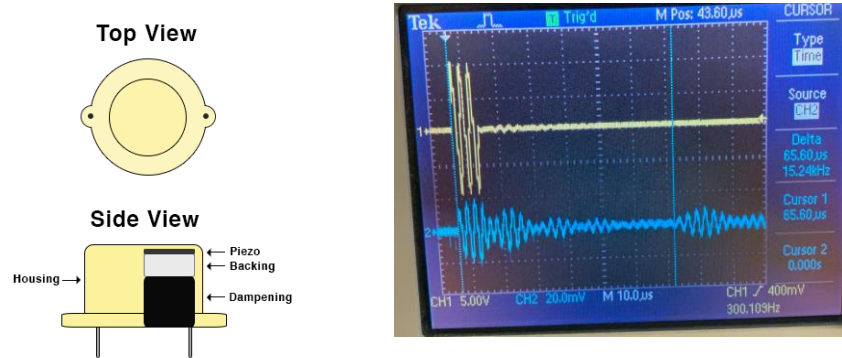


Figure 3.5: Ultrasonic Transducer 4 Testing Results

Testing transducer 5 was the next step. It showed a great improvement over the other transducers. The output signal on the receiver transducer was larger, and the signal to noise ratio was smaller. It was easy to distinguish the signal from noise and to detect the first peak on the receiver side. The only drawback of this transducer was its flimsy legs which made it very hard to connect to the power supply and oscilloscope. Transducer 6 showed a similar performance to transducer 5. However, the legs were much better. The output signal of the receiver was in the order of 100 mV. Figure 3.6 shows the testing results of transducer 6.

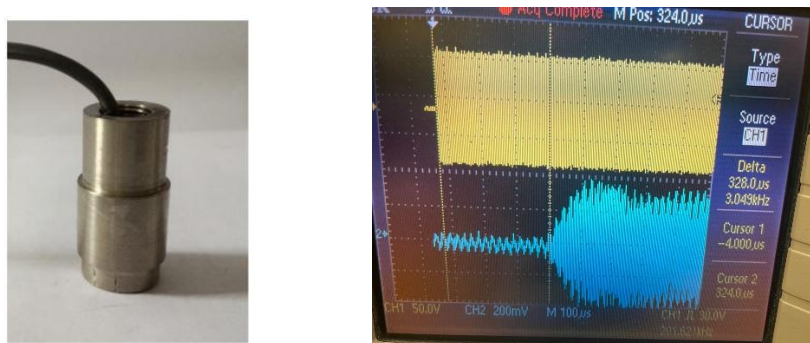


Figure 3.6: Ultrasonic Transducer 6 testing results

The operating temperature range (-40 to 80 °C) of transducer 6 makes it a good candidate for the application of gas detection. The maximum allowable peak to peak supply voltage

is 600V, and the maximum operating pressure is 1.6MPa. DYA-200-011-X was chosen to be used in the ultrasonic technique gas composition testing.

The materials and design of an ultrasonic transducer highly affects its performance in a certain medium. As discussed in section 2.1, the piezoelectric element, the matching layer, and the backing element specify the performance of the transducer. This explains why some transducers are better than the others in certain conditions.

3.3 Gas Composition Experimental Setup Design

In order to accurately test the ability of the ultrasonic transducer to detect the composition of a mixed gas. The first step was to design a jig that is capable of securing the ultrasonic transducers in place, and simultaneously connect to a gas supply with flanges. The dimensions of the ultrasonic transducers were taken into consideration to fit tightly inside the jig. Figure 3.7 shows the design of the jig.

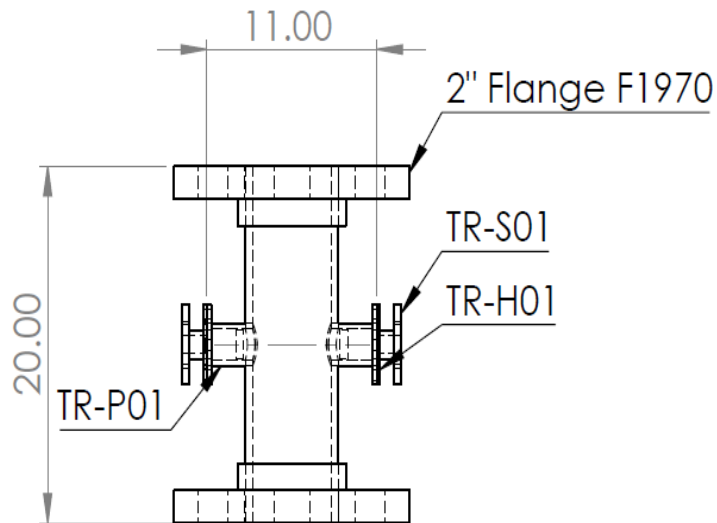


Figure 3.7: jig Design of Gas Composition Experiment

The flanges connect to a gas supply in order to fill the medium with a mixed gas. The two transducers sit in two small pipes with their facets maintained parallel to each other. The

material of the pipe was chosen to be CPVC, and the pipe diameter was 2". The distance between the two transducers was 6.9 cm making them as close as possible without interfering the gas flow inside the pipe. The jig was then manufactured, and the transducers were installed and tested.

Figure 3.8 shows a schematic of how the emitter and receiver are placed inside the pipe.

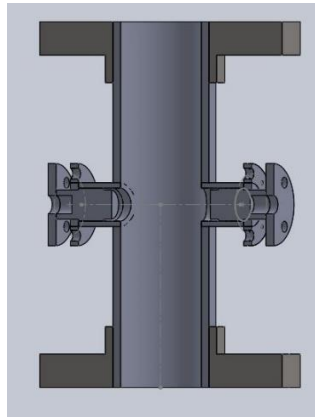


Figure 3.8: Section View of the Jig Design

In order to prove the principal of gas composition testing using ultrasonic transducers, a mixed gas shall be supplied to the medium between the two ultrasonic transducers. Ideally, the mixed gas shall be hydrogen blended natural gas. However, due to the explosive nature of mixed natural gas, especially in a laboratory closed room environment, an alternative lower risk mixed gas can be used in the proof of principle experiment. The alternative mixed gas was chosen to be a mixed nitrogen/oxygen gas. Both nitrogen and oxygen are present in air and their presence does not impose any risk on the person that is performing the experiment.

Pressurized nitrogen/oxygen mixed gas cylinders were ordered from Airliquide with different molar concentrations. Each cylinder's content was analyzed by the supplier to provide an accurate measurement of the composition of the pressurized mixed gas cylinders.

Table 3.2 shows the different mixed nitrogen/oxygen cylinders that were used in the composition testing experiment.

Cylinder	Molar% Oxygen	Molar% Nitrogen
1	25	75
2	33.3	66.6
3	50	50
4	75	25

Table 3.2: Cylinders Used in the Mixed Gas Composition Testing with their Relative Molar Concentrations of Nitrogen and Oxygen

Figure 3.9 shows the mechanical and electrical design assembly of the cylinders and jigs during the composition testing experiments.

In order to ensure that only the mixed gas is present between the two transducers, the jig would be flushed with the mixture before the experiment and the outlet of the jig would be slightly sealed in order to prevent backflow of air into the medium.

Using Ansys and MATLAB, the simulation/theoretical speed of sound are obtained. These simulation results were compared with the experimental results to check how accurate the speed of sound calculation and the proposed mixed gas composition testing could be.

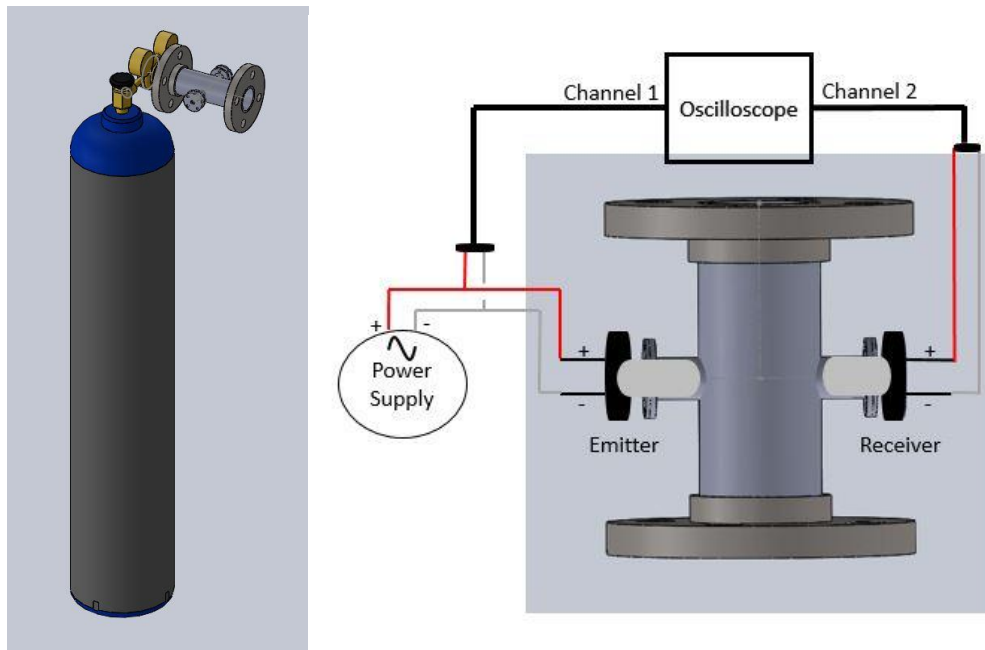


Figure 3.9: Cylinder Jig Assembly During the Composition Testing Experiment

3.4 Experimental and Simulation Results

The design was implemented in a lab setup as shown in Figure 3.10. A pressure regulator was installed between the cylinder and the jig to be able to control the flow out of the cylinder. A thermistor was used to measure the temperature of the gas near the ultrasonic transducers' location inside the pipe.



Figure 3.10: Implemented Mechanical Cylinder/Jig Assembly

In order to get the calorific measurement, the composition of the mixed gas shall be calculated. The proposed way to calculate the composition of the mixture depends on the accuracy of the speed of sound calculation. Since the composition of the gas cylinders are known and analyzed by Airliquide to a very high accuracy, an accurate reference for the experimental findings is present. Figure 3.11 shows a chart that explains the logical flow of the speed of sound comparison between the experimental and real theoretical results of speed of sound. Figure 3.12 shows a chart that explains how a second comparison can be made between the experimental composition results and the real ones reported by Airliquide.

Development of Advanced Technologies for Mixed Natural Gas Detection

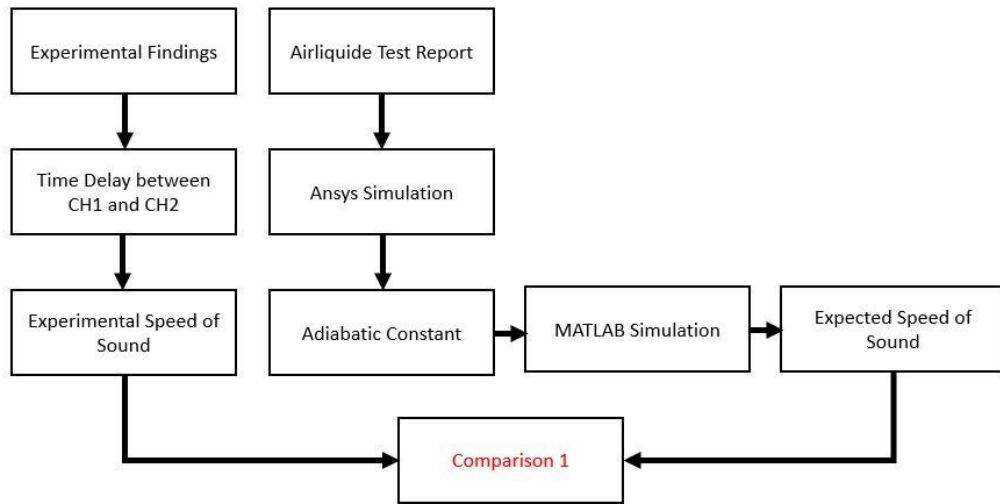


Figure 3.11: Speed of Sound Comparison Between the Experiment and Airliguide Report

In the first comparison, the time difference between channel 1 and channel 2 on the oscilloscope is used to calculate the speed of sound in the medium. On the other hand, the composition report is used to calculate the expected speed of sound. The experimental and expected speed of sounds are compared.

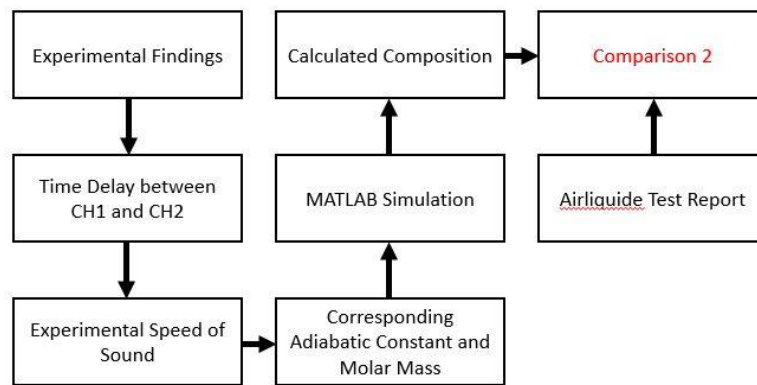


Figure 3.12: Gas Composition Comparison Between the Experiment and Airliguide Report

In the second comparison, the time delay is used to calculate the speed of sound. In addition, using MATLAB, the corresponding molar fraction of each component in the mixture is calculated. The experimental composition finding is compared with the Airliguide composition report.

Table 3.3 shows the obtained experimental time delays between channels 1 and 2 in Air, and in the 4 different gas mixtures.

Test Medium	Time Delay (micro seconds)
Air	201
Cylinder 1 (25 Molar% O ₂)	202.7
Cylinder 2 (33.3 Molar% O ₂)	203.9
Cylinder 3 (50 Molar% O ₂)	206.4
Cylinder 4 (75 Molar% O ₂)	210.1

Table 3.3: Time Delay Between Channel 1 and Channel 2 with Different Mediums

Figure 3.13 shows a plot for the time difference vs oxygen molar concentration in the mixed gas. The graph shows a good linearity.

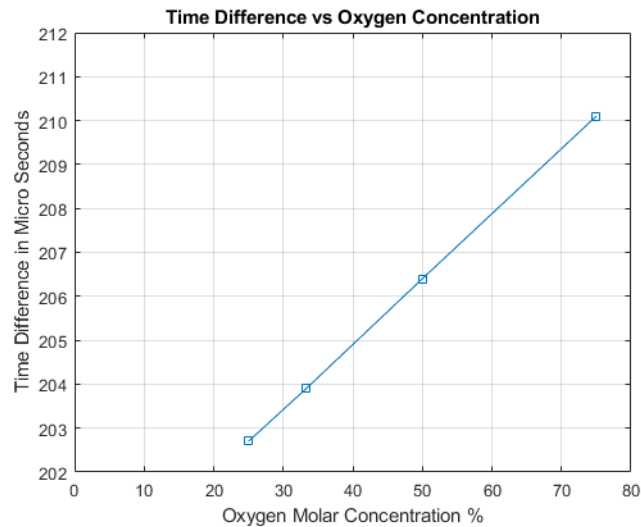


Figure 3.13: Experimental Time Difference vs Oxygen Molar Concentration

Using the procedure shown in Figure 3.11, the experimental speed of sound can be compared with the theoretical speed of sound as shown in Table 3.4.

Test	Temperature (°C)	Experimental Speed of Sound (m/s)	Expected Speed of Sound (m/s)	% Error
Air	20	343.28	343.2	0.023%
Cylinder 1	15	340.4	340.62	0.065%
Cylinder 2	15	338.4	338.62	0.065%
Cylinder 3	15	334.3	334.48	0.054%
Cylinder 4	15	328.42	328.59	0.052%

Table 3.4: Experimental vs Expected Speed of Sound Comparison

The experimental results show that the speed of sound calculation can be made with a very high accuracy with an error less than 0.1% when compared with the theoretical speed of sound. Figure 3.14 shows the plots for the experimental and theoretical speed of sounds constructed using the 4 mixed gas data points in this experiment.

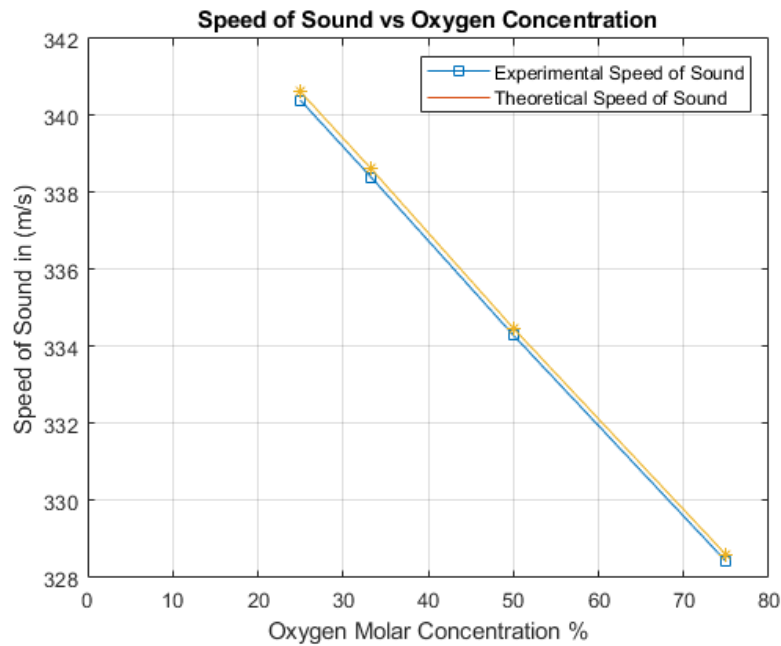


Figure 3.14: Experimental and Theoretical Speed of Sound Calculations vs Oxygen Molar Concentration

By comparing the speed of sound measurements, it can be concluded that the proposed method is capable of determining the composition of the mixture under certain conditions:

- The gases that are present in the mixture are known

- The temperature measurement is accurate
- The time delay measurement is accurate

If one of these conditions is not accurate, the composition measurement would deviate from the real values.

After making sure that the speed of sound measurement is highly accurate, comparison 2 was then conducted. Table 3.5 shows the findings of comparison 2.

Airliquide Reported Composition	Experimental Composition
Molar %: 25 O ₂ / 75 N ₂	Molar %: 25.9 O ₂ / 74.1 N ₂
Molar %: 33.33 O ₂ / 66.66 N ₂	Molar %: 33.91 O ₂ / 66.09 N ₂
Molar %: 50 O ₂ / 50 N ₂	Molar %: 50.7 O ₂ / 49.3 N ₂
Molar %: 75 O ₂ / 25 N ₂	Molar %: 75.7 O ₂ / 24.3 N ₂

Table 3.5: Comparison Between Composition Measurement Using Ultrasonic Transducers and Airliquide Reported Composition

The molar composition of the mixed nitrogen-oxygen cylinders was calculated with a very high accuracy compared with the reported Airliquide concentrations. The volumetric concentration can also be compared by converting the molar concentration to a volumetric one. Both gases are present at the same pressure and temperature, so according to Avogadro's law, the molar fraction is the same as the volumetric fraction.

The proposed composition measurement technique was able to detect the volumetric composition of a mixed nitrogen-oxygen gas with a deviation less than 1%. However, the end goal was to see how accurate the composition of methane-hydrogen mixture can be. To investigate this, the effect of adding hydrogen to methane shall be compared with the effect of adding nitrogen to oxygen.

- Speed of Sound in hydrogen is much higher than speed of sound in Nitrogen
- Adding a small amount of hydrogen to methane would drastically affect the speed of sound of the mixture

- Adding a small amount of hydrogen to methane is equivalent to adding a huge amount of nitrogen to oxygen when looked at from a speed of sound point of view

To visualize these effects more, the rate of change in speed of sound vs hydrogen content in a methane-hydrogen mixture shall be compared with the rate of change in speed of sound vs nitrogen content in a nitrogen-oxygen mixture. Figure 3.15 shows two graphs that explain how much the addition of hydrogen or nitrogen affects the speed of sound in their corresponding mixtures.

Adding nitrogen such that it corresponds for 20% of the volume in a nitrogen oxygen mixture, would change the speed of sound from 323 m/s (pure oxygen at 15 °C) to 327.44 m/s. However, adding hydrogen to methane to have a 2% H_2 -98% CH_4 mixture would change the speed of sound from 440.3 m/s (pure methane at 15°C) to 446.23 m/s. As a result, methane-hydrogen mixtures are 10 times more sensitive to the change in composition. The slopes of the two graphs shown in Figure 3.15 are 2.78 and $0.2248 \frac{\text{m}}{\text{s}} \frac{1}{\%V}$.

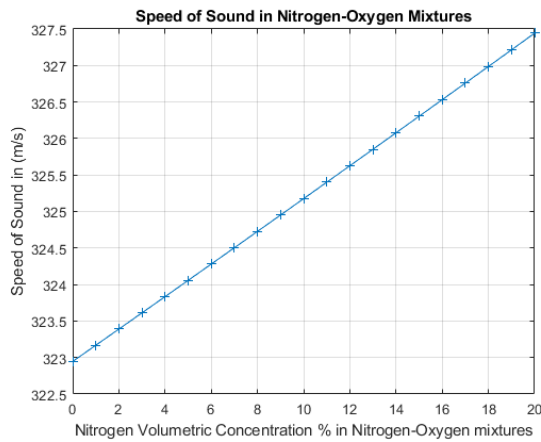
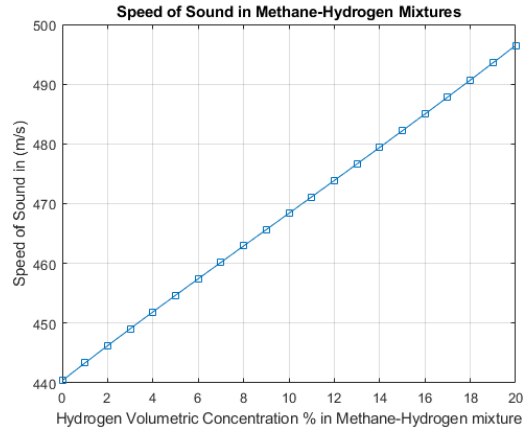


Figure 3.15: Speed of Sound in Methane-Hydrogen and Nitrogen-Oxygen Mixtures

Figure 3.16 shows both plots in the same figure to better see the difference in slopes.

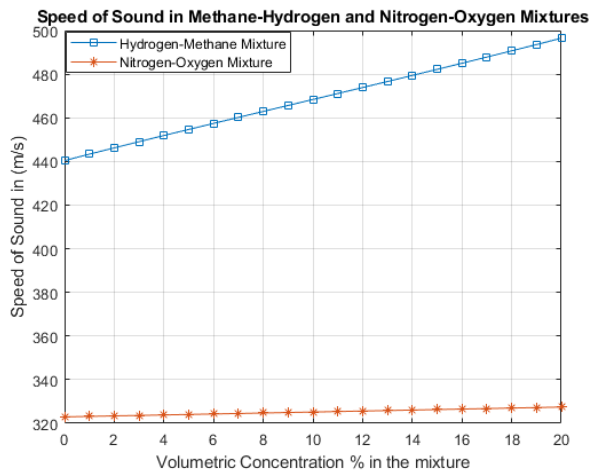


Figure 3.16: Speed of Sound in Methane-Hydrogen and Nitrogen-Oxygen Mixtures

The maximum % error in the nitrogen-oxygen speed of sound measurement was 0.065%. If the same error is assumed in the Methane-Hydrogen simulation, the conducted experiment would be able to detect the addition of a very small amount of hydrogen (<0.5%) with a maximum deviation of 0.1% from the real hydrogen or methane composition.

The calorific value for hydrogen is between 10.05MJ/m³ and 11.88MJ/m³, and the calorific value of natural gas is between 35.22MJ/m³ and 39.05MJ/m³ [95]. Assume a total volume of hydrogen blended natural gas V_{total} . The ratio of hydrogen to the total volume is x_1 and the ratio of natural gas to the total volume is defined as x_2 . The total calorific value can be obtained using Equation (3.1)

$$C_{Va} = C_{Va \text{ of } H_2} * x_1 + C_{Va \text{ of } Ng} * x_2 \quad (3.1)$$

The average calorific values of hydrogen and natural gases are 10.965 MJ/m³ and 37.135 MJ/m³. The total calorific value becomes as shown in Equation (3.2).

$$C_{Va} = 10.965 * x_1 + 37.135 * x_2 \quad (3.2)$$

As per the experimental and simulation work, the expected uncertainty in x_1 or x_2 is less than 0.1.

$\Delta x_1 = \pm 0.1\%$ and $\Delta x_2 = \pm 0.1\%$ with these two uncertainties, the uncertainty in the total calorific value can be obtained as shown in Equation (3.3)

$$\begin{aligned} \Delta f &= \sqrt{\left(\frac{\delta f}{\delta x_1} \Delta x_1\right)^2 + \left(\frac{\delta f}{\delta x_2} \Delta x_2\right)^2} \quad (3.3) \\ &= \sqrt{(10.965 * 0.001)^2 + (37.135 * 0.001)^2} \\ &= 0.03872 \text{ MJ/m}^3 \end{aligned}$$

Where f is the calorific value function shown in Equation (3.2).

If the calorific measurement is used to bill the supplied mixed gas, the total energy supplied shall be known, which requires a precise total volume measurement. Flow meters can be used to measure the total flow volume. We define the price of hydrogen per unit energy as

P_{H_2} and the price of natural gas per unit energy as P_{Ng} , and P_t as the total price per unit energy. The billing amount can be calculated as shown in Equation (3.4)

$$P = C_{Va} * V_{total} * P_t = C_{Va \text{ of } H_2} * x_1 * V_{total} * P_{H_2} + C_{Va \text{ of } Ng} * x_2 * V_{total} * P_{Ng} \quad (3.4)$$

The total price per unit energy may be a function of the composition of the mixed gas to account for the higher price of hydrogen.

The uncertainty in price can be expressed as shown in Equation (3.5)

$$\begin{aligned} \Delta P &= \sqrt{\left(\frac{\delta P}{\delta C_{Va}} \Delta C_{Va}\right)^2 + \left(\frac{\delta P}{\delta V_{total}} \Delta V_{total}\right)^2} \quad (3.5) \\ &= \sqrt{(3.872 * V_{total} * P_t)^2 + (C_{Va} * P_t * \Delta V_{total})^2} \end{aligned}$$

It can be concluded from Equation (3.5) that the accuracy of pricing depends on the accuracy of the calorific value measurement, and the uncertainty of the volumetric flow rate measurement.

In Canada, the price of natural is 0.034 U.S. dollar per KWh which is 0.01 U.S. dollar per Megajoule (MJ) [96]. On the other hand, in 2020, a company based in Quebec called V energies sold green H_2 for 2.67 U.S. Dollar per kg [97]. This makes the price per (MJ) of hydrogen 0.0204 U.S. Dollar per MJ.

We take a special case of 10% blended hydrogen and natural gas, and we calculate the price of the mixed gas to be 0.01104 U.S. Dollar per MJ. At 10% blending, the expected calorific value is 34.518 MJ/m³.

Using Equation (3.5), the expected uncertainty in pricing becomes as shown in Equation (3.6)

$$\begin{aligned} \Delta P &= \sqrt{(0.03872 * V_{total} * 0.01104)^2 + (34.518 * 0.01104 * \Delta V_{total})^2} \quad (3.6) \\ &= \sqrt{0.000000183 * V_{total}^2 + 0.1452 * \Delta V_{total}^2} \end{aligned}$$

The price P can be written as shown in Equation (3.7)

$$P = 34.518 * 0.01104 * V_{total} \quad (3.7)$$

$$= 0.381 * V_{total}$$

Assuming that the uncertainty of the flow measurement is negligible, the uncertainty in pricing can be studied based on the findings of the ultrasonic composition experiment. In 2021, the annual residential natural gas usage in Canada was between 1900 and 3100 m³ [98]. Assuming the upper limit is going to be the same with mixed natural gas, the price and the uncertainty can be plotted as shown in Figures 3.17 and 3.18.

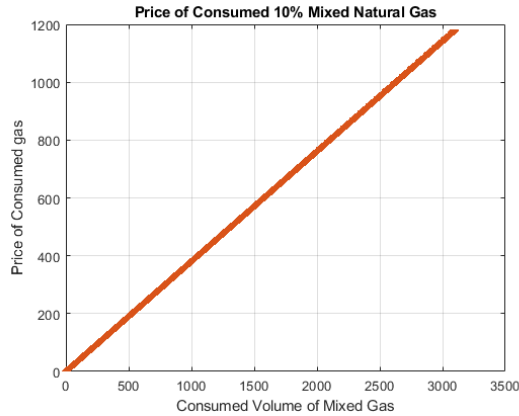


Figure 3.17: Price of Mixed gas vs Consumption

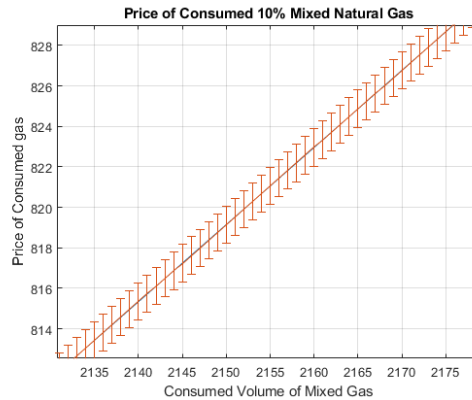


Figure 3.18: Error bars in Price due to Ultrasonic Transducer Composition Testing Uncertainty

From Figure 3.18 and Equation (3.6), it can be seen that the uncertainty is linearly proportional to the price of consumed gas. The percentage error can be written as:

$$\%Error = \frac{\Delta P}{P} * 100 = 0.1122\%$$

It can be concluded that the uncertainty in the proposed ultrasonic composition testing slightly affects the accuracy of the billing price. In addition, the proposed method is expected to perform better in mixed natural gas than in nitrogen-oxygen mixtures.

As mentioned in Section 1.2.3, some countries limit the billing error in gas supply to 2%. Out of this 2% error, 0.1122% is due to the uncertainty in mixed gas composition testing. A superposition method can be used to determine the allowed error in volume measurement ΔV_{total} in order to comply with the 2% requirement. It turns out that the allowed error in volume measurement shall not exceed 1.997% in order to obtain the 2% error margin in billing. In conclusion, the proposed ultrasonic composition testing method shows a promising solution for determining the mixing ratios in hydrogen blended mixed gas. However, it is important to avoid major source of errors in volumetric flow rate measurements.

3.4.1 Composition and Flow Rate Measurement

In the second experiment, a flow meter supplied by Romet Limited was used after the ultrasonic jig to measure the flow rate. The flow meter was equipped with a temperature sensor. The experimental setup is shown in Figure 3.19.

The purpose of this experiment is to prove that the flow rate and composition testing can be done simultaneously, and to find out what are the requirements for an accurate combined measurement.

The same experimental procedure that was explained in section 3.4 was used in this experiment. Table 3.6 shows the outcome of the experiment with 50% Oxygen and Air.



Figure 3.19: Experimental Setup of Composition and Flow Rate Measurements

Test	Flow Rate (CF/hr)	Temperature (°C)	Experimental Speed of Sound (m/s)	Theoretical Speed of Sound (m/s)	Error %
50% Oxygen	203	19	334.33	336.78	0.73%
50% Oxygen	244	19	334.33	336.78	0.73%
Air	240	22.3	344.48	344.68	0.058%

Table 3.6: Obtained Experimental Results for Composition and Flow Measurements

The obtained results in this experiment show a higher error in composition testing which can be explained by the following factors:

- The outlet of the flow meter is not sealed which is allowing for air mixing and leaking
- The temperature measurement is not close to the transducers position which induces some errors in the measurement
- The accuracy of the time delay measurement on the oscilloscope

In conclusion, it can be noted that the measurements shall be improved by incorporating the temperature sensor closer to the ultrasonic transducers' location, and by making sure that the medium between the two transducers is completely filled with the mixed gas. Since a compressed gas cylinder is used in this experiment, the temperature gradient is large throughout the stream which explains the difference in temperature between the first experiment and the second one. The speed of sound measurement for 50% oxygen was consistent with the previous result, which is another indication that the temperature measurement is a critical factor to determine the accuracy of the test.

3.4.2 Flow Rate Measurement Using Ultrasonic Transducers

The option of using ultrasonic transducers for flow rate measurements was studied. The physics behind the transit time method that was studied is described in section 2.2. The first step in this experiment was to design a jig that is capable of holding the two transducers at 45° with respect to the gas flow. The jig 3D design that was done on SOLIDWORKS is shown in Figure 3.20. The pipe was made out of CPVC with a 2" diameter.

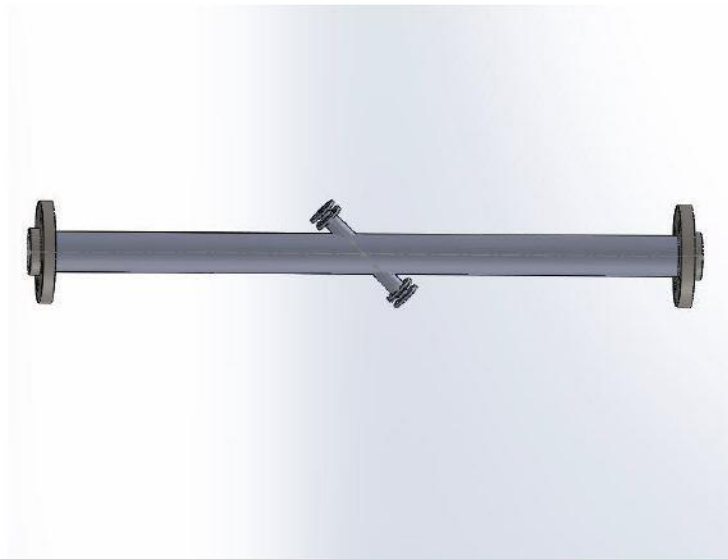


Figure 3.20: Ultrasonic Flow Meter Jig Design

The testing procedure requires two different time delay measurements. The first one is called the upstream ultrasonic time delay (with stream), and the second one is called the downstream ultrasonic time delay (against the stream). These two measurements are used to determine the velocity of the gas stream as explained in section 2.2. The ultrasonic transducers jig shall be connected to a gas supply with a known flow rate. The calculated flow rate from the ultrasonic technique should be compared with the reference flow rate. The test was conducted at Romet Limited facility in Mississauga, Canada. The experimental flow rate measurements were also compared with the simulation results. The simulation was done using Ansys where the velocity profile of the gas flow is obtained from which the ultrasonic time delay can be calculated. The logical flow of the comparison between the simulation, real, and experimental results is shown in Figure 3.21.

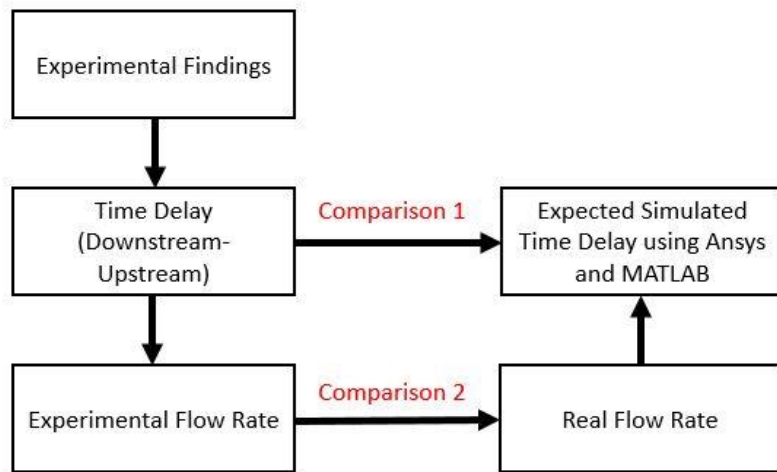


Figure 3.21: Comparison Methods Between Experimental, Simulation and Real Results

In the first comparison, the experimental and simulation time delays are compared to check how much the delay measurements are deviating from the expected simulated values. In the second comparison, the flow rates obtained from the ultrasonic transit time method are compared with the real flow rates obtained from a Romet flow meter.

Table 3.7 shows the obtained Time delays (downstream time-upstream time) with different flow rates.

Real Flow Rate (m ³ /hr)	Time against the flow (μ s)	Time with the flow (μ s)	Experimental time difference (μ s)
6.458	367	366.4	0.6
12.886	367.3	366.1	1.2
29.822	368.5	365.3	3.2
38.658	369.1	364.7	4.4
51.686	369.6	364.1	5.5
65.987	371.1	363.5	7.6
77.457	372.4	363.1	9.3

Table 3.7: Experimental Time Delays obtained with Different Air flow Rates

In Figure 3.22, a plot for the change in experimental time difference against the real flow rate is shown.

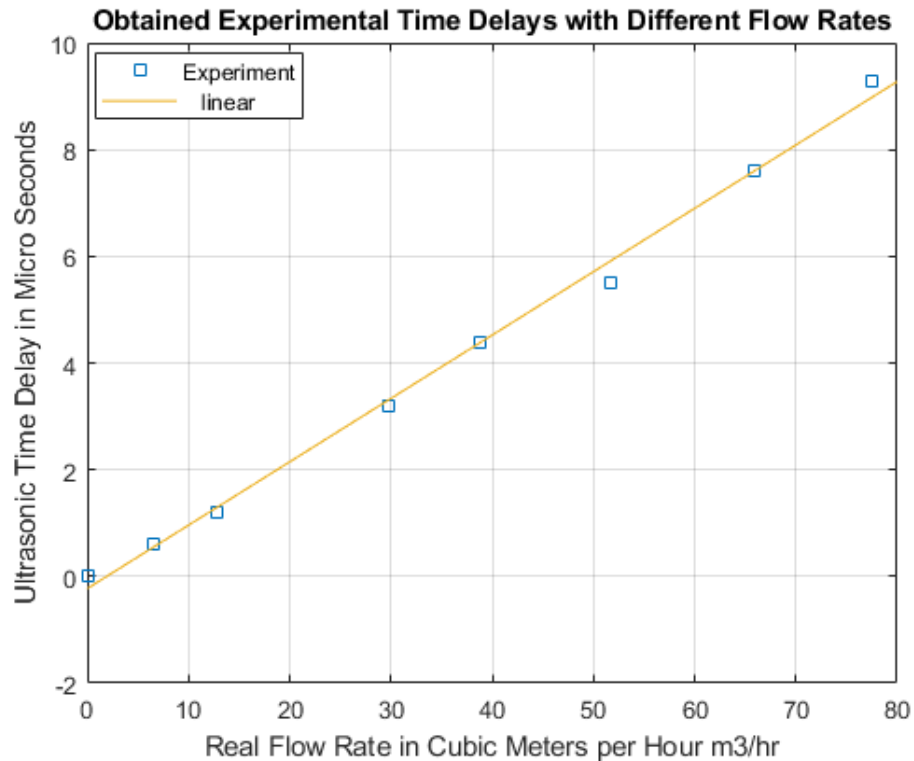


Figure 3.22: Ultrasonic Time Delay Measurements vs Different Flow Rates

The obtained time delays can be compared with the simulated time delays. The first step that is needed is to plot the velocity profile in Ansys and export the data to MATLAB to get the simulation time delays. Figure 3.23 shows a velocity contour obtained in Ansys. This step is needed because of the shape of the pipe and the way the ultrasonic are mounted.

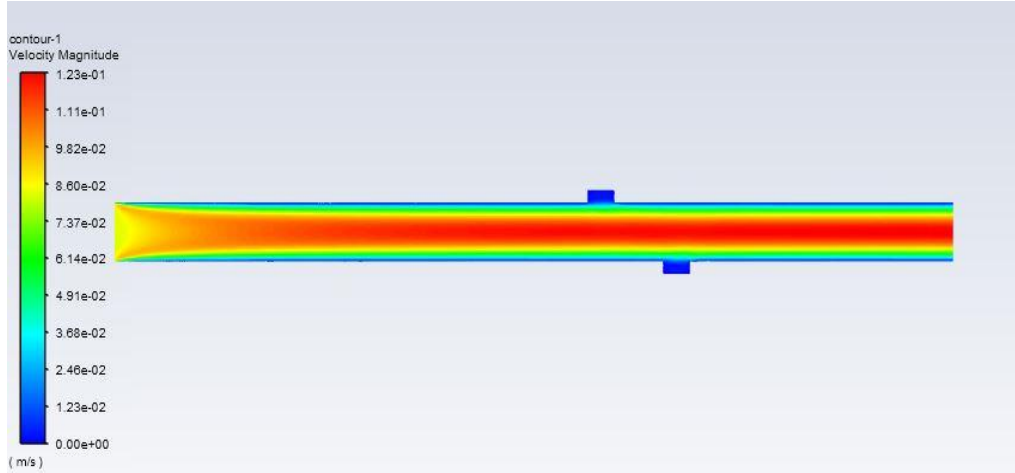


Figure 3.23: Velocity Contour for the Flow Inside the Pipe

In Figure 3.24, both experimental and simulation time delays are shown on the same plot.

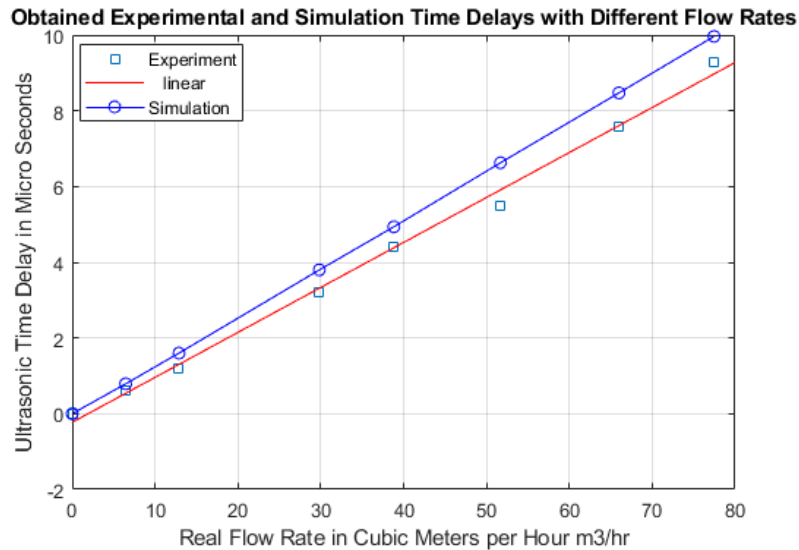


Figure 3.24: Experimental and Simulation Time Delay Measurements with Different Flow Rates

The maximum error between the simulation and experimental time delay is around 25% which occurred at low flow rates. By increasing the flow rate, the % error got smaller and

reached 5.83% with the last measurement. On the other side, the linearity in the experimental measurements is clear, which is a good sign that the measurements can be easily calibrated to have a perfect fit. Most ultrasonic transducer flow meters require a calibration step in order to get accurate flow rate measurements. The sources of errors in this experiment are:

- Air leaking in the connection between the jig and the air pump
- Signal to noise ratio in the ultrasonic signal due to the noisy and vibrational environment the test was conducted in
- Fluctuating flow rates from the air pump

The second comparison that can be made is to compare the obtained experimental flow rates with the ones obtained from Romet's rotary meter as shown in Table 3.8.

Test #	Ultrasonic Flow Rate (m³/hr)	Rotary Meter Real Flow Rate (m³/hr)	% Error
1	4.653	6.458	27.91%
2	9.306	12.886	27.79%
3	24.814	29.822	16.81%
4	34.118	38.658	11.76
5	42.645	51.686	17.5%
6	58.92	65.987	10.72%
7	72.09	77.457	6.94%

Table 3.8: Measured Flow Rates with the Time Transit Ultrasonic Method and the Rotary Meter

The results show that there are some errors in the ultrasonic flow rate measurements, and the method is always predicting a flow rate smaller than that of the rotary meter which might agree with the assumption of having some air leaking between the rotary meter and the ultrasonic meter. However, by plotting these two obtained flow rates, as shown in Figure 3.25, it can be seen that the ultrasonic flow rates can be calibrated in case no real leakage is happening. Most ultrasonic flow rate devices require calibration, and it is always

advised to calibrate these sensors in the location of installation before relying on their measurements.

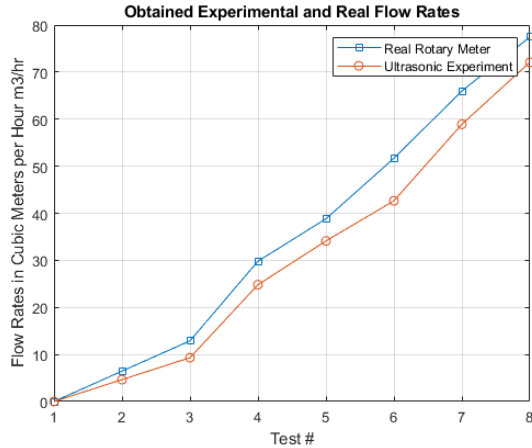


Figure 3.25: Experimental Ultrasonic and Real Rotary Flow Rate Measurements

The calibration can be done with a simple linear calibration function. An example of a calibration function that works with the current data is shown in Equation (3.8).

$$\text{Calibrated Flow Rates} = 1.09 * \text{Ultrasonic Flow Rate} + 1.6 \quad (3.8)$$

The 3 different plots can be put on the same graph to show how the calibrated curve becomes closer to the real rotary meter plot as shown in Figure 3.26.

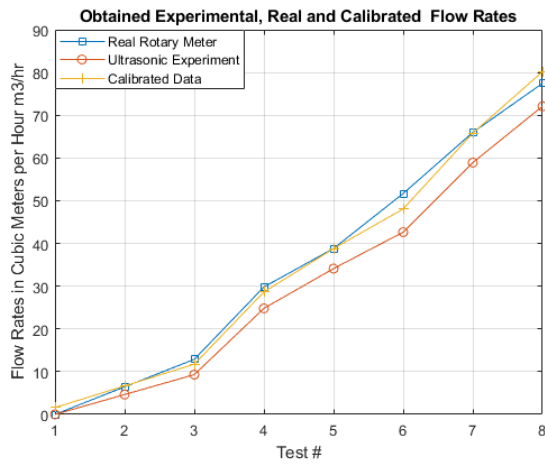


Figure 3.26: Experimental Ultrasonic, Real Rotary and calibrated Flow Rate Measurements

As a result, when the ultrasonic flow rate measurements are calibrated, they match with the real flow very well.

3.5 Conclusion and Future Work

Three different experiments were done in this project. The first experiment was the composition testing of mixed gas. The experiment was done with mixed oxygen-nitrogen to study the feasibility of the method to detect the composition of the components in the mixture. The method showed a very high accuracy in detecting the component's volumetric concentrations. It was also proven that the expected results for methane-hydrogen mixtures could be done with a higher accuracy. The second experiment was also a composition testing experiment, but with a flow rate measurement being conducted at the same time. The results also showed good agreement with the simulation and theory. It was concluded that the temperature measurement is a crucial factor that affects the accuracy of the measurements. In the third experiment, a time transit method was used to determine the flow rates of air. When calibrated, the results showed a good agreement with the real flow rates obtained from a calibrated rotary meter.

One obvious source of errors in the experiments was the way the ultrasonic time difference is obtained on the oscilloscope. A timing circuit can solve this issue where the time between the pulse of the first transducer is compared with the time of the generated pulse on the receiver side.

Some of the future potential tracks that can lead to a higher accuracy are:

- Design a circuit that is capable of detecting the time delay
- Amplify the signal on the receiver side
- Cancel the noise on the receiver transducer by using a band pass frequency circuit
- Consider battery powering of the emitter transducer for the method to be feasible to use in the field
- Test Mixed Natural gas compositions to confirm the accuracy

Development of Advanced Technologies for Mixed Natural Gas Detection

- Combine ultrasonic flow rate and composition measurement by designing a jig that is capable of holding 4 transducers
- Design and fabricate an ultrasonic transducer that perfectly matches the requirements for mixed natural gas detection

Chapter 4

4 Mid Wavelength Infrared Laser Source for Natural Mixed Gas Leak Detection

4.1 Introduction

Mixed natural gas tends to be one of the potential future fuels due to the increased interest in lowering the greenhouse gases emissions. As explained in section 1.2, hydrogen blending into natural gas would decrease the greenhouse emissions. However, the main constituent of a mixed natural gas is still methane, which is considered one of the most harmful greenhouse gases. As a result, leak detection of mixed natural gas is an important aspect in controlling the greenhouse gases emissions due to some safety concerns that are discussed in Section 1.1.4. Laser spectroscopy has been identified as one of the most successful techniques in gas leak detections as discussed in Section 2.4.5. Laser spectroscopy is based on the concept that some gases absorb an emitted laser beam if its wavelength matches the absorption line of the gas. A simple setup of direct laser spectroscopy is shown in Figure 4.1.

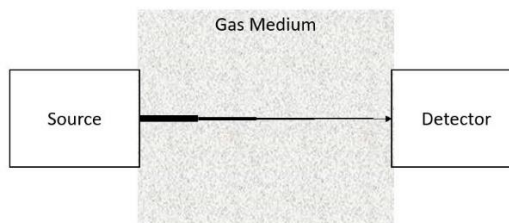


Figure 4.1: Direct Laser Absorption Spectroscopy

Two of the requirements for direct absorption gas spectroscopy are:

- An efficient high intensity laser source with good beam quality and wavelength that matches the absorption line of the gas medium
- A highly sensitive detector

The emitted laser intensity gets absorbed as it passes through the gas medium. The intensity decays exponentially with respect of the optical path to reach the detector with a much lower intensity than the emitted beam. This decay in intensity signals the presence of a gas having an absorption line at the laser wavelength. Methane has a weak absorption line in the short wave infrared (SWIR) region, and two strong absorption lines in the mid wave infrared red (MWIR) and long wave infrared (LWIR) regions. To take advantage of the strong absorption lines in the MWIR and LWIR regions, sources that emit in these region must be developed further. In this chapter, a high efficient mid-infrared laser for methane detection using a compact intracavity difference frequency generation (DFG) is reported.

4.2 Experimental Setup and Procedure

In this work, an intracavity structure is used with Nd:YVO₄ as the fundamental crystal. Nd:YVO₄ is capable of producing a 1064 nm beam that serves as the pump for the nonlinear DFG process. The gain medium is pumped with an 808 nm fiber pigtailed laser. The intracavity structure contains a 5 mol% MgO doped periodically-poled lithium niobate (PPLN) as the nonlinear crystal. The signal source is an amplified tunable C-band laser. To couple the signal and pump in the PPLN, a dichroic mirror is inserted inside the resonator cavity that reflects the signal beam towards the PPLN. A schematic for the full setup is shown in Figure 4.2.

The multimode 808nm fiber pigtailed diode laser has a 125 μm core diameter. A 4.5 W 808 nm optical power was focused onto the Nd:YVO₄ using an anti-reflection (AR) coated at 810 nm GRIN lens. The Nd:YVO₄ is high-reflective (HR) coated at 1064 nm ($R > 99.9\%$) and high-transmission (HT) coated at 808 nm ($T > 95\%$) at the input facet. At the output facet, the Nd:YVO₄ is AR coated at 1064 nm ($T > 99.8\%$). The dimensions of the Nd:YVO₄ are 3mm (W) x 3mm (H) x 8mm (L), and the doping concentration is 0.5%. Moreover, the

dichroic mirror has a 99.3% transmission at 1064 nm and 70% reflectivity at 1528 nm at 45° angle. The PPLN is AR coated for 1064 nm and 1528 nm ($T > 99.8\%$) at the input facet, and AR coated for 1064 nm ($T > 99.8\%$) and $3.5 \mu\text{m}$ ($T > 95\%$) at the output facet. The PPLN has a period of $30.3 \mu\text{m}$ and the dimensions of the crystal are 3mm (W) x 3mm (H) x 50mm (L). The output coupling (OC) mirror is plano-concave with a 100 mm radius of curvature. The input facet of the OC is HR coated at 1064 nm ($R = 99.85\%$) and AR coated for $3.5 \mu\text{m}$ ($T = 92\%$). The total cavity length is less than 90 mm. A germanium (Ge) filter is used to filter out the pump and signal after the OC, and a thermal power sensor is used to measure the generated MWIR DFG power. In addition, the signal source is an amplified C-band tunable laser. The amplification is done using a polarization maintained (PM) erbium-doped fiber amplifier (EDFA). The signal beam is focused in the middle of the PPLN by using a 5x beam expander and a focusing lens with a 100 mm focal length. The fibers used to connect the tunable laser, EDFA and beam expander are PM fibers.

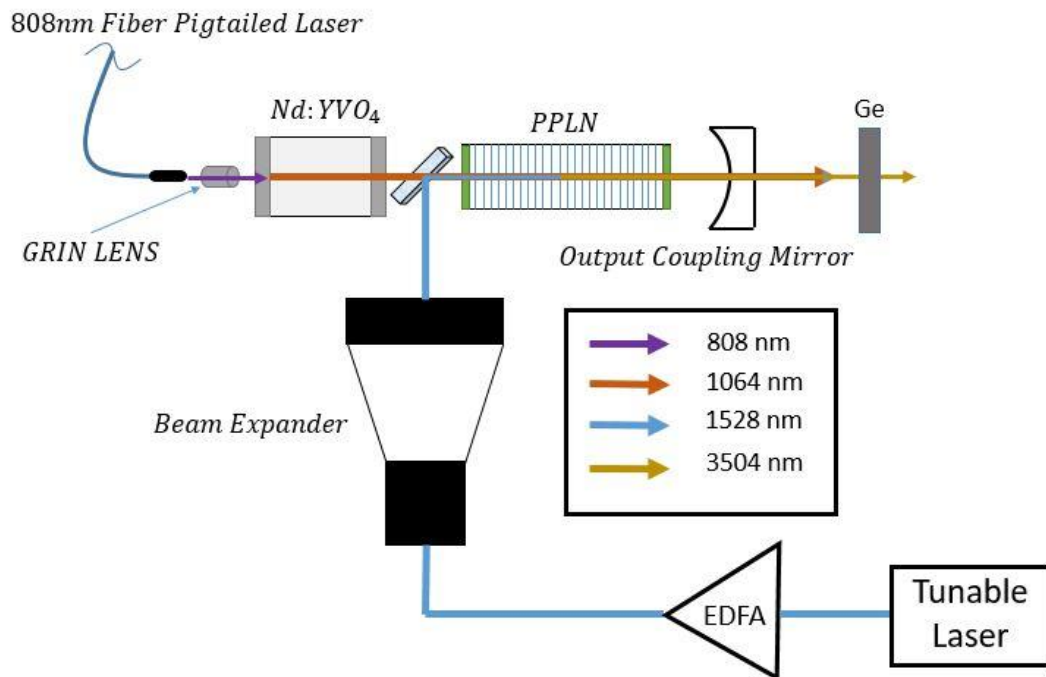


Figure 4.2: Schematic Diagram of the MWIR DFG Laser

In order to control the temperature of the fiber pigtailed laser, Nd:YVO₄, and PPLN, the components were mounted on copper jigs, thermo-electric Peltiers, heat sinks, and fans as shown in Figure 4.3.

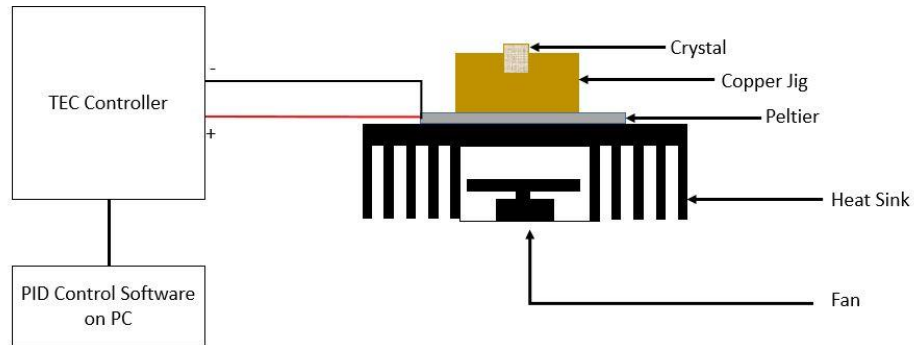


Figure 4.3: Schematic of the Thermal Control Setup

The thermal management system is a crucial part of the overall setup in order to operate the components that are sensitive to any temperature change.

- The temperature of the 808 nm fiber pigtailed laser shall be controlled in order to ensure that the output wavelength is set at 808 nm.
- The temperature of the Nd:YVO₄ shall be stabilized in order to achieve a stable output power and to avoid any potential thermal induced damage
- The temperature of the PPLN shall be fixed at the QPM temperature in order to achieve a highly efficient nonlinear conversion.

4.2.1 Experimental Procedure

A detailed experimental procedure is explained in this section. All components shall be carefully aligned and tested in order to ensure everything is operating as per the design requirements.

The following points are addressed in the test preparation:

- 808 nm power vs supplied current is measured in order to obtain the operating current
- Output wavelength vs temperature to obtain the operating temperature
- Use a 5 axis stage to Align the 808 nm with the alignment beam
- Use a 5 axis stage to insert and align the GRIN lens in front of the 808 nm laser
- Use a 5 axis stage for the Nd:YVO₄ gain medium
- Roughly align the Nd:YVO₄ using the alignment beam
- Insert the output coupling mirror in a jig and use a 5 axis stage to roughly align the OC
- Turn on the current source and slowly increase the current while making sure that the temperature controller is capable of keeping the temperature at the desired points
- Fine tune the optical components to maximize and record the 1064 nm leaking power
- Insert the PPLN inside the resonator cavity using a 5 axis stage, align it using the alignment beam, and optimize the alignment while maximizing the 1064 nm leaking power
- Obtain the QPM temperature by doing a spontaneous parametric down conversion (SPDC) experiment
- Ensure that the temperature is stable at the QPM temperature
- Insert the dichroic mirror at 45° using a rotational stage, and maximize the 1064 nm leaking power
- Use the obtained experimental powers to confirm the reflectivity and transmissions of the different optical components at the 1064 nm.
- Insert a second OC outside the resonator cavity to confirm its transmission at 1064 nm
- Double check the dichroic mirror transmission at 1064 nm by using another one outside the resonator cavity

- Use a scanning slit beam profiler outside the cavity to measure the beam width and calculate the expected beam waist of the Gaussian beam inside the resonator cavity
- Mount the beam expander on a 6 axis stage
- Use the beam profiler to measure the minimum achievable beam waist of 1528 nm
- Confirm the dichroic mirror reflectivity at 1528 nm
- Check polarization of 1528 nm and 1064 nm to ensure it is parallel to the z-axis of the PPLN
- Use the beam profiler to confirm that the 1528 nm beam and 1064 nm beam are overlapping outside the cavity at different positions
- Use a germanium (Ge) filter outside the cavity to cut out 1064 nm and 1528 nm and pass the MWIR generated output
- Fine tune the beam expander position and angle to maximize coupling and DFG power

From the components testing, a total intracavity loss can be obtained, and it can be used in simulations to have a meaningful representation for the specific setup on hand. The obtained intracavity components specifications that were found match with the reported ones in section 4.2. The operating temperature of the fiber pigtailed laser was found to be 31°C. In addition, the TEC was able to stabilize the Nd:YVO₄ temperature at 30°C. The PPLN QPM temperature was found to be 23°C using the spontaneous parametric down conversion (SPDC) test.

4.2.2 Spontaneous Parametric Down Conversion (SPDC) Test

The SPDC signal test is conducted to ensure that the QPM temperature of the PPLN. Figure 4.4 shows the setup of the SPDC experiment.

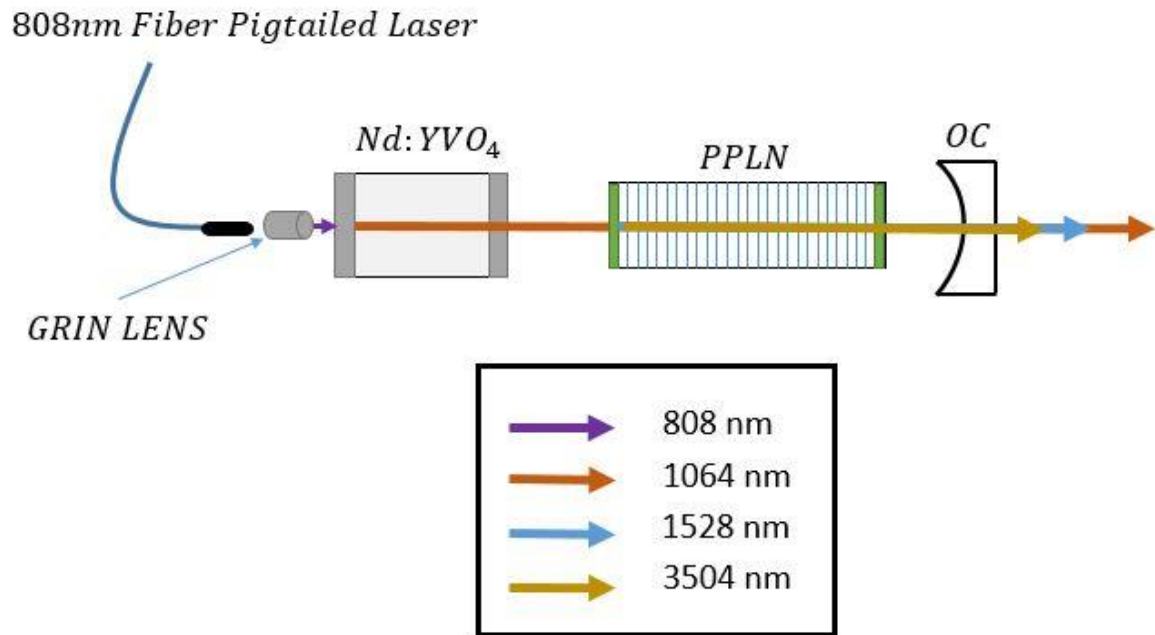


Figure 4.4: SPDC Test Setup

By pumping the PPLN with 1064 nm, we expect a weak SPDC signal at 1528 if operating at the QPM temperature. Using an optical spectrum analyzer (OSA), the SPDC signal can be observed. To confirm that the shown signal on the OSA is a SPDC signal, the temperature of the PPLN shall be changed and the wavelength of the SPDC signal is monitored on the OSA as it should also shift. Figure 4.5 shows a sample picture of the SPDC signal obtained in the experiment at 25°C.

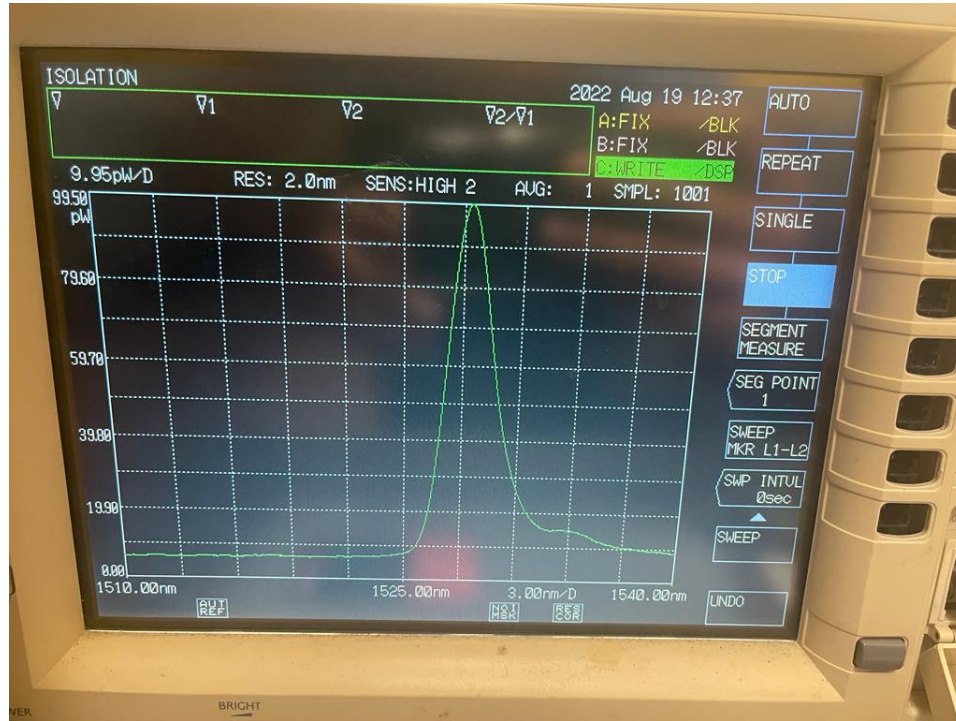


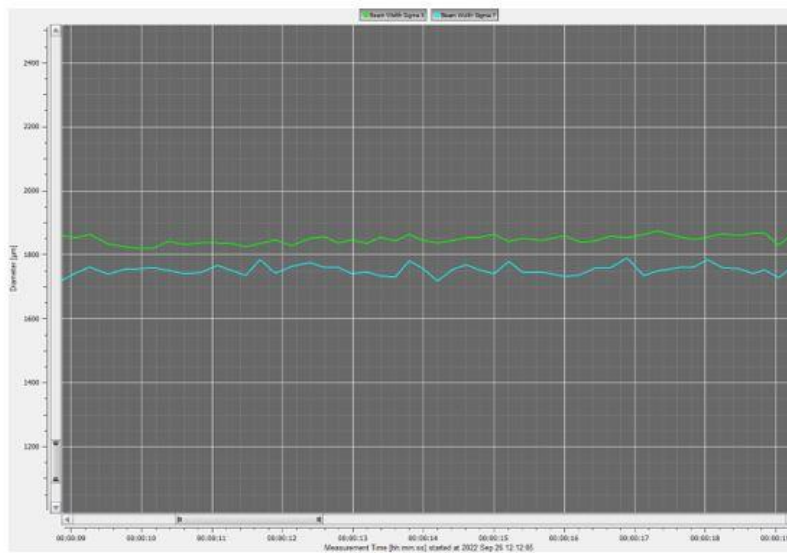
Figure 4.5: SPDC Signal Obtained on the OSA at 25 °C

As a result of this experiment, it was found that the QPM temperature is around 23°C with the SPDC signal being detected at 1528 nm.

4.2.3 Beam Profiling

Using a scanning slit beam profiler, 1528 nm and 1064 nm beam diameters could be measured and compared with the expected values used in the simulation. Figure 4.6 shows the 1064 nm beam diameters (a) at 5" after the OC (b) after the OC. Figure 4.7 shows the Gaussian beam shape obtained for 1064 nm.

(a)



(b)

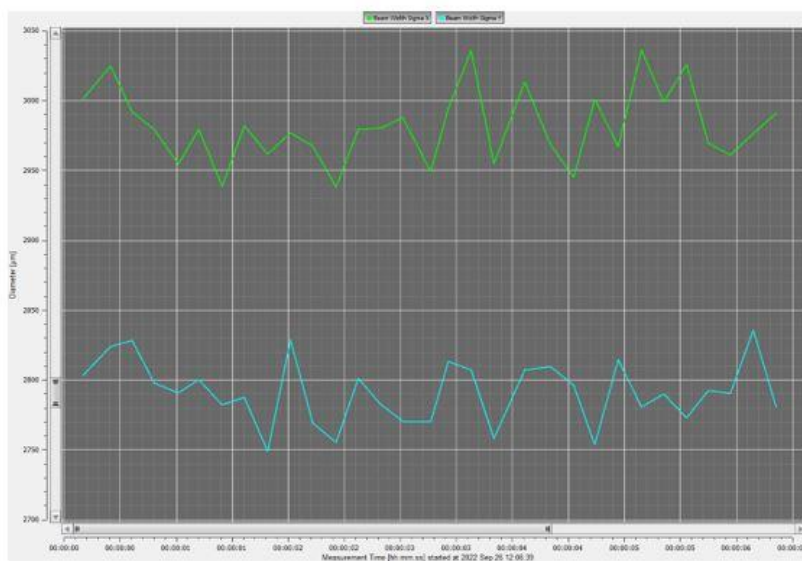


Figure 4.6: (a) 1064 nm Beam Diameter 5" after the OC (b) 1064 nm Beam Diameter 8.35" After the OC

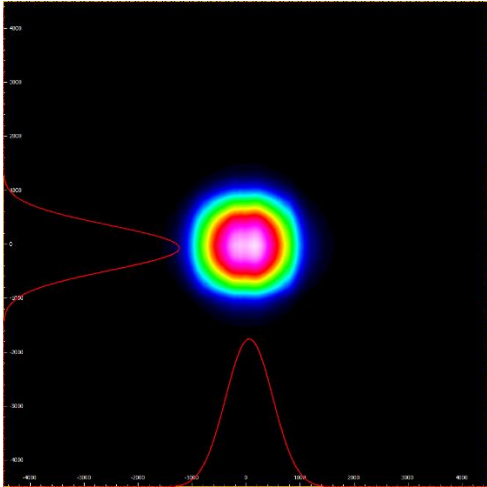


Figure 4.7: 1064 nm Beam Profile 5" After the OC

In summary, the results of 1064 nm beam profiling showed that a 145 μm beam waist assumption inside the cavity is valid. The minimum 1528 nm beam waist was also verified using the beam profiler. At a distance of 10.5 cm from the focusing lens, 110 μm beam waist was obtained as shown in Figure 4.8.

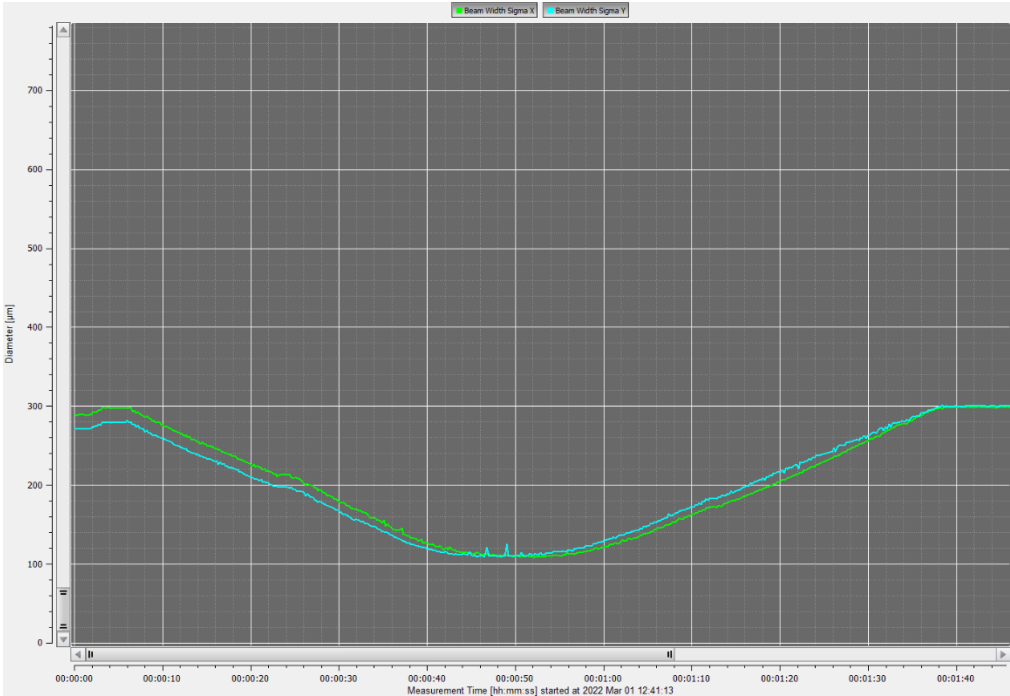


Figure 4.8: 1528 nm Minimum Beam Diameter at 10.5 cm From the Focusing Lens

4.3 Experimental Results

The first obtained set of results is the 1064 nm leaking power as a function of the 808 nm pump power. The experimental results were plotted along with the simulation results as shown in Figure 4.9. The simulation used a spatially dependent rate equation model to calculate the intracavity 1064 nm power. The test was conducted with all optical components inside the resonator cavity, and the calculated total linear loss was used in the simulation. The PPLN temperature was controlled to maximize the nonlinear conversion efficiency. The experimental and simulation results show a good agreement.

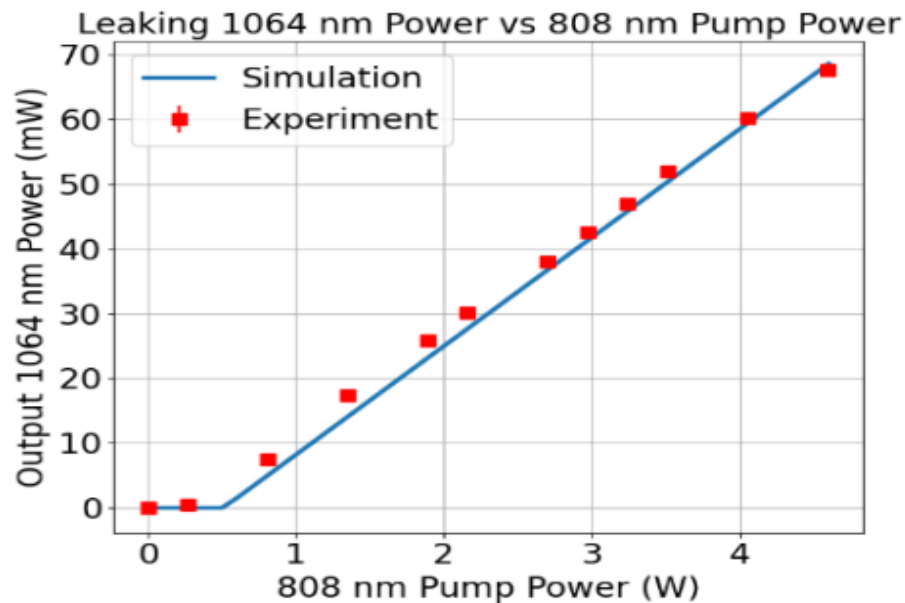


Figure 4.9: Experimental and Simulation Results for Leaking 1064 nm Power Against 808 nm Power

The second set of results was obtained after coupling the 1064 nm and 1528 nm into the PPLN. The maximum obtained DFG power was 8.1 mW with 4.5 W 808 nm pump power and 170 mW C-band power. The experimental data was compared with a DFG simulation based on a coupled nonlinear wave equation model reported by our research group [79]. Figure 4.10 shows the obtained experimental and simulation DFG results. The simulation overestimates the DFG power by ~ 20%. The discrepancy can be explained by a non-ideal overlap of the pump and signal beams inside the PPLN.

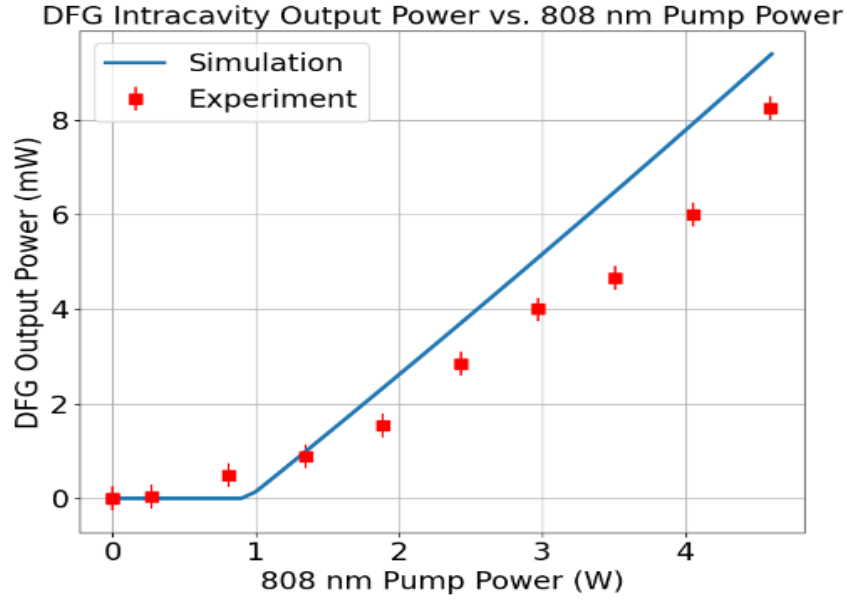


Figure 4.10: Experimental and Simulation DFG Output Power vs 808 nm Pump Power

One important metric to compare the efficiency of the DFG laser is the black box efficiency defined as:

$$\eta = 100\% \times \frac{P_{DFG}}{P_{pump}P_{signal}} \quad (4.1)$$

Where P_{DFG} is the DFG power in mW, P_{pump} is the 808 nm optical power in W, and P_{signal} is the C-band optical power in W. In our case, Figure 4.11 shows the values used to obtain the black box efficiency.

The calculated black box efficiency was 1.058% W^{-1} which is, to the best of our knowledge, the highest value reported for a continuous wave (CW) DFG laser based on a bulk nonlinear optical crystal.

To study the tunability of the DFG laser, the black box efficiency was obtained as a function of the signal wavelength. Figure 4.12 shows that the black box efficiency drops to 0 if the signal wavelength is moved by more than 2 nm while keeping the PPLN temperature at 23 °C.

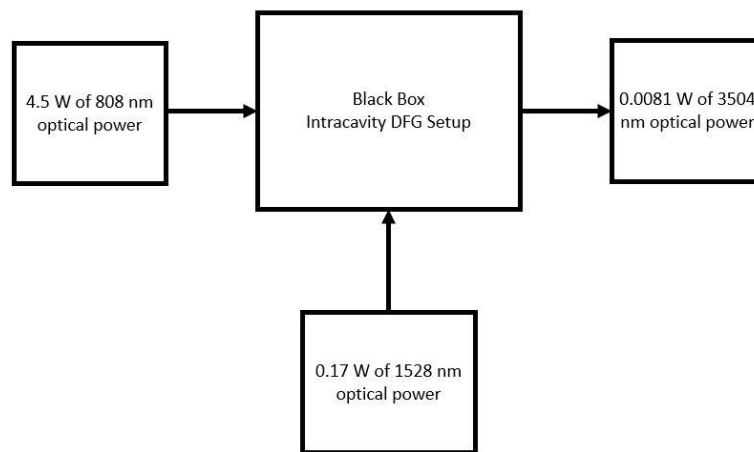


Figure 4.11: Black Box Efficiency Diagram

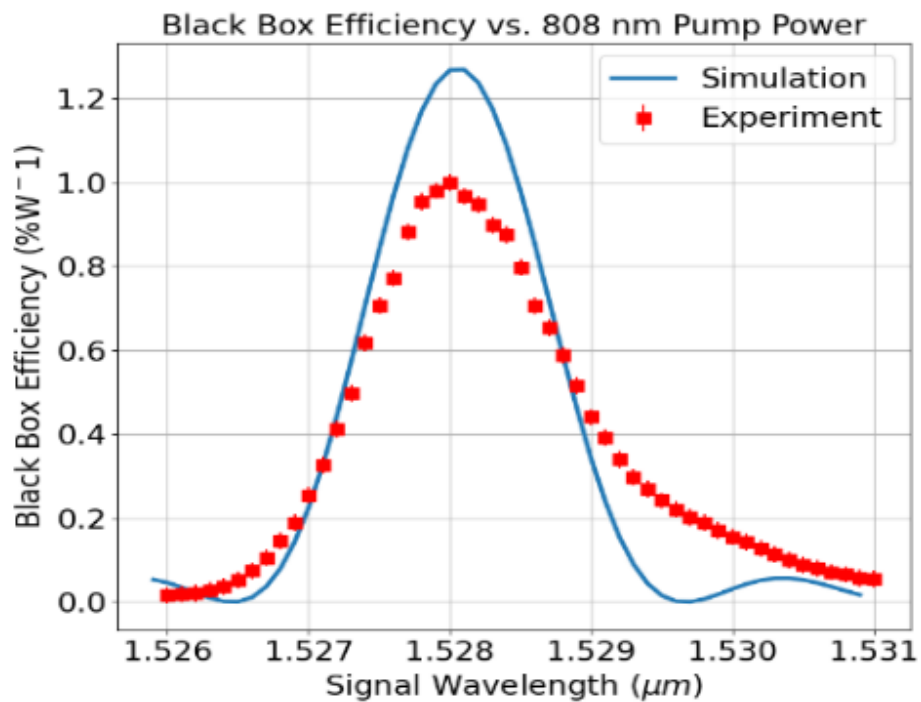


Figure 4.12: Experimental and Theoretical Black Box Efficiencies as a Function of Signal Wavelength

The temperature tolerance of the DFG laser was studied by obtaining the temperature tuning curve. In this experiment, the temperature of the PPLN was changed and the output DFG power was recorded. The experimental results were compared with the simulation results that take into consideration the Sellmeier equation for MgO doped lithium niobate.

Figure 4.13 shows the results of this study. The temperature tolerance was shown to be large enough, which makes our DFG laser a potential laser source for many practical applications such as remote gas sensing.

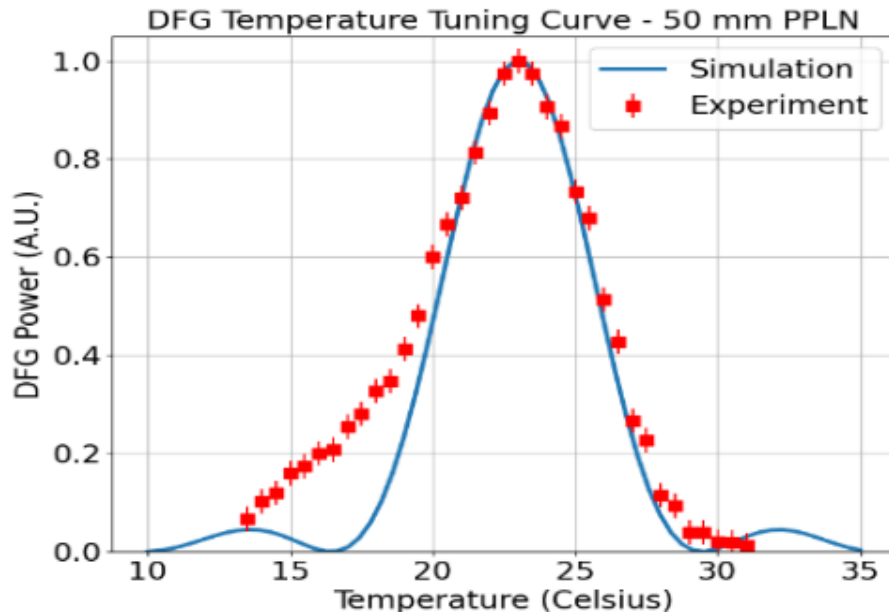


Figure 4.13: Measured and Theoretical Temperature Tuning Curves

The peaks' location of the simulation and experimental results show a good agreement. However, the Peltier element struggled to operate at temperatures less than 20 °C, which explains the mismatch between the experimental and simulation results on the left hand side of the graph.

4.4 Discussion

4.4.1 DFG Power Enhancement

The maximum achieved DFG power was 8.1 mW. However, if a higher power is required for a long range sensing, the power can be enhanced in some obvious ways:

- 1- Increase 1064 nm power by pumping with a higher 808 nm optical power. By pumping the Nd:YVO₄ with a higher 808 nm power, the 1064 nm intracavity power is expected to increase, and, eventually, an increase in DFG power is expected assuming the following does not occur: the higher pumping power does not induce thermal induced damage in the Nd:YVO₄, and thermal lensing is not heavily affecting the 1064 nm beam diameter and stability.
- 2- Optimize the coating conditions of all optical elements used in the setup. In the best case scenario, the performance of all AR and HR coatings would be desired to be >99.9%. By optimizing the coating, the black box efficiency can be boosted up to more than 3%W⁻¹.
- 3- Increase the C-band signal power: theoretically, if a 10W EDFA is used for the signal wavelength, the DFG power can be boosted up to more than 500 mW as shown in Figure 4.14. As a result, by implementing some coating optimization and using a 10W EDFA, a watt level DFG power can be predicted.

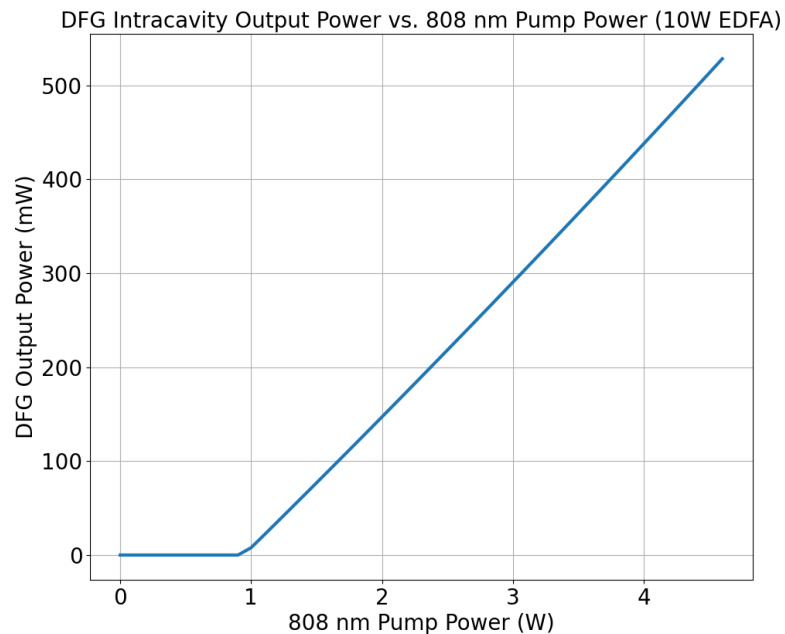


Figure 4.14: Expected MWIR DFG Power with 10W EDFA

4.4.2 Wavelength Tunability

The end goal of this laser is to be used in methane detection. MWIR was chosen for the advantages this wavelength range brings over the SWIR region. As a result, we must ensure the MWIR wavelength selected matches the largest absorption lines to maximize sensitivity to methane. Figure 4.15, shows the absorption spectrum of methane in the MWIR region obtained from the HITRAN database.

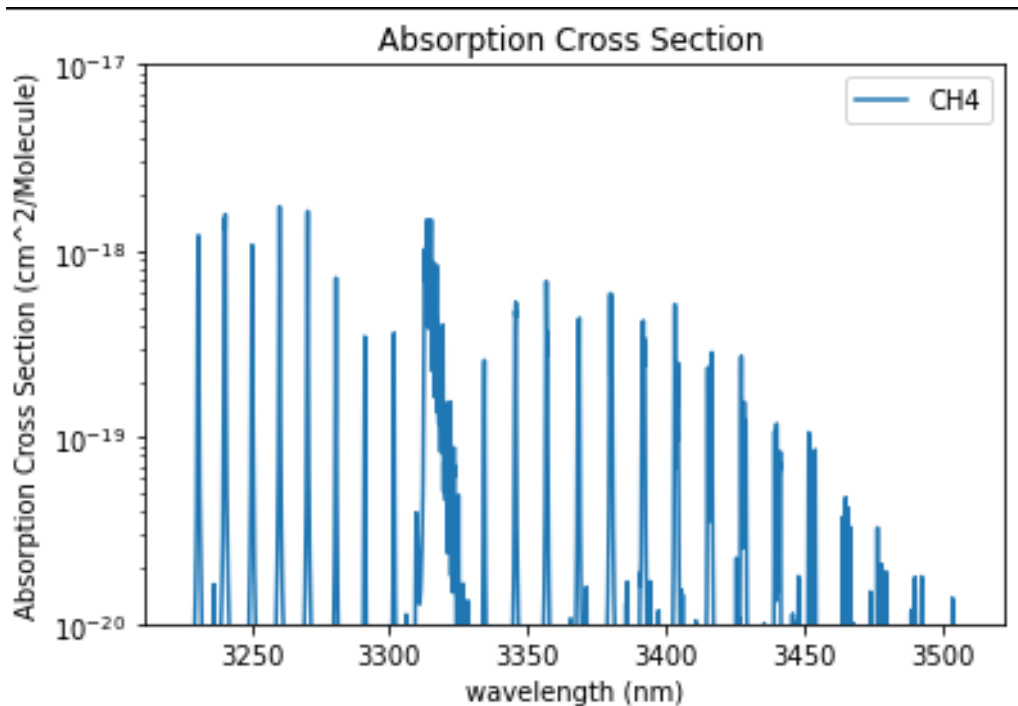


Figure 4.15: Methane Absorption Spectrum in the MWIR Region

Although the obtained DFG wavelength matches with one of methane's absorption lines in the MWIR at 3.504 μm , two orders of magnitude improvement can be seen if the wavelength was around 3.39 μm . This is no problem for our device, as the period can be easily tuned between 3.32 μm and 3.52 μm by varying the poling period of the crystal. This can be coupled with operating at the QPM temperature to obtain a specific wavelength while keeping the pump wavelength at 1064 nm and the signal wavelength in the C-band region. For example, if a 30.49 μm poling period is chosen, 1064 nm pump wavelength,

1550 nm signal wavelength, and 57 °C QPM temperature, a 3.39 μm DFG wavelength can be obtained.

4.4.3 DFG Linewidth

In molecular spectroscopy, very narrow linewidth lasers (100kHz) are desired [67]. The linewidth of the MWIR DFG laser is defined by the linewidth of the pump and signal beams. The linewidth of the 1528 nm signal is in the pm range since it is a single frequency laser. However, the linewidth of 1064 nm pump is around 0.1 nm (~ 25 GHz), which is the main limitation for the linewidth of the generated MWIR DFG signal. This results in a linewidth on the order of 25 GHz for the current iteration of the laser in the MWIR. In order to make the DFG linewidth more narrow, the linewidth of 1064 should be reduced; the most straightforward way to do so being the insertion of a Fabry-Perot (F-P) etalon into the cavity, where the linewidth of 1064 nm pump can be brought down to kHz levels [92,100,101].

4.5 Conclusion

A mid-wave infrared (MWIR) laser source was described in this chapter. The laser source was based on an intracavity difference frequency generation (DFG). The obtained black box efficiency is the best reported value, to the best of our knowledge. In addition, the compact design of the laser, potential output power, wavelength tunability, and potential narrow linewidth make it a great future source for mixed gas detection especially that it is operating at a wavelength that gets strongly absorbed by methane. With the current setup, the maximum obtained power is 8.1 mW, the achieved blackbox efficiency is 1.058% W^{-1} . In addition, the temperature tolerance of the setup was shown to be 5°C. The obtained MWIR linewidth was in the GHz order. Potential watt level MWIR power was shown to be achievable with some coating optimization.

Chapter 5

5 Long Wavelength Infrared Laser Source for Natural Mixed Gas Leak Detection

5.1 Introduction

Methane gas has a strong absorption line in the long wave infrared (LWIR) region as shown in Figure 5.1. This absorption line is two orders of magnitude higher than in the short wave infrared region. The high transmission of LWIR is another reason that makes LWIR sources a great potential candidate for gas detection. Away from the absorption line of some gases, such as methane, LWIR sources rarely get absorbed, attenuated, or scattered [93]. As a result, noise and cross talk are not a concern when operating in the LWIR region. Advancement in LWIR laser sources is needed to satisfy the requirements for methane detection. Quantum cascade lasers (QCL) have been demonstrated to work in the LWIR region. However, QCLs' operating temperature is required to be at liquid nitrogen temperature for peak performance which requires a complicated and costly temperature control system. An alternative approach to generate LWIR is to use nonlinear optics (NLO). The non linear crystal shall be transparent in the LWIR region in order to be usable in LWIR generation. the upper transparency limit of periodically poled lithium niobate (PPLN) is around $4.5 \mu\text{m}$, which makes it incapable of generating LWIR. A promising nonlinear medium for LWIR generation is orientation-patterned semiconductors (OP-SCs) such as gallium arsenide (GaAs) or gallium phosphide (GaP) that are transparent up to $18 \mu\text{m}$ [93]. OP-GaP has a smaller nonlinear coefficient than OP-GaAs. However, OP-GaAs has a strong absorption at $1 \mu\text{m}$ relative to OP-GaP. Thus, OP-GaAs does not tolerate $1 \mu\text{m}$ pumping [99]. In order to avoid the strong absorption at shorter wavelengths, OP-GaP is preferred, and the pump wavelength can be moved to a longer wavelength such as 1.34

μm , which is another laser transition available to Nd:YVO₄. In this chapter, the same difference frequency generation intracavity design that was used to generate mid wavelength infrared (MWIR) is studied for potential LWIR generation using Op-GaP.

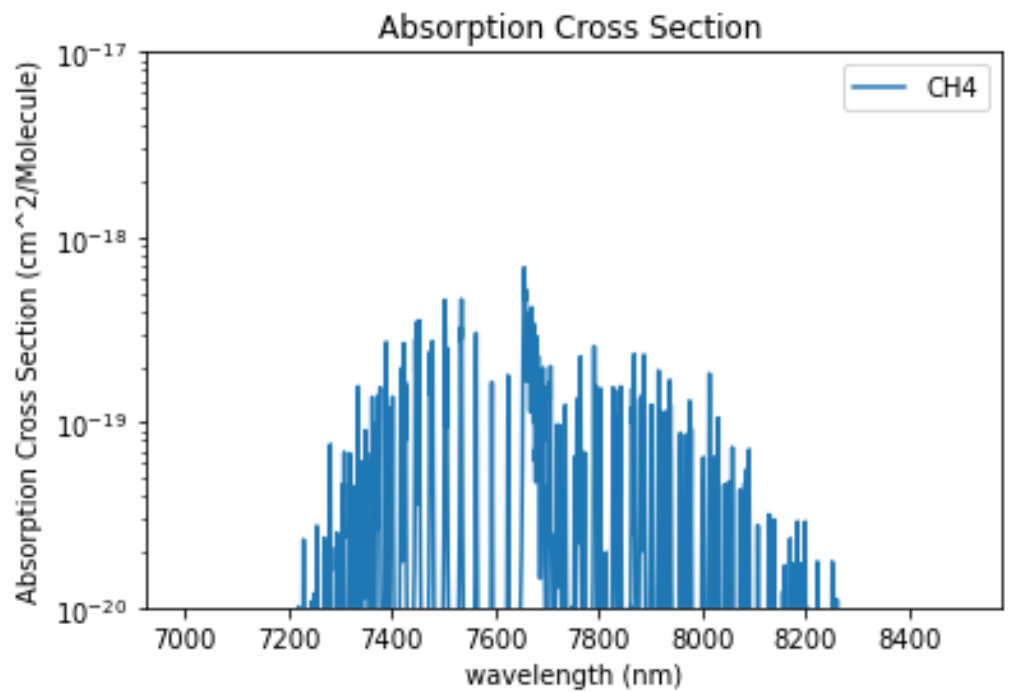


Figure 5.1: Methane Absorption Spectrum in the LWIR Region

5.2 Experimental Setup

In order to generate LWIR, an Intracavity DFG setup is studied in this chapter. The expected LWIR wavelength is chosen to be around $7.7 \mu\text{m}$. The pump wavelength is chosen to be $1.34 \mu\text{m}$ instead of $1.064 \mu\text{m}$ for better performance and lower absorption in the OP-GaP nonlinear crystal. As a result, the signal wavelength has to be in the L-band in order to satisfy the conservation of energy rule. Figure 5.2 shows the studied design for LWIR generation in this chapter.

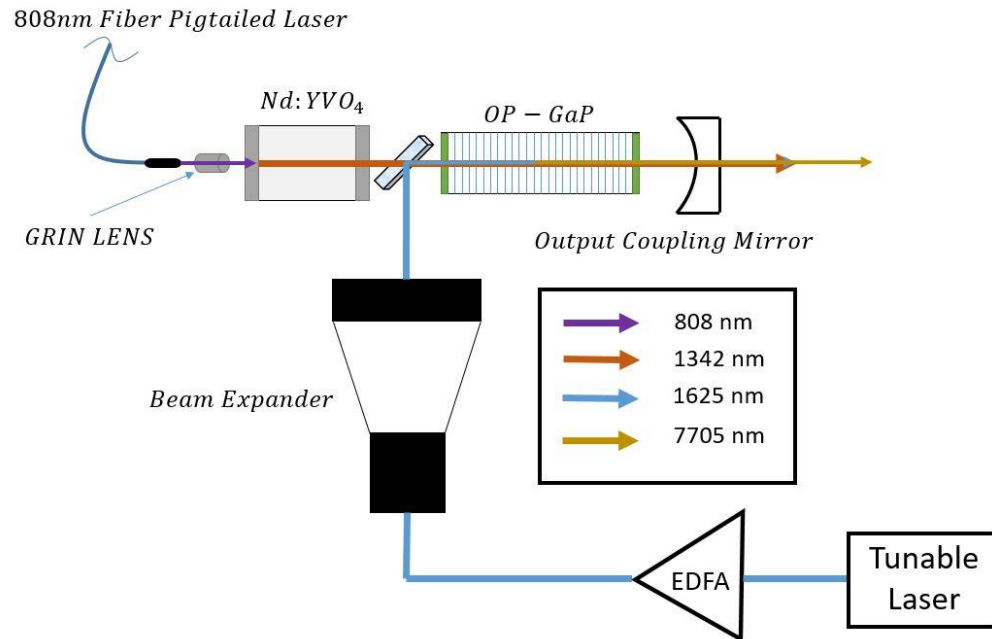


Figure 5.2: Schematic Diagram of the LWIR Laser

In this work, an intracavity structure is used with Nd:YVO₄ as the fundamental crystal. Nd:YVO₄ is capable of producing a 1342 nm beam that serves as the pump for the nonlinear DFG process. The gain medium is pumped with an 808 nm fiber pigtailed laser. The intracavity structure contains an OP-GaP as the nonlinear crystal. The signal source is an amplified tunable L-band laser. To couple the signal and pump in the OP-GaP, a dichroic mirror is inserted inside the resonator cavity that reflects the signal beam towards the Op-GaP.

The multimode 808nm fiber pigtailed diode laser has a 125 μm core diameter. A 4.5 W 808 nm optical power was focused onto the Nd:YVO₄ using an anti-reflection (AR) coated at 810 nm GRIN lens. The Nd:YVO₄ is high-reflective (HR) coated at 1342 nm ($R > 99.9\%$) and high-transmission coated at 808 nm ($T > 95\%$) at the input facet. At the output facet, the Nd:YVO₄ is AR coated at 1064 nm ($T > 99.8\%$). The dimensions of the Nd:YVO₄ are 3mm (W) x 3mm (H) x 5mm (L), and the doping concentration is 1.1%. The output coupling (OC) mirror is plano-concave with a 100 mm radius of curvature. The input facet of the OC is HR coated at 1342 nm ($R > 99.85\%$).

As a first step, the intracavity 1342 nm power shall be obtained. A simple design shown in Figure 5.3 was used to study the achievable intracavity 1342 nm power. Using a combination of experimental and theoretical values, the expected LWIR generated power can be simulated. The logical flow of the study conducted in this chapter is shown in Figure 5.4.

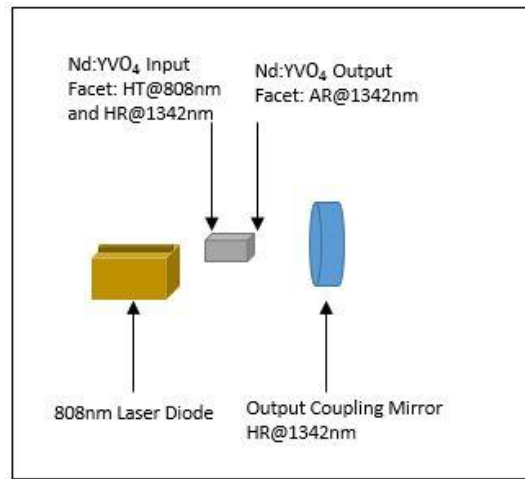


Figure 5.3: Schematic Diagram of 1342 nm Diode Pumped Solid State Laser

The experimental procedure for the 1342 nm experiment is similar to what was described in 4.2.1. The temperatures of the laser diode and Nd:YVO₄ were controlled using a TEC-heat sink-fan assembly. Each of the 3 components shown in Figure 5.3 was mounted on 5 axis stage to align the components with respect to each other.

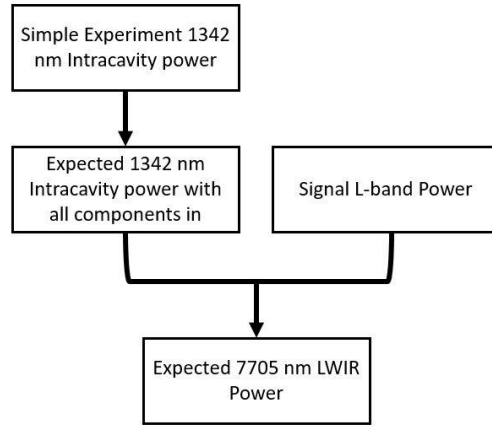


Figure 5.4: Logical Flow of LWIR Study

5.2.1 1342nm Pump Laser - Experimental Results

The obtained leaking 1342 nm experimental and simulation results for the simple setup is shown in Figure 5.5. The solid blue line shows the simulation results with a good agreement with the experimental results. Saturation effects can be seen at around 4W 808nm pumping power due to thermal lensing that is not modeled in the simulation. The saturation effect can be avoided by using a Nd:YVO₄ crystal with a lower doping concentration.

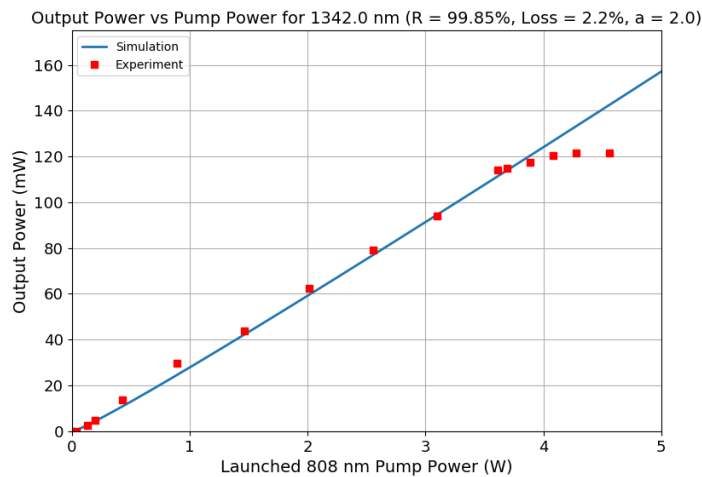


Figure 5.5: Experimental and Simulation Leaking 1342nm Powers

From the leaking 1342 nm power, the equivalent intracavity power can be calculated as shown in Figure 5.6. The intracavity power is important since it shows the available pump power inside the resonator cavity.

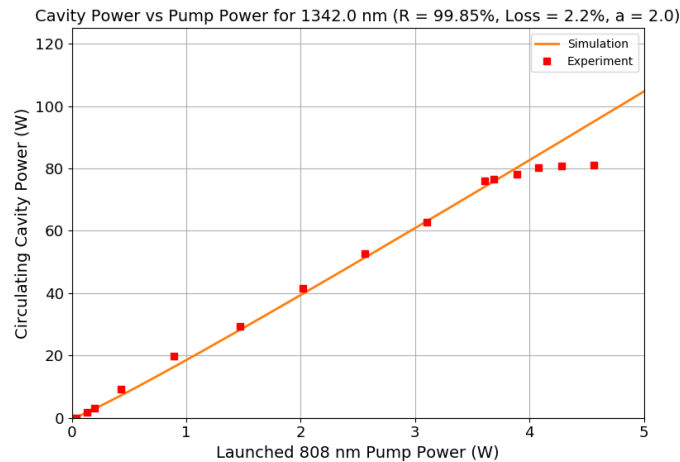


Figure 5.6: Experimental and Simulation Intracavity 1342nm Powers

5.2.2 1342 nm Beam Profiling and Linewidth

Using a scanning slit beam profiler, the beam profile for the 1342 nm laser outside the OC can be obtained as shown in Figure 5.7. The measurement shows a circular Gaussian beam spot with a $600 \mu\text{m}$ diameter 20 mm after the OC the beam spot size is big compared to what was obtained for 1064 nm. Changing the laser diode to a fiber pigtailed laser and adding a GRIN lens to focus the pump beam into the Nd:YVO₄ would decrease the beam diameter.

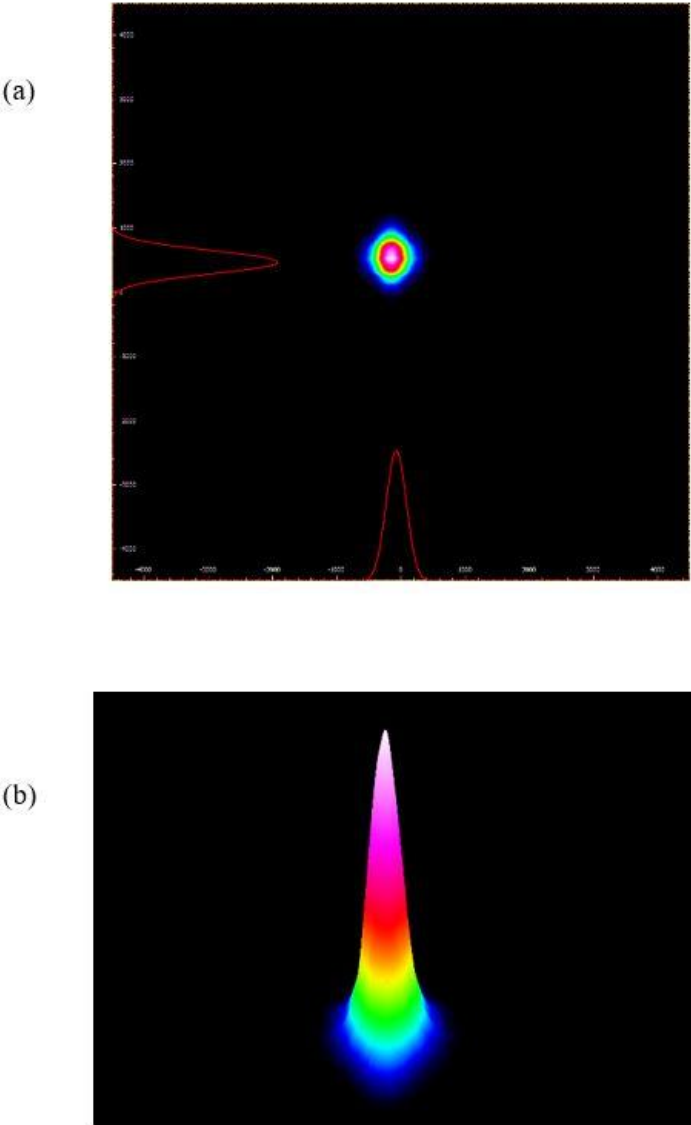


Figure 5.7: (a) 1342 nm 2D Beam Profile (b) 1342 nm 3D Beam Profile

Figure 5.8 shows a screenshot from the OSA screen showing the wavelength at 1342 nm. The linewidth of the obtained beam is around 0.1 nm.

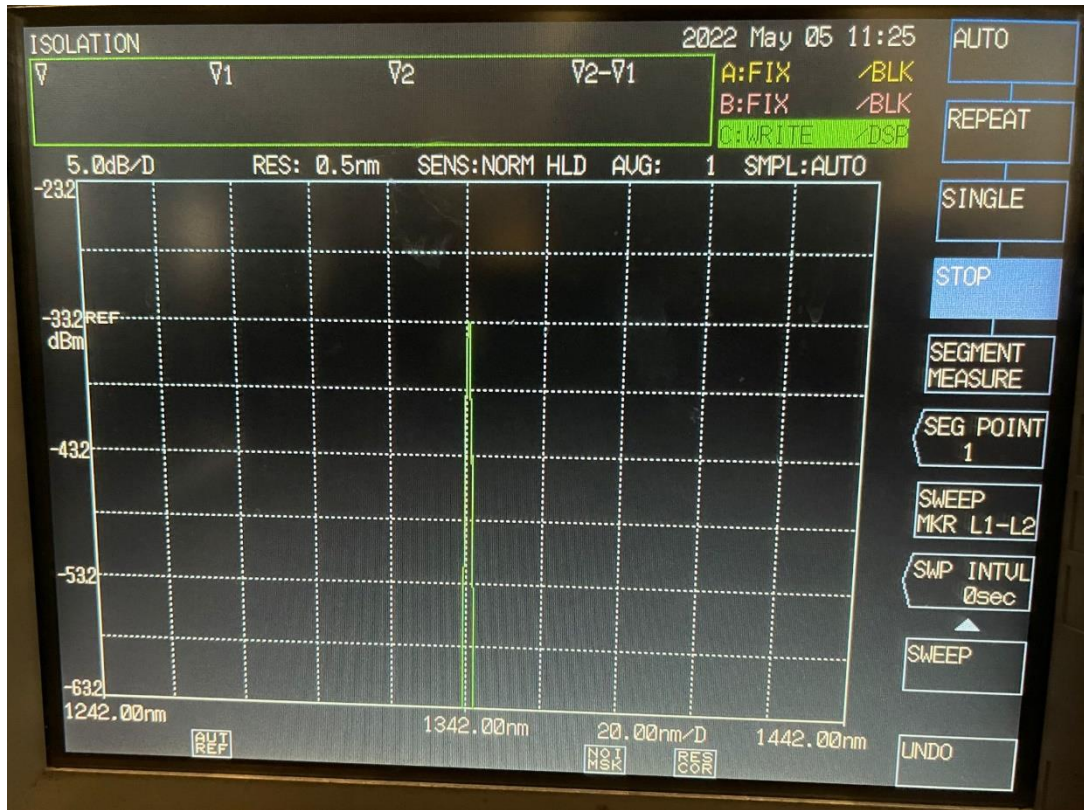


Figure 5.8: Screenshot of the OSA at 1342 nm

5.3 LWIR Simulation

Assuming the setup shown in Figure 5.2 is used with the available 1342 nm intracavity power achieved in pump experiment, a simulation prediction of the achievable LWIR power can be estimated. The simulation uses a 4 W input signal power at 1625 nm combined with the obtained 1342 nm power, and a total linear loss inside the cavity that is equivalent to the current measurements for the MWIR DFG setup. Because of the high absorption loss at the pump wavelength for OP-GaP, the simulation shows in Figure 5.9 that LWIR generation is not feasible with the current setup. If the 1342 nm pump does not saturate at 4 W, some LWIR generation can be observed with a 5.5W 808 nm threshold.

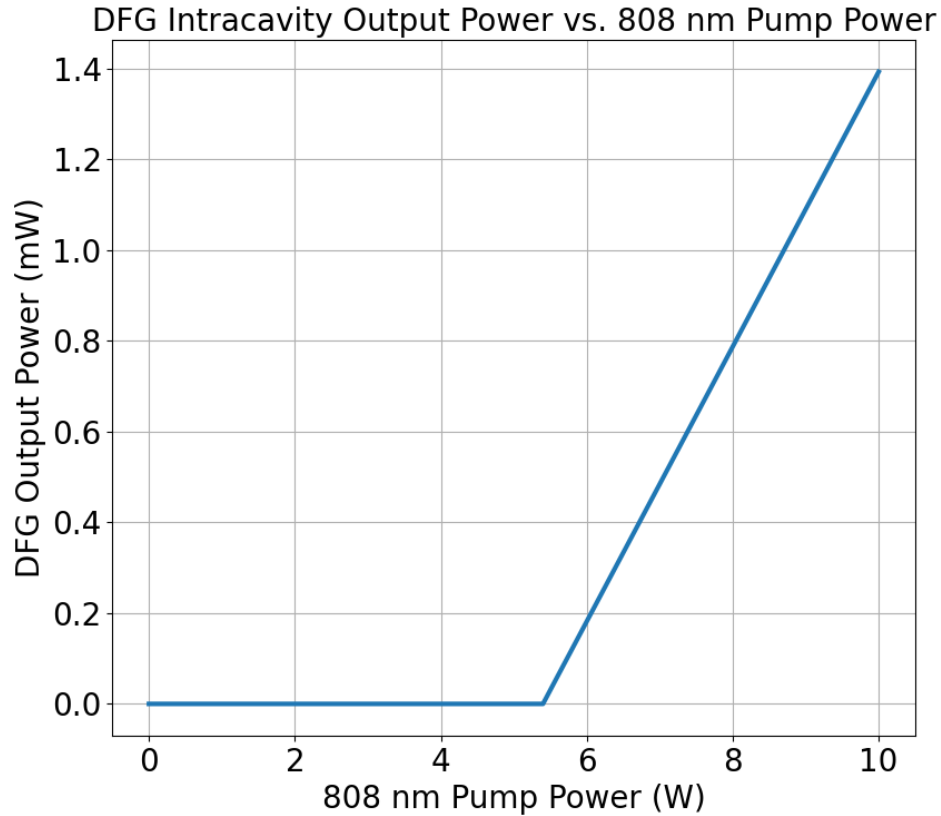


Figure 5.9: Simulation Results for LWIR Power against 808 nm Pump Power

The simulation assumed a 10 mm long Op-GaP crystal, and the outcome of this study shows that the proposed setup does not offer a great opportunity for LWIR generation mainly due to the high absorption. Some of the potential solutions are proposed in the following section.

5.4 Alternative LWIR Generation Methods

In an intracavity structure, the loss at the pump wavelength induced by any component inside the resonator cavity hugely affects the achievable power. Due to the high absorption loss of GaP at 1342 nm, the expected power level of LWIR is low. As a result, an alternative approach shall be considered to enhance the overall performance.

- First alternative solution is to optimize the GaP crystal's length. The power scales quadratically with the OP-GaP length, but it decays exponentially with length as well due to the added absorption loss induced due to the extra OP-Gap length. Figure 5.10 shows a plot of the expected maximum power at 10W 808 nm pumping and 4W 1625 nm signal for various OP-GaP crystal lengths. The maximum expected power peaks at around 12 mm GaP length before it starts to decrease. Even with optimized OP-GaP length at 12 mm, the maximum expected power with the current setup is not satisfactory, so moving to other structures such as single pass lasers may seem an alternative option.

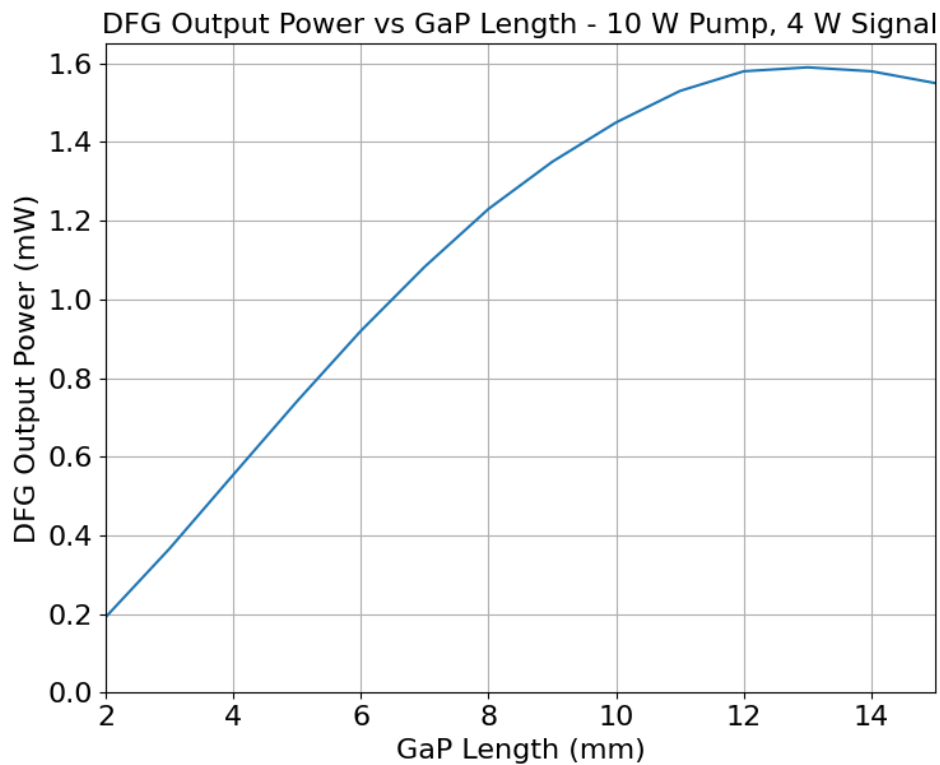


Figure 5.10: DFG Output Power at 10 W 808 nm Pumping and 4 W 1625 nm Signal Power as a Function of GaP Length

- The second option is to use a single pass setup with 1342 nm (0-10W) and 1625 nm (4W) in a 10 mm OP-Gap which lowers the effect of absorption loss. The expected

power levels of such a setup is shown in Figure 5.11. The maximum expected LWIR power is around 20 mW.

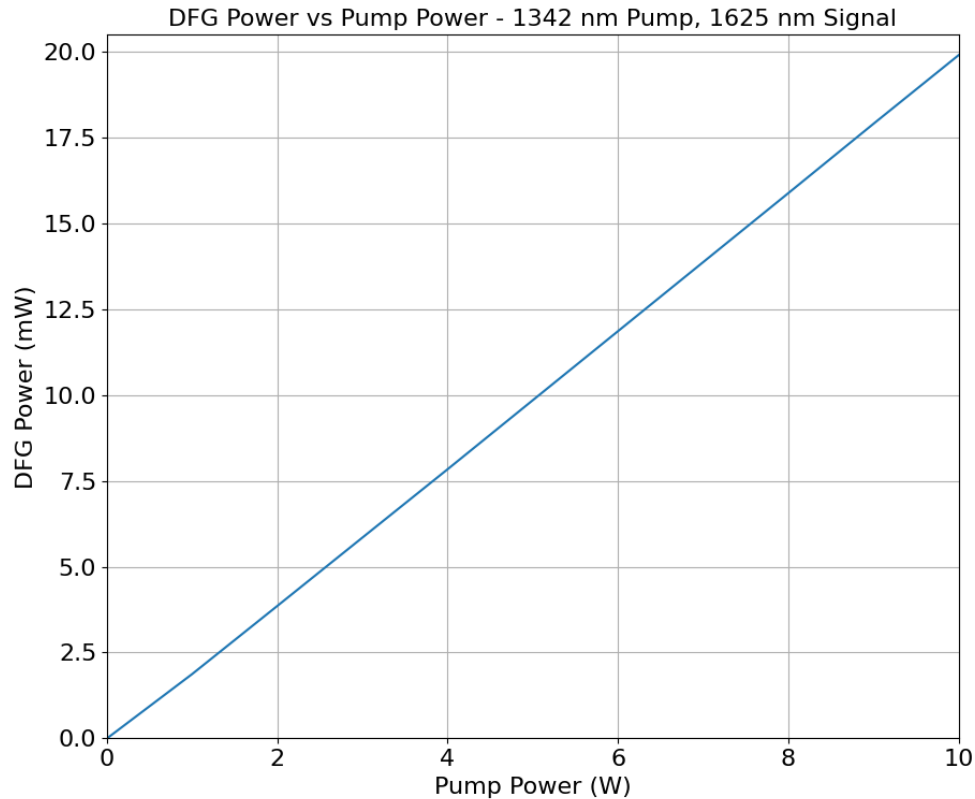


Figure 5.11: LWIR Generation with a Single Pass Structure 1342 nm Pump and 1625 nm Signal

- Third, a single pass setup can be used with the pump wavelength moved to 1550 nm, and the signal wavelength set at 1950 nm (4W). In this case, two high power fiber lasers can be used to generate LWIR using OP-GaP. The simulation result of this study is shown in Figure 5.12. The maximum expected LWIR power is 17.5 mW.

Single Pass structures show an enhanced performance over the intracavity structure due to the reduced effect of absorption loss in such structures. Short pump and signal wavelengths show a better performance than longer pump and signal wavelengths. However, comparing these expected results with the expected watt-level MWIR DFG results expected in chapter 5 leads to the conclusion that our proposed MWIR DFG laser is superior to the LWIR DFG laser. In addition, available commercial detectors

that work in the MWIR region are superior to their counterparts in the LWIR region which facilitates the overall detection procedure when working in the MWIR region.

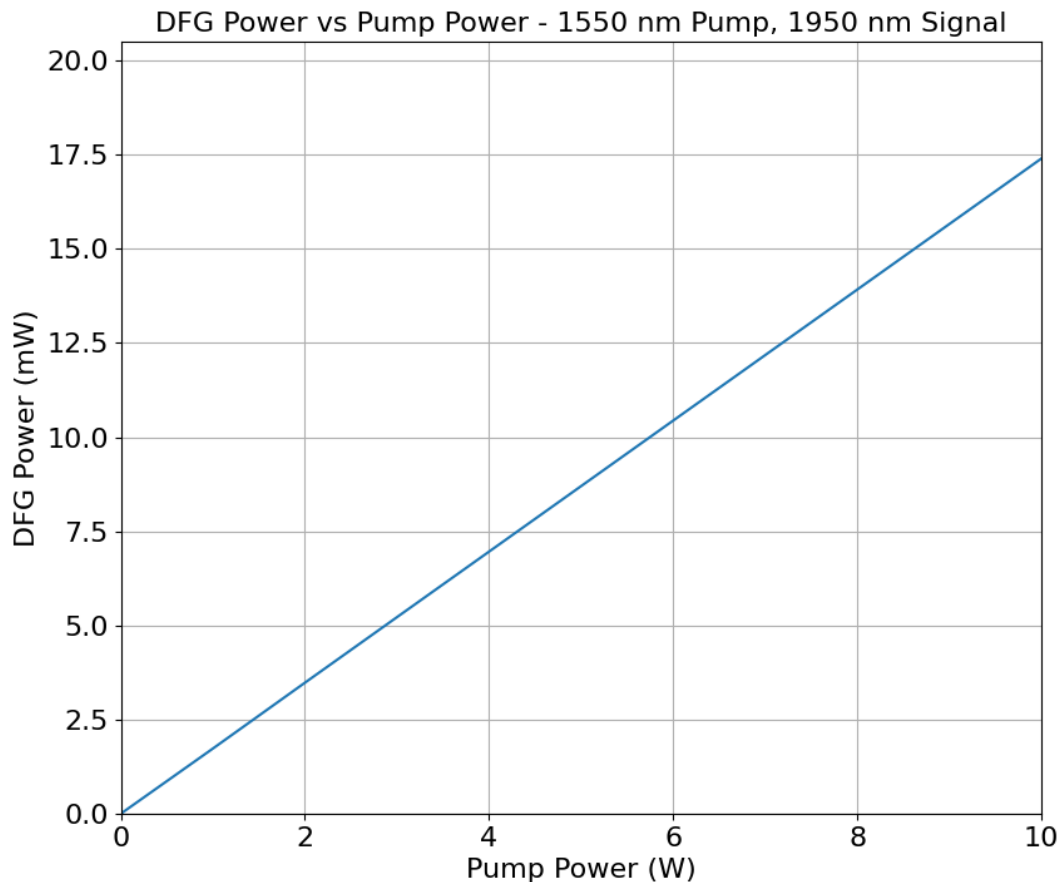


Figure 5.12: LWIR Generation with a Single Pass Structure 1550 nm Pump and 1950 nm Signal

5.5 Conclusion

In this chapter, some methods for long wave infrared (LWIR) generation are discussed. The first method was using an intracavity difference frequency generation structure using orientation patterned gallium phosphide as a nonlinear medium inside the resonator cavity. The pump wavelength was 1342 nm with a 1625 nm signal wavelength to get $7.705 \mu\text{m}$ output wavelength. Weak output power of 1.6 mW at LWIR was expected

to be obtained with the intracavity structure with a GaP crystal 12mm long. As a result, different structures were studied. The second structure was a single pass one with 1342 nm as a pump signal and 1625 nm as a signal wavelength. Better LWIR powers are expected in this setup with a maximum power of 20mW. A third option with 1550 nm pump and 1950 nm signal was studied. The LWIR output power was 17.5mW which is slightly less than what is expected in the second option. This study sets the path that might be taken to generate a high power LWIR signal. With the current results, watt level LWIR is not achievable. Other options such as Intracavity optical parametric oscillators (OPO) might be a potential track to optimize the LWIR generation.

Chapter 6

6 Thesis Summary

6.1 Summary

In this work, two main issues in hydrogen blended natural gas were discussed. The first issue is measuring the calorific value of a mixed gas. A non destructive measurement technique using ultrasonic transducers was studied. The proposed method was based on calculating the composition of a mixed gas by obtaining the speed of sound in a mixture. The method was validated with nitrogen-oxygen gas mixtures, and it was proven to have a high accuracy in measuring the volumetric composition of a mixed gas. After knowing the limitation of the current method, the maximum expected error in mixed natural gas composition measurement was calculated to be less than 0.1%. In addition, An ultrasonic flow meter was also studied and implemented to help in measuring the total energy flow rate. The % error in the flow rate measurement was less than 28% showing that there is a room for improvement in this measurement. In conclusion, the non-destructive ultrasonic composition testing technique showed some promising results to be used as a method for calorific measurements in mixed natural gas.

The second issue was leak detection of mixed natural gas. A novel and high efficient mid wave infrared (MWIR) laser source was proposed and implemented to be used in direct absorption spectroscopy. The continuous wave laser source used an intracavity structure and a difference frequency generation phenomenon in a periodically poled lithium niobate crystal. The obtained results show the highest reported black box efficiency of 1.058%, to the best of our knowledge. The maximum achieved power in the current setup was 8.1 mw, the linewidth was in the Ghz order, and the laser had a temperature tolerance of 5°C. the

experimental and simulation results showed a great agreement. Watt level MWIR generation was predicted by implementing some optimization procedures on the setup. As a result, the developed laser is a promising source for methane leak detection.

A similar setup was used to study the feasibility of long wave infrared generation. an orientation patterned gallium phosphide crystal was proposed as a nonlinear crystal. The pump wavelength was a 1342 nm diode pumped solid state laser and the signal was chosen to be in the L-band at 1625 nm. The outcome of the study showed that proposed structure results in a 1.4 mW LWIR achievable power with a 10 mm long GaP crystal. By optimizing the GaP crystal length, it was shown that this achievable power can be boosted up to 1.6 mW with a 12 mm long GaP crystal. A single pass structure was studied with the same pump and signal wavelengths. 20 mW LWIR power was shown to be expected from this setup. A third single pass setup with 1550 nm pump and 1950 nm signal was simulated and showed a maximum power of 17.5 mW.

This thesis contributes to advancing the research in mixed natural gas testing and discusses some main potential solutions that ease the way towards less greenhouse gas emissions.

6.2 Skills Acquired

The work done in this thesis project helped me acquire some advanced skills in setting up diode pumped solid state lasers, and aligning optical components. In addition, the projects helped me boost my knowledge in optical and mechanical designs. The use of MATLAB, ANSYS and SOLIDWORKS added an additional set of software skills to my set of skills. Furthermore, by working on an industrial project with Romet Limited, I was able to work closely with an industry partner which enhanced my professional and coordination skills. Working with a team of highly skilled colleagues boosted my teamwork capabilities.

7 References

- [1] “Greenhouse gas | Definition, Emissions, & Greenhouse Effect | Britannica.” <https://www.britannica.com/science/greenhouse-gas> (accessed Nov. 18, 2022).
- [2] “Overview of Greenhouse Gases | US EPA.” <https://www.epa.gov/ghgemissions/overview-greenhouse-gases> (accessed Nov. 18, 2022).
- [3] “What are the main man-made greenhouse gases? | Environment | The Guardian.” <https://www.theguardian.com/environment/2011/feb/04/man-made-greenhouse-gases> (accessed Nov. 18, 2022).
- [4] A. George *et al.*, “A Review of Non-Thermal Plasma Technology: A novel solution for CO₂ conversion and utilization,” *Renew. Sustain. Energy Rev.*, vol. 135, p. 109702, Jan. 2021, doi: 10.1016/J.RSER.2020.109702.
- [5] “Climate Change Indicators: Greenhouse Gases | US EPA.” <https://www.epa.gov/climate-indicators/greenhouse-gases> (accessed Nov. 18, 2022).
- [6] “Greenhouse gas emissions - Canada.ca.” <https://www.canada.ca/en/environment-climate-change/services/environmental-indicators/greenhouse-gas-emissions.html> (accessed Nov. 18, 2022).
- [7] “Annual CO₂ emissions worldwide 1940-2020 | Statista.” <https://www.statista.com/statistics/276629/global-co2-emissions/> (accessed Nov. 18, 2022).
- [8] “Understanding Global Warming Potentials | US EPA.” <https://www.epa.gov/ghgemissions/understanding-global-warming-potentials> (accessed Nov. 18, 2022).
- [9] M. Saunois *et al.*, “The global methane budget 2000-2017,” *Earth Syst. Sci. Data*,

vol. 12, no. 3, pp. 1561–1623, Jul. 2020, doi: 10.5194/ESSD-12-1561-2020.

- [10] “Predictions of Future Global Climate | Center for Science Education.” <https://scied.ucar.edu/learning-zone/climate-change-impacts/predictions-future-global-climate> (accessed Nov. 18, 2022).
- [11] “Greenhouse gas emissions: drivers and impacts - Canada.ca.” <https://www.canada.ca/en/environment-climate-change/services/environmental-indicators/greenhouse-gas-emissions-drivers-impacts.html> (accessed Nov. 18, 2022).
- [12] “Greenhouse gases, facts and information.” <https://www.nationalgeographic.com/environment/article/greenhouse-gases> (accessed Nov. 18, 2022).
- [13] “Global Climate Agreements: Successes and Failures | Council on Foreign Relations.” <https://www.cfr.org/background/paris-global-climate-change-agreements> (accessed Nov. 18, 2022).
- [14] “Government of Canada confirms ambitious new greenhouse gas emissions reduction target - Canada.ca.” <https://www.canada.ca/en/environment-climate-change/news/2021/07/government-of-canada-confirms-ambitious-new-greenhouse-gas-emissions-reduction-target.html> (accessed Nov. 18, 2022).
- [15] “Global warming solutions, facts and information.” <https://www.nationalgeographic.com/environment/article/global-warming-solutions> (accessed Nov. 18, 2022).
- [16] “Clean, green hydrogen with that natural gas | Gowling WLG.” <https://gowlingwlg.com/en/insights-resources/articles/2021/clean-green-hydrogen-with-that-natural-gas/> (accessed Nov. 18, 2022).
- [17] “The Future of Hydrogen,” *Futur. Hydrog.*, 2019, doi: 10.1787/1e0514c4-en.
- [18] E. O. Obanijesu, A. Barifcani, V. K. Pareek, and M. O. Tade, “Experimental study

- on feasibility of H₂ and N₂ as hydrate inhibitors in natural gas pipelines,” *J. Chem. Eng. Data*, vol. 59, no. 11, pp. 3756–3766, Nov. 2014, doi: 10.1021/JE500633U/ASSET/IMAGES/MEDIUM/JE-2014-00633U_0014.GIF.
- [19] M. Flekiewicz and G. Kubica, “AN INFLUENCE OF METHANE/HYDROGEN PROPORTION IN FUEL BLEND ON EFFICIENCY OF CONVERSION ENERGY IN SI ENGINE,” *J. KONES. Powertrain Transp.*, vol. 19, no. 3, pp. 117–124, Jan. 2015, doi: 10.5604/12314005.1137955.
- [20] P. Glanville *et al.*, “Impact of Hydrogen/Natural Gas Blends on Partially Premixed Combustion Equipment: NO_x Emission and Operational Performance,” *Energies* 2022, Vol. 15, Page 1706, vol. 15, no. 5, p. 1706, Feb. 2022, doi: 10.3390/EN15051706.
- [21] S. Lee, M. Kim, and J. Lee, “Analyzing the impact of nuclear power on CO₂ emissions,” *Sustain.*, vol. 9, no. 8, Aug. 2017, doi: 10.3390/su9081428.
- [22] “Methane emissions are driving climate change. Here’s how to reduce them.” <https://www.unep.org/news-and-stories/story/methane-emissions-are-driving-climate-change-heres-how-reduce-them> (accessed Nov. 18, 2022).
- [23] Conley *et al.*, “Methane emissions from the 2015 Aliso Canyon blowout in Los Angeles, CA,” *Sci. 10.1126/science.aaf2348*, 2016, Accessed: Nov. 18, 2022. [Online]. Available: <https://www.science.org/cms/asset/ae34bcec-c488-43fc-81a3-46ea3bc846b4/pap.pdf>
- [24] N. Olmer *et al.*, “GREENHOUSE GAS EMISSIONS FROM GLOBAL SHIPPING, 2013-2015 The authors thank,” 2017, Accessed: Nov. 18, 2022. [Online]. Available: www.theicct.org
- [25] T. . *et al.* . Stocker, “Climate Change 2013: The Physical Science Basis,” *Cambridge Univ. Press*, 2014.
- [26] T. Aldhafeeri, M. K. Tran, R. Vrolyk, M. Pope, and M. Fowler, “A review of

- methane gas detection sensors: Recent developments and future perspectives,” *Inventions*, vol. 5, no. 3. MDPI Multidisciplinary Digital Publishing Institute, pp. 1–18, Sep. 01, 2020. doi: 10.3390/inventions5030028.
- [27] “Methane Tracker 2020 – Analysis - IEA.” <https://www.iea.org/reports/methane-tracker-2020> (accessed Nov. 18, 2022).
- [28] S. Thomas and N. Shahnaj Haider, “Instruments for Methane Gas Detection,” *Int. J. Eng. Res. Appl.*, vol. 4, no. 5, pp. 137–143, 2014, [Online]. Available: www.ijera.com
- [29] M. A. Butt, S. A. Degtyarev, S. N. Khonina, and N. L. Kazanskiy, “An evanescent field absorption gas sensor at mid-IR 3.39 μm wavelength,” <http://dx.doi.org/10.1080/09500340.2017.1325947>, vol. 64, no. 18, pp. 1892–1897, Oct. 2017, doi: 10.1080/09500340.2017.1325947.
- [30] M. Triki, T. Nguyen Ba, and A. Vicet, “Compact sensor for methane detection in the mid infrared region based on Quartz Enhanced Photoacoustic Spectroscopy,” *Infrared Phys. Technol.*, vol. 69, pp. 74–80, Mar. 2015, doi: 10.1016/J.INFRARED.2015.01.016.
- [31] J. Xia, F. Zhu, S. Zhang, A. Kolomenskii, and H. Schuessler, “A ppb level sensitive sensor for atmospheric methane detection,” *Infrared Phys. Technol.*, vol. 86, pp. 194–201, Nov. 2017, doi: 10.1016/J.INFRARED.2017.09.018.
- [32] J. Xia *et al.*, “A sensitive methane sensor of a ppt detection level using a mid-infrared interband cascade laser and a long-path multipass cell,” *Sensors Actuators, B Chem.*, vol. 334, May 2021, doi: 10.1016/j.snb.2021.129641.
- [33] Khalighi M A and Uysal M, “Survey on free space optical communication: a communication theory perspective ,” *IEEE Commun. Surv.*, vol. Tutor. 16, 2014.
- [34] F. Wang, S. Slivken, D. H. Wu, and M. Razeghi, “Room temperature quantum cascade laser with $\sim 31\%$ wall-plug efficiency,” *AIP Adv.*, vol. 10, no. 7, p. 075012,

- Jul. 2020, doi: 10.1063/5.0012925.
- [35] “High-end Laser Systems for Scientific and Industry | TOPTICA Photonics AG.” <https://www.toptica.com/> (accessed Nov. 21, 2022).
- [36] Q. Hao *et al.*, “Mid-infrared transmitter and receiver modules for free-space optical communication,” *Appl. Opt. Vol. 56, Issue 8, pp. 2260-2264*, vol. 56, no. 8, pp. 2260–2264, Mar. 2017, doi: 10.1364/AO.56.002260.
- [37] L. G. Carpenter, S. A. Berry, J. C. Gates, C. B. E. Gawith, P. G. R. Smith, and A. C. Gray, “Upconversion detection of 1.25 Gb/s mid-infrared telecommunications using a silicon avalanche photodiode,” *Opt. Express, Vol. 28, Issue 23, pp. 34279-34289*, vol. 28, no. 23, pp. 34279–34289, Nov. 2020, doi: 10.1364/OE.404855.
- [38] G. Druart *et al.*, “Test of SIMAGAZ: a LWIR cryogenic multispectral infrared camera for methane gas leak detection and quantification,” *SPIE Def. + Commer. Sens.*, p. 10, 2021, doi: 10.1117/12.2586933i.
- [39] I. V. Sherstov and D. B. Kolker, “Photoacoustic methane gas analyser based on a 3.3- μm optical parametric oscillator,” *Quantum Electron.*, vol. 50, no. 11, pp. 1063–1067, Nov. 2020, doi: 10.1070/QEL17316.
- [40] Z. Li *et al.*, “Advances in designs and mechanisms of semiconducting metal oxide nanostructures for high-precision gas sensors operated at room temperature,” *Mater. Horizons*, vol. 6, no. 3, pp. 470–506, Mar. 2019, doi: 10.1039/C8MH01365A.
- [41] A. Hormaza Mejia, J. Brouwer, and M. Mac Kinnon, “Hydrogen leaks at the same rate as natural gas in typical low-pressure gas infrastructure,” *Int. J. Hydrogen Energy*, vol. 45, no. 15, pp. 8810–8826, Mar. 2020, doi: 10.1016/J.IJHYDENE.2019.12.159.
- [42] Y. S. H. Najjar, “Hydrogen safety: The road toward green technology,” *International Journal of Hydrogen Energy*, vol. 38, no. 25. Elsevier Ltd, pp. 10716–10728, Aug. 21, 2013. doi: 10.1016/j.ijhydene.2013.05.126.

- [43] S. M. Frolov, S. N. Medvedev, V. Y. Basevich, and F. S. Frolov, “Self-ignition of hydrocarbon–hydrogen–air mixtures,” *Int. J. Hydrogen Energy*, vol. 38, no. 10, pp. 4177–4184, Apr. 2013, doi: 10.1016/J.IJHYDENE.2013.01.075.
- [44] C. J. Winter, “Energy policy is technology politics - The hydrogen energy case,” *NATO Secur. through Sci. Ser. C Environ. Secur.*, pp. 33–49, 2007, doi: 10.1007/978-1-4020-6442-5_3/COVER.
- [45] K. K. J. R. Dinesh, X. Jiang, and J. A. Van Oijen, “Hydrogen-enriched non-premixed jet flames: Compositional structures with near-wall effects,” *Int. J. Hydrogen Energy*, vol. 38, no. 12, pp. 5150–5164, Apr. 2013, doi: 10.1016/J.IJHYDENE.2013.02.041.
- [46] T. A. Nguyen and M. Mikami, “Effect of hydrogen addition to intake air on combustion noise from a diesel engine,” *Int. J. Hydrogen Energy*, vol. 38, no. 10, pp. 4153–4162, Apr. 2013, doi: 10.1016/J.IJHYDENE.2013.01.082.
- [47] N. R. Mirza, S. Degenkolbe, and W. Witt, “Analysis of hydrogen incidents to support risk assessment,” *Int. J. Hydrogen Energy*, vol. 36, no. 18, pp. 12068–12077, Sep. 2011, doi: 10.1016/J.IJHYDENE.2011.06.080.
- [48] U. Schmidtchen, “Hydrogen Safety,” 2002.
- [49] “Hydrogen: The next wave for electric vehicles? | McKinsey.” <https://www.mckinsey.com/industries/automotive-and-assembly/our-insights/hydrogen-the-next-wave-for-electric-vehicles> (accessed Nov. 18, 2022).
- [50] “6 Differences between Hydrogen and Natural Gas | POWER Engineers.” <https://www.powereng.com/library/6-things-to-remember-about-hydrogen-vs-natural-gas> (accessed Nov. 18, 2022).
- [51] M. H. Amini, “Design and Manufacture of an Ultrasonic Transducer for Long-term High Temperature Operation,” 2016.
- [52] “Seizing the Opportunities for Hydrogen A Call to Action HYDROGEN

- STRATEGY FOR CANADA,” 2020.
- [53] “ATCO to build Alberta’s first hydrogen blending project with ERA support.” <https://www.atco.com/en-ca/about-us/news/2020/122900-atco-to-build-alberta-s-first-hydrogen-blending-project-with-era.html> (accessed Nov. 18, 2022).
- [54] “Groundbreaking \$5.2M hydrogen blending project aims to green Ontario’s natural gas grid - Enbridge Inc.” <https://www.enbridge.com/stories/2020/november/enbridge-gas-and-hydrogenics-groundbreaking-hydrogen-blending-project-ontario> (accessed Nov. 18, 2022).
- [55] “Hydrogen gas .” <https://www.fortisbc.com/services/sustainable-energy-options/hydrogen-gas> (accessed Nov. 18, 2022).
- [56] “Evolugen and Gazifère announce one of Canada’s largest green hydrogen injection projects to be located in Quebec.” <https://www.newswire.ca/news-releases/evolugen-and-gazifere-announce-one-of-canada-s-largest-green-hydrogen-injection-projects-to-be-located-in-quebec-826261149.html> (accessed Nov. 18, 2022).
- [57] C. Fiebig, D.-I. Andreas Hielscher, D.-I. Roland Span, A. Gulin, D.-I. Stefan Rickelt, and D.-I. Peter Schley, “GAS QUALITY TRACKING IN DISTRIBUTION GRIDS WITH SMARTSIM-APPLICATION IN COMPLEX AND MESHED GRIDS”.
- [58] P. Ulbig and D. Hoburg, “Determination of the calorific value of natural gas by different methods.”
- [59] P. Schley, R. Kleinrahm, M. Jaeschke, R. Janssen-Van Rosmalen, and J. A. Schouten, “FEASIBILITY STUDY OF A CORRELATIVE ENERGY MEASUREMENT SYSTEM FOR NATURAL GASES,” 2000.
- [60] “Advanced Piezoelectric Materials,” *Adv. Piezoelectric Mater.*, 2017, doi: 10.1016/C2015-0-01989-X.

- [61] P. E. Mix, "Introduction to nondestructive testing : a training guide," p. 681, 2005, Accessed: Nov. 21, 2022. [Online]. Available: <https://www.wiley.com/en-us/Introduction+to+Nondestructive+Testing%3A+A+Training+Guide%2C+2nd+Edition-p-9780471420293>
- [62] S. Zhang, R. Cao, Z. Jia, Y. Xiong, C. Chen, and Y. Zhang, "Cement/epoxy-based embedded ultrasonic transducers for concrete structure applications," *J. Mater. Res. Technol.*, vol. 14, pp. 242–254, Sep. 2021, doi: 10.1016/J.JMRT.2021.06.067.
- [63] S. G. Joshi, "Ultrasonic flow meter using mode coupling transducers," *Ultrasonics*, vol. 116, p. 106497, Sep. 2021, doi: 10.1016/J.ULTRAS.2021.106497.
- [64] A. J. Zuckerwar, "Handbook of the Speed of Sound in Real Gases ."
- [65] "Nondestructive Evaluation Physics : Sound." <https://www.nde-ed.org/Physics/Sound/tempandspeed.xhtml> (accessed Nov. 21, 2022).
- [66] X.-C. Wang, Y.-H. Wang, H. Zheng, H.-Z. Liu, Y.-J. Yu, and Z.-J. Wang, "Wide-Tunable Mid Infrared Intra-cavity Optical Parametric Oscillator Based on Multi-period MgO:PPLN," 2021, doi: 10.3807/COPP.2021.5.1.059.
- [67] G. G. Ortiz, S. Lee, S. P. Monacos, M. W. Wright, and A. Biswas, "Design and development of a robust ATP subsystem for the Altair UAV-to-ground lasercomm 2.5-Gbps demonstration," <https://doi.org/10.1117/12.478939>, vol. 4975, pp. 103–114, Jul. 2003, doi: 10.1117/12.478939.
- [68] F. Wang, H. Nie, J. Liu, K. Yang, B. Zhang, and J. He, "Miniaturized Widely Tunable MgO:PPLN Nanosecond Optical Parametric Oscillator," *Chinese J. Lasers*, Vol. 48, Issue 5, pp. 0501015 - , vol. 48, no. 5, p. 0501015, Mar. 2021, doi: 10.3788/CJL202148.0501015.
- [69] K. L. Vodopyanov, J. P. Maffetone, I. Zwieback, and W. Ruderman, "AgGaS₂ optical parametric oscillator continuously tunable from 3.9 to 11.3 μm ," *Appl. Phys. Lett.*, vol. 75, no. 9, p. 1204, Aug. 1999, doi: 10.1063/1.124642.

- [70] J. Yang, H. Luo, F. Liu, J. Li, and Y. Liu, “Widely Tunable Gain-Switched Er³⁺-Doped ZrF Fiber Laser from 3.4 to 3.7 μm ,” *IEEE Photonics Technol. Lett.*, vol. 32, no. 20, pp. 1335–1338, Oct. 2020, doi: 10.1109/LPT.2020.3022428.
- [71] M. Bernier, V. Fortin, R. Vallée, P. Paradis, F. Jobin, and S. Magnan-Saucier, “1.4 W in-band pumped Dy³⁺-doped gain-switched fiber laser at 3.24 μm ,” *Opt. Lett. Vol. 45, Issue 18, pp. 5028-5031*, vol. 45, no. 18, pp. 5028–5031, Sep. 2020, doi: 10.1364/OL.398425.
- [72] D. Martyshkin, K. Karki, V. Fedorov, and S. Mirov, “Room temperature, nanosecond, 60 mJ/pulse Fe:ZnSe master oscillator power amplifier system operating at 3.8-5.0 μm ,” *Opt. Express, Vol. 29, Issue 2, pp. 2387-2393*, vol. 29, no. 2, pp. 2387–2393, Jan. 2021, doi: 10.1364/OE.416574.
- [73] S. Aikawa, M. Yumoto, T. Saitoh, and S. Wada, “Mid-infrared tunable pulsed laser based on Cr²⁺-doped II–VI chalcogenide,” *J. Cryst. Growth*, vol. 575, p. 126341, Dec. 2021, doi: 10.1016/J.JCRYSGRO.2021.126341.
- [74] R. Gang, “Studies on the Mid-Infrared Optical Parametric Oscillators and Their Applications,” *Sichuan Univ. Chengdu, China*, 2006.
- [75] D. A. McArthur, “Lasers, Nuclear Pumped,” *Encycl. Phys. Sci. Technol.*, pp. 409–417, 2003, doi: 10.1016/B0-12-227410-5/00369-0.
- [76] X. Wang, “InAs/AlSb Based Mid-Infrared QCL Growth and XRD Simulation,” 2016.
- [77] T. W. Hänsch *et al.*, “Springer Series in”, Accessed: Nov. 21, 2022. [Online]. Available: www.springer.
- [78] A. J. Singh, S. K. Sharma, P. K. Mukhopadhyay, and S. M. Oak, “Dual wavelength operation in diode-end-pumped hybrid vanadate laser,” *Pramana - J. Phys.*, vol. 75, no. 5, pp. 929–934, Nov. 2010, doi: 10.1007/S12043-010-0177-6.
- [79] L. Flannigan, T. Kashak, and C.-Q. Xu, “Study of fundamental wave depletion in

- intracavity second harmonic generation,” *Opt. Express*, vol. 29, no. 5, p. 6810, Mar. 2021, doi: 10.1364/OE.417191.
- [80] “Fundamentals of Photonics: Quantum Electronics | Electrical Engineering and Computer Science | MIT OpenCourseWare.” <https://ocw.mit.edu/courses/6-974-fundamentals-of-photonics-quantum-electronics-spring-2006/> (accessed Nov. 21, 2022).
- [81] Peter E Powers Joseph W Haus, “Fundamentals of Nonlinear Optics,” *CRC Press*.
- [82] T. Ren, C. Wu, Y. Yu, T. Dai, F. Chen, and Q. Pan, “Development progress of 3–5 μm mid-infrared lasers: Opo, solid-state and fiber laser,” *Appl. Sci.*, vol. 11, no. 23, 2021, doi: 10.3390/app112311451.
- [83] Y. Niu *et al.*, “Research progress on periodically poled lithium niobate for nonlinear frequency conversion,” *Infrared Phys. Technol.*, vol. 125, no. June, 2022, doi: 10.1016/j.infrared.2022.104243.
- [84] C. He *et al.*, “High efficiency single-pass SHG of low power CWML and QML laser in an MgO:PPLN,” *Opt. Laser Technol.*, vol. 106, pp. 197–201, Oct. 2018, doi: 10.1016/J.OPTLASTEC.2018.03.027.
- [85] J. Feng, Y. Li, Q. Liu, J. Liu, and K. Zhang, “High-efficiency generation of a continuous-wave single-frequency 780 nm laser by external-cavity frequency doubling,” *Appl. Opt. Vol. 46, Issue 17, pp. 3593-3596*, vol. 46, no. 17, pp. 3593–3596, Jun. 2007, doi: 10.1364/AO.46.003593.
- [86] A. Ghosh, D. Yadav, and G. K. Samanta, “Single-pass, second-harmonic generation of high-power, ultrafast mid-IR Cr²⁺:ZnS laser at 2360 nm,” *Opt. Lett.*, vol. 44, no. 14, p. 3522, Jul. 2019, doi: 10.1364/OL.44.003522.
- [87] B. Zhang, Q. Ma, and C. Q. Xu, “Orthogonally polarized dual-wavelength Nd:YVO₄/MgO:PPLN intra-cavity frequency doubling green laser,” *Opt. Laser Technol.*, vol. 125, p. 106005, May 2020, doi:

10.1016/J.OPTLASTEC.2019.106005.

- [88] S. Song *et al.*, “Small yellow-green Nd:YAG/PPMgLN laser module at 561.3 nm,” *Optik (Stuttg.)*, vol. 232, Apr. 2021, doi: 10.1016/J.IJLEO.2021.166557.
- [89] I.-H. et al. Bae, “Development of a Mid-infrared CW Optical Parametric Oscillator Based on Fan-out Grating MgO:PPLN Pumped at 1064 nm,” *Curr. Opt. Photonics*, vol. Vol. 3, no. No. 1, 2019, Accessed: Nov. 21, 2022. [Online]. Available: https://opg.optica.org/DirectPDFAccess/798367F7-3F75-43E8-8BD7CC9D84CACBE1_406756/copp-3-1-33.pdf?da=1&id=406756&seq=0&mobile=no
- [90] Y. Zhao, H. Zheng, Y. Yu, Y. Wang, H. Liu, and G. Jin, “2.1 μm self frequency conversion optical parameter oscillator based on Nd³⁺ doped MgO:PPLN,” *Opt. Laser Technol.*, vol. 143, Nov. 2021, doi: 10.1016/J.OPTLASTEC.2021.107348.
- [91] Z. Dai and X. Zhang, “Stable high power narrow linewidth single frequency fiber laser using a FBG F-P etalon and a fiber saturable absorber,” *2010 Symp. Photonics Optoelectron. SOPO 2010 - Proc.*, 2010, doi: 10.1109/SOPO.2010.5504159.
- [92] D. A. Kleinman and P. P. Kisliuk, “Discrimination Against Unwanted Orders in the Fabry-Perot Resonator,” *Bell Syst. Tech. J.*, vol. 41, no. 2, pp. 453–462, 1962, doi: 10.1002/J.1538-7305.1962.TB02418.X.
- [93] “Remote Sensing.” https://earthobservatory.nasa.gov/features/RemoteSensing/remote_04.php (accessed Nov. 29, 2022).
- [94] L. Zimmerman, “Comparison of Methane Plume Detection Using Shortwave and Comparison of Methane Plume Detection Using Shortwave and Longwave Infrared Hyperspectral Sensors Under Varying Longwave Infrared Hyperspectral Sensors Under Varying Environmental Conditions Environmental Conditions”, Accessed: Nov. 29, 2022. [Online]. Available: <https://scholarworks.rit.edu/theses>
- [95] “Natural Gas Facts | Canadian Gas Association.” <https://www.cga.ca/natural-gas->

statistics/natural-gas-facts/ (accessed Nov. 21, 2022).

- [96] “‘Green hydrogen’ on sale in open market at 80% higher price than grey H₂ | Recharge.” <https://www.rechargenews.com/transition/green-hydrogen-on-sale-in-open-market-at-80-higher-price-than-grey-h2/2-1-743348> (accessed Nov. 21, 2022).
- [97] “Canada natural gas prices, March 2022 | GlobalPetrolPrices.com.” https://www.globalpetrolprices.com/Canada/natural_gas_prices/ (accessed Nov. 21, 2022).
- [98] I. Staffell, “The Energy and Fuel Data Sheet,” 2011.
- [99] L. Flannigan et al, “Mid-wave and long-wave infrared transmitters and detectors for optical satellite communications-a review ,” *J. Opt*, vol. 24, no. 043002, 2022, doi: 10.1088/2040-8986/ac56b6.
- [100] H. Lin *et al.*, “Chalcogenide glass planar photonics: from mid-IR sensing to 3-D flexible substrate integration,” *Laser Reson. Microresonators, Beam Control XV*, vol. 8600, p. 86000K, Mar. 2013, doi: 10.1117/12.2000683.
- [101] L. Hu, Z. Li, S. Liu, F. Ning, and R. Tan, “Intra-cavity difference frequency generation of 3141 nm based on diode pumped rubidium laser and tandem pumped Nd:YVO₄ laser,” *Opt. Commun.*, vol. 456, p. 124682, Feb. 2020, doi: 10.1016/J.OPTCOM.2019.124682.